MEMS ACCELEROMETERS AND GYROSCOPES
FOR
INERTIAL MEASUREMENT UNITS

A THESIS SUBMITTED TO
THE GRADUATE SCHOOL OF NATURAL AND APPLIED SCIENCES
OF
MIDDLE EAST TECHNICAL UNIVERSITY

BY

MEHMET AKİF ERİŞMİŞ

IN PARTIAL FULFILLMENT OF THE REQUIREMENTS
FOR
THE DEGREE OF MASTER OF SCIENCE
IN
ELECTRICAL AND ELECTRONICS ENGINEERING

SEPTEMBER 2004

Approval of Graduate School of Natural and Applied Science.

_____
Prof. Dr. Canan ÖZGEN
Director

I certify that this thesis satisfies all the requirements as a thesis for the degree of Master of Science.

_____
Prof. Dr. Mübeccel DEMİREKLER
Head of Department

This is to certify that we have read this thesis and that in our opinion it is fully adequate, in scope and quality, as a thesis for the degree of Master of Science.

_____
Prof. Dr. Tayfun AKIN
Supervisor

Examining Committee Members:

Prof. Dr. Cengiz BEŞİKÇİ	(METU, EEE)	_____
Prof. Dr. Tayfun AKIN	(METU, EEE)	_____
Prof. Dr. Aydan ERKMEN	(METU, EEE)	_____
Instructor Dr. Haluk KÜLAH	(METU, EEE)	_____
Dr. Volkan NALBANTOĞLU	(ASELSAN)	_____

I hereby declare that all information in this document has been obtained and presented in accordance with academic rules and ethical conduct. I also declare that, as required by these rules and conduct, I have fully cited and referenced all material and results that are not original to this work.

Mehmet Akif ERİŞMİŞ

ABSTRACT

MEMS ACCELEROMETERS AND GYROSCOPES FOR INERTIAL MEASUREMENT UNITS

Erişmiş, Mehmet Akif
M.Sc., Department of Electrical and Electronics Engineering
Supervisor: Prof. Dr. Tayfun Akın

September 2004, 137 pages

This thesis reports the development of micromachined accelerometers and gyroscopes that can be used for micromachined inertial measurement units (IMUs). Micromachined IMUs started to appear in the market in the past decade as low cost, moderate performance alternative in many inertial applications including military, industrial, medical, and consumer applications. In the framework of this thesis, a number of accelerometers and gyroscopes have been developed in three different fabrication processes, and the operation of these fabricated devices is verified with extensive tests. In addition, the fabricated accelerometers were combined with external readout electronics to obtain hybrid accelerometer systems, which were tested in industrial test facilities.

The accelerometers and gyroscopes are designed and optimized using the MATLAB analytical simulator and COVENTORWARE finite element simulation tool. First set of devices is fabricated using a commercial foundry process called SOIMUMPs, while the second set of devices is fabricated using the electroplating processes

developed at METU-MET facilities. The third set of devices is designed for a new advanced process based on DRIE, which is under development.

Mechanical and electrical test results of the fabricated accelerometers and gyroscopes are in close agreement with the designed values. The testing of the SOI and nickel accelerometers is also performed in industrial test environments. In order to perform these tests, accelerometers are hybrid connected to commercially available capacitive readout circuits. These accelerometer systems require only two DC supply voltages for operation and provide an analog output voltage related to the input acceleration. The industrial tests show that the SOI accelerometer system yields a 799 μg/√Hz average noise floor, a 1.8 mg/√Hz peak noise floor, a 22.2 mV/g sensitivity, and a 0.1 % nonlinearity, while the nickel accelerometer system yields a 228 μg/√Hz average noise floor, a 375 μg/√Hz peak noise floor, a 1.02 V/g sensitivity, and a 0.23 % nonlinearity. Long-term drift components of the accelerometers are determined to be smaller than 20 mg. These systems are the highest performance micromachined accelerometer systems developed in Turkey, and they can be used in implementation of a national inertial measurement unit.

Keywords: Accelerometer, Gyroscope, Inertial Measurement Unit, Micro-Electro-Mechanical Systems (MEMS), and micromachined inertial devices.

ÖZ

ATALETSEL ÖLÇÜM BİRİMİ İÇİN MEMS İVMEÖLÇERLER VE DÖNÜÖLÇERLER

Erişmiş, Mehmet Akif
Yüksek Lisans, Elektrik ve Elektronik Mühendisliği Bölümü
Tez Yöneticisi: Prof. Dr. Tayfun Akın

Eylül 2004, 137 sayfa

Bu tez ataletsel ölçüm biriminde (IMU) kullanılabilecek mikroişlenmiş ivmeölçerler ve dönüölçerler geliştirilmesini rapor etmektedir. Mikroişlenmiş IMU'lar, endüstriyel, medikal ve tüketici uygulamalarında, düşük maliyetli ve yüksek performanslı alternatifler olarak kullanılmaya başlanmıştır. Bu tez çalışması kapsamında çok sayıda ivmeölçer ve dönüölçer üç farklı üretim süreci kullanılarak geliştirilmiş, ayrıca yapılan çeşitli testlerle ürünlerin istenilen şekilde çalıştıkları gösterilmiştir. Buna ek olarak, tez kapsamında üretilmiş olan ivmeölçerler, dış okuma devreleri ile birleştirilerek hibrit ivmeölçer sistemleri tasarlanmış ve bu sistemler endüstriyel test alanlarında test edilmiştir.

İvmeölçerler ve dönüölçerler MATLAB analitik simülatör ve COVENTORWARE sonlu eleman simülatörü ile tasarlanmış ve en iyilenmiştir. İlk grup ürünler SOIMUMPs adlı ticari bir üretim süreci ile üretilirken, ikinci grup ürünler METU-MET tesislerinde geliştirilen elektrokaplama yöntemi ile üretilmiştir. Üçüncü grup ürünler halen geliştirilmekte olan DRIE bazlı yeni ve gelişmiş bir ürün süreci için tasarlanmıştır.

Üretilen ivmeölçerler ile dönüölçerlerin mekanik ve elektriksel test sonuçları tasarlanan değerlere çok yakın çıkmıştır. SOI ve nikel ivmeölçerlerin testleri endüstriyel ortamlarda da gerçekleştirilmiştir. Bu testleri gerçekleştiribilmek için ivmeölçerler, endüstriyel bir kapasitif okuma devrelerine hibrit bağlanmıştır. Bu ivmeölçer sistemleri sadece iki DC voltaj kaynağı ile beslenmekte ve ölçülen ivmeyle orantılı analog voltaj çıkışı vermektedir. Endüstriyel testler, SOI ivmeölçer sisteminin 799 µg/√Hz ortalama gürültü seviyesi, 1.8 mg/√Hz tepe gürültü seviyesi, 22.2 mV/g orantı katsayısı, ve % 0.1 orantı katsayısı hatası olduğunu ve nikel ivmeölçer sisteminin 228 µg/√Hz ortalama gürültü seviyesi, 375 µg/√Hz tepe gürültü seviyesi, 1.02 V/g orantı katsayısı, % 0.23 orantı katsayısı hatası olduğunu göstermiştir. Uzun süreli sabit kayma ile açış-kapanış sabit kayma değerlerinin 20 mg'den küçük olduğu bulunmuştur. Bu sistemler Türkiye'de üretilen en yüksek performanslı mikroişlenmiş ivmeölçer sistemleri olup, ulusal ataletsel ölçüm birimi geliştirilmesinde kullanılabilirler.

Anahtar Kelime: İvmeölçer, Jiroskop, Ataletsel Ölçüm Birimi, Mikroelektromekanik Sistemler (MEMS) ve mikroişlenmiş ataletsel sensörler.

To my family

ACKNOWLEDGEMENTS

First of all, I would like to thank my family for their love and support. I would specially like to thank my advisor Prof. Dr. Tayfun Akın for his guidance and support, and especially for his friendly attitude.

I would like to thank Mr. Said Emre Alper and Mr. Fırat Yazıcıoğlu for sharing their knowledge with me, for helping me especially in fabrication steps, and for their patience to my endless questions. I would like to thank Mr. Orhan Akar for his suggestions in the fabrication process and for wire bonding sessions. I would like to thank our group computer administrator Mr. Murat Tepegöz for his time spent on constructing and maintenance of our group's computer network. I would like to acknowledge all METU-MEMS group members for providing a nice research atmosphere. I would like to thank METU-MET personnel for their help in the fabrication steps. Also, I would like to thank all my friends for their support and friendship. I would like to thank TUBITAK-SAGE and ASELSAN for providing their test facilities, and finally I would like to thank ASELSAN for SEM pictures.

TABLE OF CONTENTS

LIST OF FIGURES

LIST OF TABLES

CHAPTER 1

INTRODUCTION

Tracking the position of an object is an important engineering problem that finds many application areas including military, industrial, medical, and consumer applications. This problem is effectively solved with an Inertial Measurement Unit (IMU). An IMU consists of three orthogonally placed accelerometers and gyroscopes, and these sensors find the linear acceleration and angular velocity of the object that it is mounted on. Knowing linear acceleration and angular velocity in three dimensions is enough to track the motion of the system with the help of additional mathematical operations [1].

MEMS inertial sensors, accelerometers and gyroscopes, started to appear in the market due to their low cost, small size, low power consumption, and promising performances. Although these sensors initially fit for applications where cost and size are more important than performance, currently their performances satisfy and even extend beyond the limits of conventional sensing systems.

Performance requirements of inertial sensors vary for different applications. Table 1-1 shows the range and bias requirements for the gyroscopes, Figure 1.1 shows the bandwidth-resolution performance requirements of the accelerometers for different applications, and Figure 1.2 shows the cost-bias instability performances of IMUs.

In general, the highest performance is required for military applications. Military navigation is the main application that pushes the development of higher performance inertial sensors. Global Positioning System (GPS), which is developed initially for military applications to track an object's position with high accuracy, combines the high performance IMUs, precision time references, radio communications, and spaceborne satellite network to achieve a precise track of motion [1-2]. The performances of the IMUs for military applications should be superior compared to the ones used for other applications. The drift values should be less then 0.1 deg/hour for the gyroscopes and in the order of few μg for accelerometers to be used in navigation applications [3-5]. The fiber-optic gyroscopes are used for these applications, but their fabrication is rather complicated [4-6]. On the other hand, the performances of micromachined accelerometers and gyroscopes are not far beyond the optical inertial sensors due to advances in micromachining technologies in the past decade [7].

Industrial applications require inertial sensors for testing and conditioning purposes. For example, accelerometers are placed into the shipping containers for monitoring the magnitudes of the shocks applied to the container during the transportation. This way, the customer or the shipping service is able to check whether the container is handled properly or not [1, 8-9]. In another application, accelerometers are put into computer hard drives for detecting the external shock. Due to the fact that high shock values may cause damage to the read/write head of the device, the accelerometer may suspend the operation of the drive when there is excessive external shock [1, 10]. In these applications, the performance of these sensors is not as critical as those used for military applications, but here, the cost of the sensors should be reasonably low. Therefore, micromachined inertial sensors are highly preferred in these applications for their low cost, low power consumption, and high reliability as well as satisfactory performance.

Table 1-1: Range and bias stability requirements for gyroscopes for different applications. [3-4].

Application Area	Uses	Range	Bias Stability
Navigation	Aircraft Spacecraft/Satellite Land Cruise Missile	200 deg/sec	0.01-0.1 deg/hr
Tactile Missiles	Air-to-surface Air-to-land Air-to-surface	200 deg/sec	0.1-100 deg/hour
Automotive	Navigation Airbags ABS/TCS Active suspension	100 deg/sec	0.001-1 deg/sec
Medical and Consumer electronics	Microsurgery Camcorders Robotics	10-100 deg/sec	0.1 deg/sec

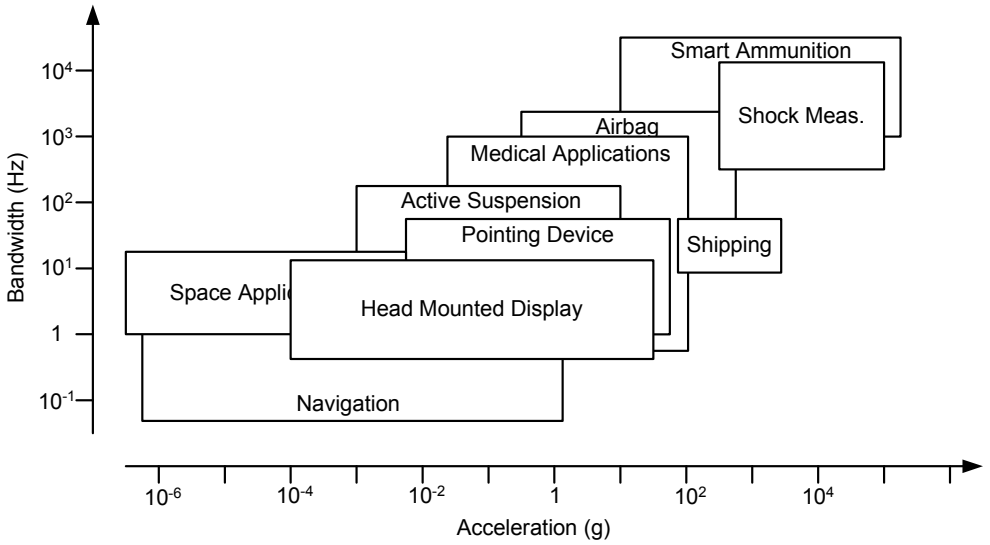

Figure 1.1: The application areas for accelerometers and the bandwidth-resolution performances of the accelerometers for these applications [5, 11].

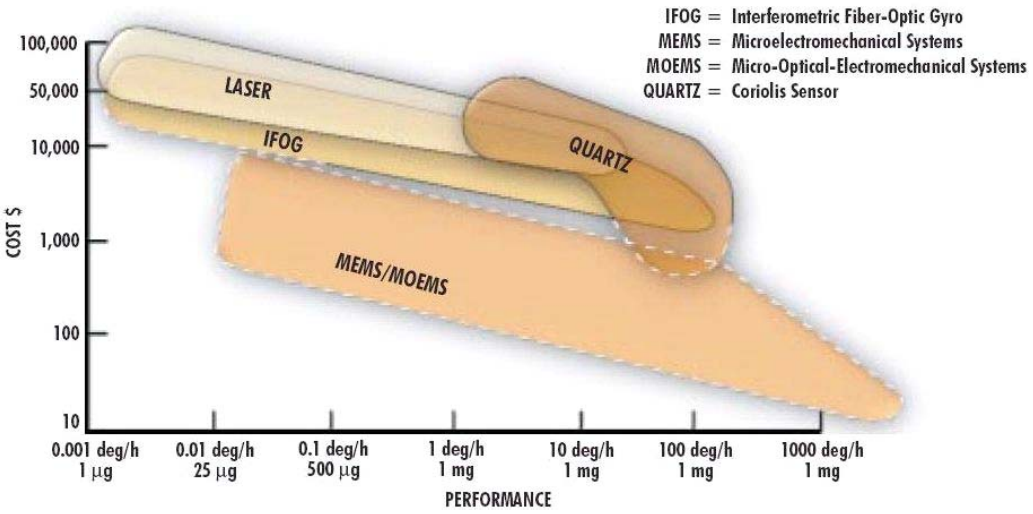

Figure 1.2: Cost-bias instability performances of IMUs, [12].

The medical applications use inertial sensors and IMUs for monitoring the physical body activities such as absolute position of the leg segments or heart monitoring [1, 13-14]. Similar to the industrial applications, in this area, the performance of the sensors is not as critical as those used for military application, but power consumption and small volume are more important. Hence, low cost micromachined inertial sensors started to appear in this application area.

The consumer applications include the automotive applications, entertainment applications, and consumer navigation applications. In the automotive industry, the MEMS accelerometers are widely used in airbag systems after the Analog Devices' ADXL accelerometer series [15-16]. Moreover, Anti-skid Braking Systems (ABS) requires inertial rate sensors [17]. In entertainment sector, accelerometers and gyroscopes are widely used in video cameras or joysticks for control and stability purposes. Moreover there is a research going on virtual reality sector in which the inertial sensors will be widely used. In consumer navigation applications, low-cost IMUs with relatively lower performance are used in detecting the position of an object [1]. In all these applications, small sensor volume is the key factor which can be satisfied by using micromachined inertial sensors.

Table 1-2 gives the comparison of the applications and the priority of IMU properties for these applications.

Table 1-2: Comparison of the applications and the priority of IMU properties for these applications.

	High Performance	**Low Cost**	**Low Power**	**High Reliability**	**Small Size**
Military	✓			✓	
Industrial		✓	✓	✓	
Medical		✓	✓		✓
Consumer		✓	✓	✓	✓

This study includes the design and fabrication of various accelerometers and gyroscopes for low-cost IMUs to be used for some military and consumer applications. An accelerometer topology previously developed at METU-MEMS research group [11] is adapted for three different processes in order to improve overall performance. In addition symmetric and decoupled gyroscope structure [3] is modified for lowering the DC polarization voltages necessary for the operation of the gyroscope. The sensors are first modeled using MATLAB and COVENTORWARE in order to estimate their performances, and then layouts are drawn for three different processes. After the layouts, sensors are fabricated in two processes at METU-MET facilities. Following the fabrication, resonance frequencies and capacitance values for each accelerometer and gyroscope are measured. After the initial measurements, two accelerometer samples are connected to readout circuitries to form two hybrid accelerometer systems. These hybrid systems are tested in TUBITAK-SAGE and ASELSAN facilities.

This chapter provides a brief review of MEMS accelerometers and gyroscopes. Section 1.1 explains the basic operation of accelerometers and gyroscopes. Section 1.2 presents the accelerometer and gyroscope types and gives high performance capacitive accelerometer and gyroscope examples. Section 1.3 provides the objective of this study and the organization of the thesis.

1.1 Basic Operation Principles of Accelerometers and Gyroscopes

An accelerometer is a sensor that senses external acceleration. To extract the acceleration value, the sensor has a movable proof mass which is connected to a fixed frame via spring structures. When there is an external acceleration, the proof mass is displaced from its rest position. The magnitude of this displacement is proportional to the magnitude of the acceleration and inversely proportional to the stiffness of the spring structures. Hence, the acceleration input that is applied to the sensor is converted to the proof mass displacement in the sensor. The sensor then extracts the magnitude of this displacement using its sensing scheme. The accelerometers are characterized using their sensing schemes, and this characterization is explained in the next section. A detailed operation principle of the accelerometer is given in Chapter 2.

A gyroscope is a sensor that senses external angular velocity. The similarity of the operation principle of the gyroscope with that of the accelerometer is that, the gyroscope converts the angular velocity input to displacement of its proof mass. For this purpose the gyroscope uses the Coriolis acceleration principle [1, 3, 6]. First the proof mass of the gyroscope is vibrated in one axis, and then when there is an external angular velocity, the proof mass starts vibrating in another axis due to Coriolis acceleration principle. The second vibration magnitude is proportional to the angular velocity input magnitude. Hence, the sensing scheme of the gyroscope extracts the magnitude of the input angular velocity with extracting the magnitude of the secondary vibration. A detailed operation principle of the gyroscope is also provided in Chapter 2.

1.2 Classification of MEMS Accelerometers and Gyroscopes

MEMS accelerometers and gyroscopes can be mainly classified into eight groups according to their sensing mechanisms:

- Capacitive
- Optical
- Piezoresistive
- Piezoelectric
- Thermal
- Tunneling current
- Resonant
- Magnetic

In capacitive accelerometers, the proof mass displacement is detected with the change in the capacitance between the proof mass and the sense electrodes. In capacitive gyroscopes, the primary vibration is obtained using electrostatic forces between the proof mass and the drive electrodes, and the proof mass displacement due to secondary vibration is detected with the charge in the capacitance between the proof mass and the sense electrodes similar to that of the capacitive accelerometers.

Capacitive sensors have important advantages compared to other types of inertial sensors. They have simple structure and hence low fabrication cost. In addition, they provide low power consumption, high sensitivity, and high reliability as well as low nonlinearity, low temperature dependency, low noise, and low drift. DRIE, LIGA and other advanced MEMS processes enable the fabrication of very high aspect ratio structures which improves the sensitivity of the sensors [18-20]. Using DRIE and high performance capacitive readout circuits, 1 μg/√Hz resolution is achieved in accelerometers [7], and 10.4°/hr/√Hz resolution is achieved for the gyroscopes [18].

Capacitive sensors are widely preferred in consumer application due to their high performance, reliability, and low cost. Analog Devices commercialized capacitive accelerometers and also gyroscopes. ADXL series accelerometers available in the market with different resolution and operation range choices. These sensors are fabricated with surface micromachining with polysilicon as the structural layer monolithically integrated with the readout electronics [21], and intended for consumer applications. ADXRS series gyroscopes are also available in the market for consumer applications.

Optical inertial sensors are rather difficult to fabricate but show high performances. The major advantages for optical inertial sensors are that they are immune to electromagnetic interference and they can operate at high temperatures. They show high performances but fabrication of light emitting and sensing components using micromachining techniques is not easy [11]. A 90 μg/√Hz resolution optic accelerometer is reported in the literature [22]. For the gyroscopes, fiber-optic gyroscopes are the first replacements of the big mechanical gyroscopes. However, they have a more complex fabrication compared to capacitive MEMS gyroscopes.

Piezoresistive sensing scheme is widely used in accelerometers [23-25]. However, to use piezoresistive materials in gyroscopes, the gyroscope should be driven in its primary mode with a different mechanism due to the fact that piozoresistive materials cannot induce force due to its passive nature [26]. Sensors using piezoresistive materials are easy to fabricate and they have simple readout circuitries. However, their sensitivity is low [6], and their temperature dependency is high [11] compared to capacitive sensors. Therefore, they are not preferred for high performance applications. In the literature, piezoresistive accelerometer with 0.2 mg/√Hz is reported [23]. There are also gyroscopes using different drive mechanism such as piezoelectric or magnetic, and use piezoresistive sensing [27-28].

The operation of piezoelectric sensors requires an external stress similar to the piezoresistive sensors. The sensitive material stores a charge on itself proportional to this external stress. This charge-storage makes the sensor an active device, theoretically providing it to generate its own power and provides low power sensor design [11]. In addition to this, the fabrication of piezoelectric sensors is as easy as piozoresistive sensors enabling low cost sensor realization. However, the main disadvantage of the piezoelectric sensors is that they do not have a DC response due to the fact that the charge stored on the piezoelectric material leaks away under a constant stress [11]. Therefore, low frequency operation is not possible. This fact makes it difficult to realize piezoelectric accelerometer since accelerometers are generally used to sense low frequency accelerations. However for the gyroscopes, the problem is not as critical as it for the accelerometers because the gyroscope brings the input angular velocity input frequency to its drive mode resonance frequency which is around a few kHz. Another disadvantage for the piezoelectric sensors is the difficulty in readout electronics. The output resistance of the sensor is high, hence it is difficult to get the signal out. There are piezoelectric accelerometer examples in the literature [29-30] and also a commercial gyroscope example realized by Murata Inc. [31].

There are also different sensing scheme studies for accelerometers such as thermal sensing [32]. In this example the proof mass of the accelerometer is a hot air bubble which is placed between two electrodes. When there is not any input acceleration, the temperature difference between the electrodes is fixed. However, when an external acceleration is applied, this bubble moves and changes the temperature difference between the electrodes. Hence, the acceleration is converted to the temperature difference. This temperature difference is sensed and acceleration is extracted. Another type of accelerometer is resonant type accelerometer which directly finds the applied force onto the proof mass [33]. The proof mass is vibrated in its natural resonance frequency and the inertial force caused by external acceleration changes the resonance frequency of the system. By finding the shift in the resonance frequency, the magnitude of the acceleration can be extracted. A third type of accelerometer is the tunneling current accelerometer, which has very low noise, has

wide bandwidth, and is highly sensitive. This type of accelerometer uses tunneling current that occurs between two conductive layers located very close to each other. The distance between these electrodes should be about 10 Å to create a tunneling current [11]. When there is an external acceleration, one of the conductive layers moves, and changes the tunneling current. With this reading scheme very low noise levels like 20 ng/√Hz is achieved for accelerometers [34], but high drift values, fabrication complexity, and high cost prevent tunneling accelerometers to be widely used in the industry.

Magnetism is generally used to create the drive mode vibration of the gyroscopes [35]. However, gyroscopes with electromagnetic drive and sensing schemes are also reported [36]. But, the performance of these sensors is not as promising as the capacitive ones.

In summary, there are a number of approaches to implement accelerometers and gyroscopes, but the widely used one is the capacitive approach, as it is suitable for MEMS fabrication techniques. Therefore, capacitive approach is used in this study to implement various accelerometers and gyroscopes.

1.3 Objectives of the Study and the Organization of the Thesis

The objectives of this study can be summarized as below:

- The main objective of this study to construct an accelerometer system which has satisfactory noise-floor/nonlinearity performance for IMUs to be used in some military and consumer applications and is powered with only ±12 DC batteries. The system is to yield a voltage output proportional to the externally applied accelerometer. The proposed system is composed of a MEMS accelerometer, a capacitive readout circuit, the bias circuitry for this capacitive readout circuit, and amplifier stages. Table 1-3 summarizes the performance goals of this hybrid accelerometer system. Sensitivity and

nonlinearity requirements are provided by ASELSAN. Bias drift value goal is appropriate for some control applications in especially consumer applications, and noise floor goal is adequate for detecting acceleration inputs for control applications for some military and consumer applications.

Table 1-3: The performance goals of the hybrid accelerometer system.

Parameter	**Performance Goals**
Supply Voltage	±12
Sensitivity	1 V/g
Nonlinearity	1 %
Noise Floor	500 μg/√Hz
Bias Drift	20 mg

- The second objective of this study is to achieve an improvement in the symmetric and decoupled gyroscope developed previously by METU-MEMS group [3] by lowering the DC polarization voltage and fabrication of this improved gyroscope in three different fabrication processes.

- The third objective is the optimization in design and fabrication area with designing micromachined sensors for three different fabrication processes and participation the fabrication steps of two of these processes. The optimization in the fabrication area will improve the success rate of the future designs of METU-MEMS group members, and also increase the performances of these designs.

This thesis reports micromachined accelerometers and gyroscopes designed during this research. Eight accelerometer and four gyroscope prototypes designs are designed, simulated, fabricated, and tested in three different micromachining technologies.

Chapter 2 describes the theoretical background required for the design of MEMS accelerometers and gyroscopes. Specifically, it explains some commonly used mechanical definitions, spring constant derivation methods, Coriolis force definition, and also accelerometer and gyroscope models.

Chapter 3 focuses the design and modeling of accelerometer and gyroscope prototypes. First, it explains the important performance parameters for accelerometers and gyroscopes. Next, it gives the design considerations for the fabrication imperfections. Then, the chapter provides the details of accelerometer and gyroscope designs with giving the topologies, MATLAB/COVENTORWARE simulation results, and comparison of these results for these designs. Finally the chapter gives the expected performance values of the designed sensors.

Chapter 4 gives the details of the three fabrication processes that are used to implement the accelerometers and the gyroscopes in this study. The first process is called SOIMUMPs and it is performed by a commercial MEMS foundry. The second process is based on electroplating process developed by METU-MEMS group. And the third process is based on DRIE etching. This process is currently being developed at METU-MET for high performance accelerometers and gyroscopes.

Chapter 5 provides the fabrication and test results. First, Scanning Electron Microscope (SEM) and optical microscope pictures of the fabricated structures are presented. Then, the chapter explains the tests performed on the accelerometer and gyroscope samples. Next, it explains the hybrid accelerometer systems that are constructed by connecting high performance SOIMUMPs and nickel electroplated accelerometer samples to the commercially available MS3110 readout circuit. Finally, the chapter gives the test results that are done to characterize the hybrid systems.

Finally, Chapter 6 gives the conclusion of the thesis and suggests future studies to improve MEMS accelerometer and gyroscope systems.

CHAPTER 2

THEORETICAL BACKGROUND

This chapter presents the theoretical background on the design of capacitive MEMS accelerometers and gyroscopes. Section 2.1 gives the definitions of some commonly used mechanical terms related with the accelerometer and gyroscope design. Section 2.2 explains the derivation of spring constants for variable spring shapes. Section 2.3 discusses the Coriolis force, which causes the secondary motion in the vibratory gyroscopes. Section 2.4 explains the basic accelerometer and gyroscope model. Section 2.5 explains different capacitive sensing and actuating topologies used in accelerometers and gyroscopes. Finally, Section 2.6 gives the summary of the whole chapter.

2.1 Definitions of Some Commonly Used Mechanical Terms

The design of accelerometers or gyroscopes needs strong background in both electrical and mechanical area. For the mechanical side, the designer should be familiar with some common mechanical terms like stress, strain, elasticity [3]. In this section, the definitions of these terms are given. Some mechanical terms like Poisson's ratio are also mentioned for the sake of completeness although it is not directly related with the mechanical design.

Stress is the defined as the force per unit area acting on the surface of a differential volume element of a solid body [26]. The stresses that are caused by forces perpendicular to differential face is called *normal stresses* and the stress caused by forces along the face is called shear stresses [26]. Normal stress is generally denoted by σ, and shear stress is generally denoted by τ. Equation 2.1 shows the basic formulation of stress where F is the applied force and A is the cross sectional area [37].

$$\sigma = \frac{F}{A} (\mathrm{N/m^2}) \tag{2.1}$$

The stress can either be *compressive* or *tensile* depending on the direction of the force acting on the differential face [38]. This fact is mostly important in fabrication issues whether the fabricated structure will deform or not after a release operation.

Another important mechanical term is the *Strain*, which can be defined as the deformation resulting from a stress, and measured as the ratio of deformation to the total dimension of the body in which the deformation is occurred. The deformation depends on the direction of the applied force. The compressive force causes the body to be shortened and the tensile force causes the body to be stretched [3]. The normal strain is denoted by ε and formulated as:

$$\varepsilon = \frac{\delta}{L} \tag{2.2}$$

where δ is the amount of deformation and L is the original dimension. Shear strain is denoted by γ.

Figure 2.1 shows the Stress-Strain relationship of a general material. In a MEMS design, designers try to stay in the linear region of this graph where the strain values are relatively small. In this linear region, another mechanical property of the

materials can be defined as *Young's Modulus* which is the proportionality constant in this linear region and can be expressed as:

$$E = \frac{\sigma}{\varepsilon} \ (\mathrm{N/m^2}) \tag{2.3}$$

where E denotes Young's Modulus [37].

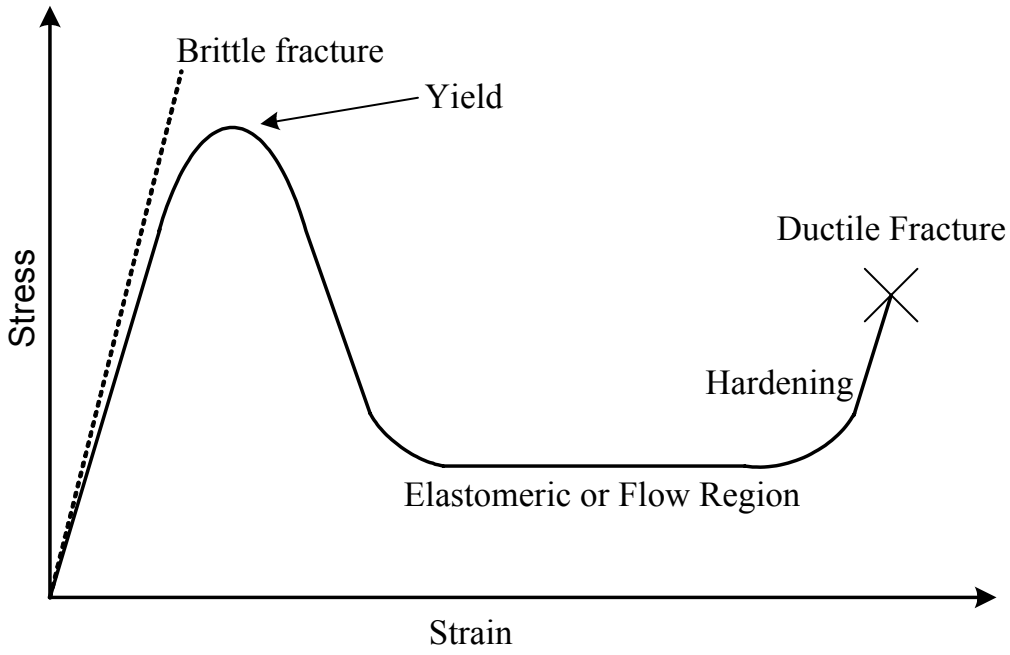

Figure 2.1: Stress-Strain relationship of a general material [26].

In real life, if there is deformation in one direction due to a stress source, there will be deformations in other directions. If a beam is squeezed so that its length is shortened, than the width of the beam widens. From this fact, another mechanical term is defined. Poisson's Ratio is the ratio of lateral strain to axial strain and is generally denoted by ν [37].

Moment of Inertia is also an important term in MEMS design. Moment of inertia of an area with respect to an axis is the sum of the products obtained by multiplying the infinitesimal area elements by the distance of this element from the axis. Moment of inertia is denoted by 'I' and can be expressed as:

$$I = \int y^2 dA \tag{2.4}$$

where dA is the infinitesimal area element and y is the distance of this area element to the origin of interest.

2.2 Derivation of Spring Constant for Variable Spring Shapes

In MEMS accelerometers and gyroscopes, spring constants play an important role in determining the performances of the sensors. The performance of the sensors is related with the easiness in the movement of the proof mass in certain directions and also with the difficulty in the movement of the proof mass in some other directions. Hence, determining the spring constants in all directions is an important design step. In this chapter, spring constant calculations in each three directions will be discussed.

Figure 2.2 shows a spring beam in its rest position. The spring constant in its relative axis depends on how the beam is bended. If the beam bends in a way that the parallelism of the fixed end and the free end is disturbed, it is called "Deflection of a Cantilever Beam." If the parallelism is preserved, then the condition is called "Deflection of a Fixed-Guided End Beam."

Deflection of a cantilever beam condition is the basic condition to be analyzed. The spring constants for this condition along each direction are calculated as [3, 11, 38]:

$$k_x = \frac{Ehw}{l} \qquad k_y = \frac{Ehw^3}{4l^3} \qquad k_z = \frac{Ewh^3}{4l^3} \tag{2.5}$$

where the direction index denotes the direction of the applied force which bends the spring beam, E is the Young's Modulus, h is the thickness, w is the width, and l is the length of the beam.

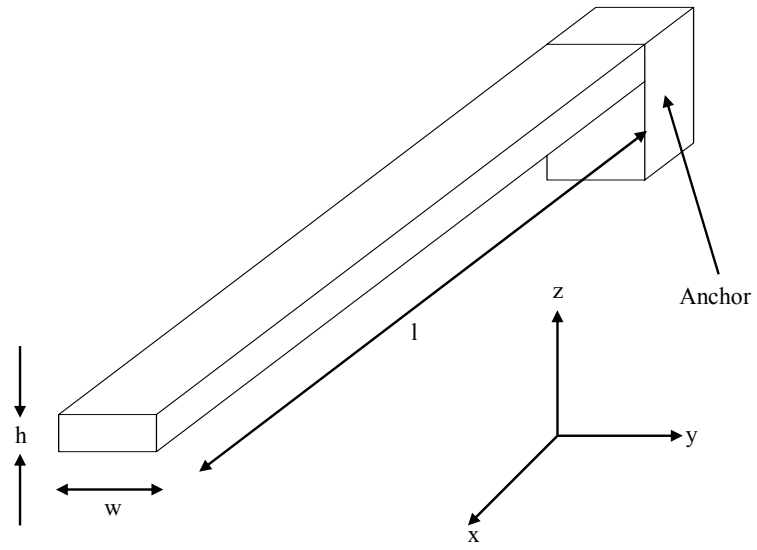

Figure 2.2: A spring beam in its rest position.

The spring constant for fixed-guided end beam can be found by using the deflection formulation similar to the cantilever beam condition [38]. Another way of calculating the spring constant of fixed-guided end beam is to use parallel and series spring constants. Figure 2.3 shows the resultant spring constant of parallel and series connected springs.

Fixed-guided end beam deflection can be modeled as series connected of two half length clamped beam springs. Figure 2.4 shows the series connection of two half length clamped beam springs forming a fixed-guided end beam. From this observation, the spring constant for a fixed-guided beam can be found as:

$$k_{res} = k/2 = \frac{1}{2}\frac{Ehw^3}{4\left(\frac{l}{2}\right)^3} = \frac{Ehw^3}{l^3} \tag{2.6}$$

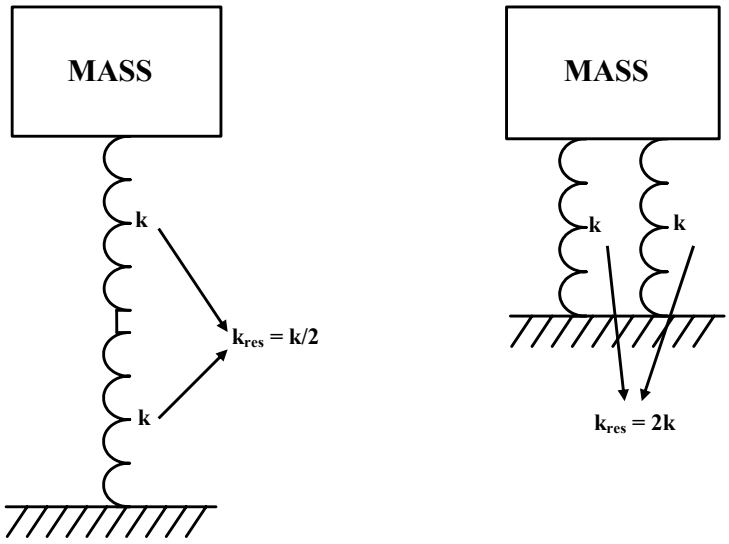

Figure 2.3: Resultant spring constants for parallel and series springs.

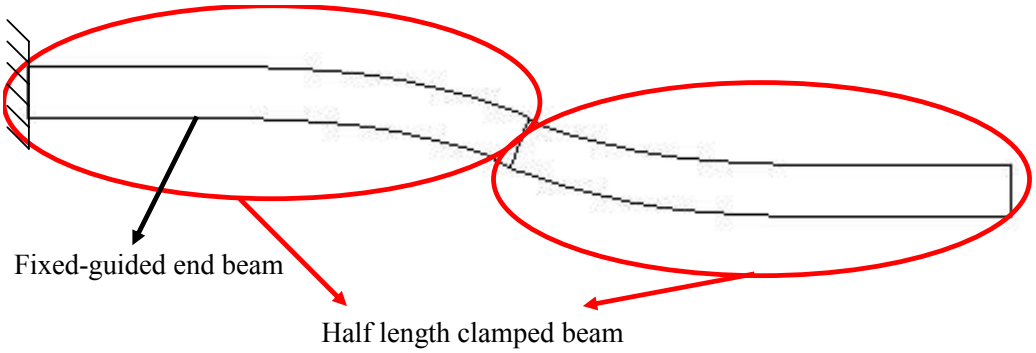

Figure 2.4: Series connected half clamped beams forming a fixed-guided end beam.

Spring constants for various shape beams can be extracted similarly using parallel series connection springs idea. Figure 2.5 shows different lateral beam structures used in this study and calculated spring constants. First important note is that the free ends of these beams move in a way that the parallelism of the free end with the

fixed end is preserved. This can be achieved by symmetrical beam allocations around the proof mass. Another important note is the rigidity of the truss regions. If the truss regions remain rigid when the beam deflects, we assume that all the sub-beams forming the total beam are fixed-guided end beams keeping in mind that first note condition is preserved. In this study, the truss region widths are designed to be at least 4 times wider then the beam widths to preserve the rigidity of the truss regions. In addition the beams are allocated symmetrically around the proof mass not to disturb the parallelism of the free and fixed end of the beams.

Although the spring constant calculations for lateral beams can model the real beams with a good accuracy, we cannot achieve a similar accuracy in z-axis beams. The reason behind this fact is the rotation of the truss regions. While the beams in Figure 2.5 are deflected in z-axis, the truss regions tend to rotate although the rigidity is preserved. Thus, the sub-beams have additional rotational spring constants. Due to this fact, it is better to design the z-axis beams using FEM simulators or more sophisticated spring constant extraction programs.

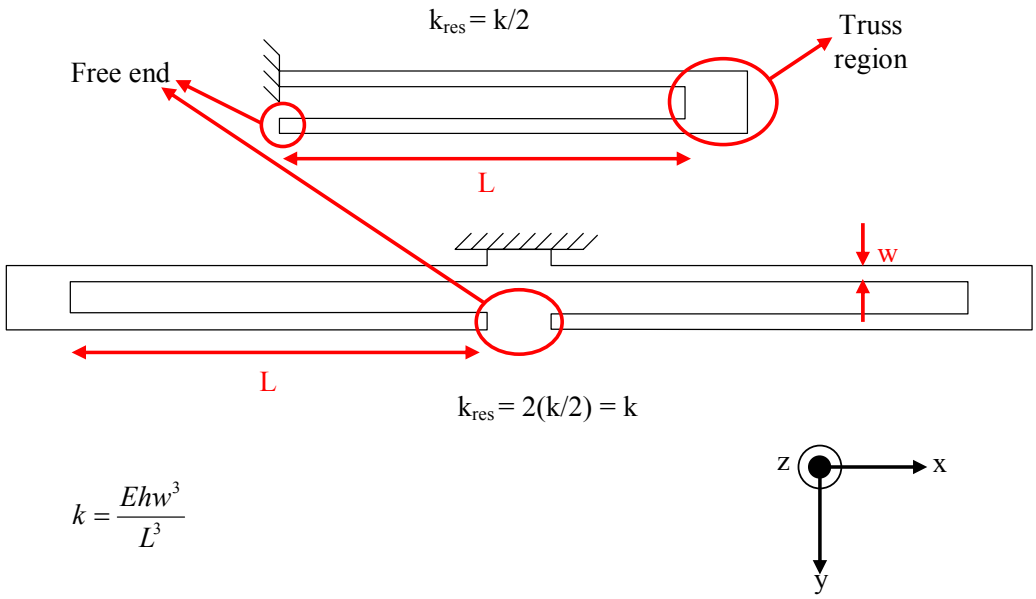

Figure 2.5: Different spring structures used in this study and calculated resultant spring constants.

2.3 Coriolis Force

Micromachined vibratory gyroscopes are based on the transfer of energy between two vibratory modes of a structure caused by Coriolis acceleration [1, 6]. Coriolis acceleration is a result of Newton's law of motion applied to rotating frames [1].

Assume that an observer is swinging a pendulum on earth. The motion of the pendulum is analogous the primary vibration of the gyroscope. Due to the fact that the pendulum is making its vibratory motion on earth which is a rotating frame, the observer standing on the earth sees the pendulum making an elliptical movement instead of a single axis movement. This elliptical movement is due to the Coriolis force that causes a secondary vibration perpendicular to the primary vibration. However, for an observer outside the rotating frame, the earth, the pendulum is really making a single axis vibration. Hence, Coriolis force is fictitious force acting on a moving object in a rotating frame. In fact, the observer in the same rotating frame rotates as the frame rotates and sees the pendulum as making an elliptical movement; the pendulum just makes a single axis vibration [39]. This is the physical explanation of the Coriolis force. Figure 2.6 shows the coordinate system indicating the directions of angular velocity, primary and secondary vibratory modes of a gyroscope, with a tuning fork gyroscope structure [3].

The derivation of the Coriolis force expression is not simple. The Coriolis force is basically the cross multiple of angular and linear velocity of the moving subject [39]. The exact expression is:

$$A_{cor} = 2\left(\frac{d\vec{r}}{dt} \times \vec{w}\right) \tag{2.7}$$

where r is the linear motion vector and w is the rotation vector. The derivation of the Coriolis force expression can be found in calculus based physics books and in different references [1, 3, 39].

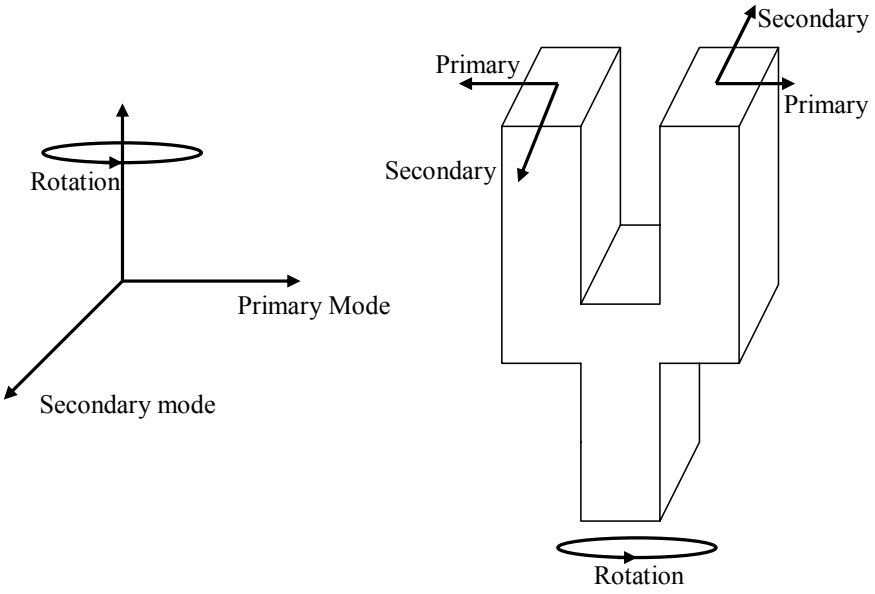

Figure 2.6: Coordinate system showing primary and secondary modes of a gyroscope with a tuning fork gyroscope structure [3].

2.4 Accelerometer and Gyroscope Models

This chapter explains the basic accelerometer and gyroscope models. The accelerometer can be modeled as a mass-spring-damper system where an external acceleration causes the proof mass to deflect from its rest position. The gyroscope can be modeled as a Coriolis acceleration sensing accelerometer. In the gyroscopes, there is a primary mode vibrator to create Coriolis acceleration under an external rotation.

2.4.1 Accelerometer Model

Figure 2.7 shows a general mass-spring-damper system. When there is an external acceleration the proof mass tends to move in the opposite direction of the acceleration due to Newton's law of motion. The proof mass movement is

determined by the beams that connect the proof mass to the fixed anchors and damping of the system.

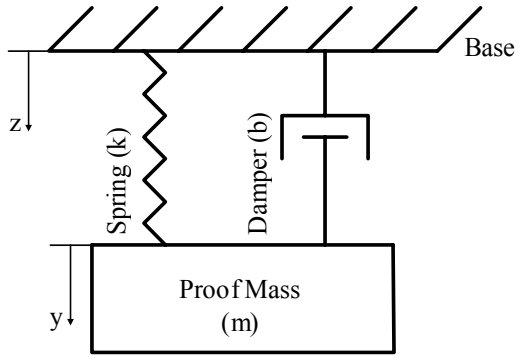

Figure 2.7: Accelerometer mass-spring-damper model.

The analysis of the dynamic behavior of the model gives us a general understanding of the accelerometer. The dynamic behavior can be extracted when we write the equation of the motion:

$$F = ma = m\ddot{x} + b\dot{x} + kx \tag{2.8}$$

where "a" is the external acceleration and "x" is the relative motion of the proof mass with respect to the base, i.e., x=y-z. If we take the Laplace transform of Equation 2.8, we get [40]:

$$ma(s) = ms^2 X(s) + bsX(s) + kX(s) \tag{2.9}$$

$$\frac{X(s)}{a(s)} = \frac{1}{s^2 + \frac{b}{m}s + \frac{k}{m}} \tag{2.10}$$

and

$$w_0 = \sqrt{\frac{k}{m}} \qquad Q = \frac{w_0 m}{b} \tag{2.11}$$

where w_0 is the resonance frequency of the accelerometer and Q is the quality factor. The magnitude and phase response of the proof mass motion with respect to input acceleration can be derived as:

$$\left|\frac{X(jw)}{a(jw)}\right| = \frac{1}{\sqrt{(w_0{}^2 - w^2)^2 + (\frac{ww_0}{Q})^2}} \tag{2.12}$$

$$\angle\frac{X(jw)}{a(jw)} = \tan^{-1}(\frac{\frac{ww_0}{Q}}{w_0{}^2 - w^2}) \tag{2.13}$$

Figure 2.8 shows the plot of the magnitude of proof mass displacement under a constant magnitude external acceleration versus acceleration frequency. The accelerometer is operated in the linear region of this plot due to the fact that the response is almost constant. The magnitude of the response in this linear region is inversely proportional to the square of the resonance frequency of the accelerometer. Hence, the mechanical resonance frequency is a very important parameter determining the performance of the accelerometer. The length of this linear region is called the effective bandwidth of the accelerometer. The effective bandwidth is also an important design parameter, and it is mainly related to the resonance frequency of the accelerometer. It should also be noted that, the definition of the effective bandwidth requires a better explanation of the length of the linear region. The linear region is not perfectly linear, but it shows a small response error. Figure 2.9 shows the focused view of this linear response region and indicates the response error. The effective bandwidth of the accelerometer is a design goal and the designer should design the accelerometer properly to achieve reasonably small response errors in that bandwidth.

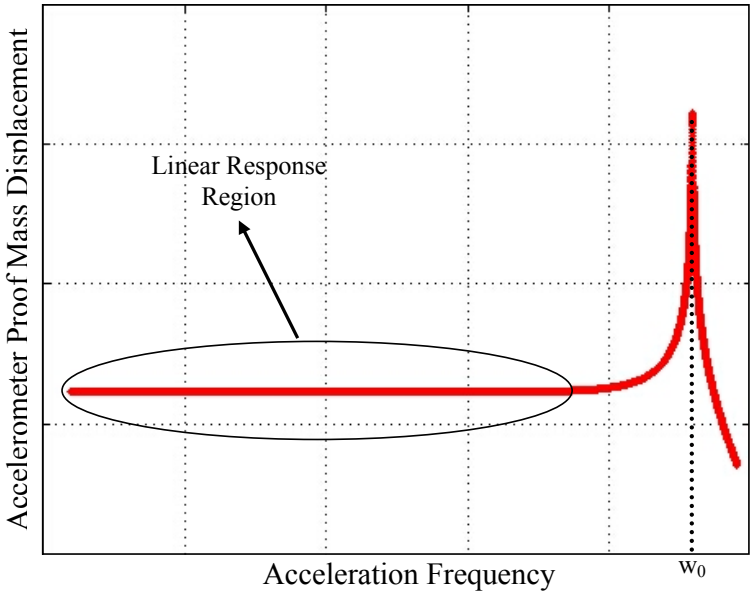

Figure 2.8: Accelerometer proof mass displacement under a constant amplitude acceleration versus acceleration frequency.

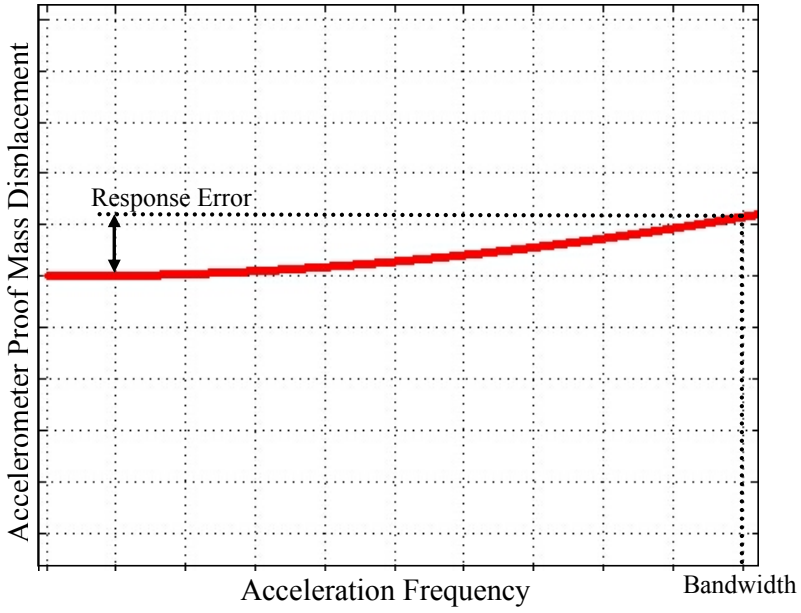

Figure 2.9: Focused view of the linear response region and the response error.

The effective bandwidth of the accelerometer or the response error in a predefined bandwidth is related to the resonance frequency and the quality factor of the system. Table 2-1 shows the response error of the accelerometer for 100 Hz effective bandwidth under different resonance frequency and quality factor values. The first observation according to the data provided in Table 2-1 is that when the frequency of the accelerometer increases for a fixed quality factor value, the response error decreases. Hence, to achieve a wider effective bandwidth, one can choose a higher resonance frequency. But, the resonance frequency of the accelerometer should be as low as possible to get a higher response values in that linear range because the proof mass displacement in that linear range is:

$$X = \frac{a}{w_0^{\,2}} \text{ (m)} \tag{2.14}$$

Hence, to find an optimum value between resonance frequency and the effective bandwidth is an important design issue. The second observation is, when the quality factor is 0.7, which means that the system is critically damped, very small response errors can be achieved with very small resonance frequencies [1, 41]. However, when the quality factor is changed slightly from 0.7, the response error is increased rapidly. The last important observation is the effect of higher quality factor values to response error. When the quality factor value is larger than 2, the response error for different resonance frequencies do not change significantly. To sum up above observations, to achieve a small response error in a fixed effective bandwidth, the design of the accelerometer can be done in two different ways. First way is to fix the quality factor at 0.7 and then to use a very small resonance frequency. This can be achieved with close loop configuration. The second way is to use a higher quality factor and to set resonance frequency 20-25 times more than the required effective bandwidth.

Table 2-1: Response error of the accelerometer for 100 Hz accelerometer effective bandwidth.

Accelerometer Effective Bandwidth (Hz)	Quality Factor	Resonance Frequency (Hz)	Response Error (%)
100	0.5	500	4.00
100	0.5	2000	0.24
100	0.7	500	0.18
100	0.7	750	0.06
100	2	750	1.58
100	2	2000	0.23
100	2	2500	0.15
100	5	2000	0.26
100	5	2500	0.15
100	100	2000	0.26
100	100	2500	0.15
100	1000	2000	0.26
100	1000	2500	0.15

In the quality factor expression given in Equation 2.11, the parameter that the designer has the least control is the damping factor, "b". The damping factor value of the accelerometer system depends on mainly air, structural, and thermal effects. The air damping results from the internal friction of the moving gas in small clearances between moving elements [42]. There are two main air damping effects namely "Squeeze-film damping", and "Coutte-flow damping". In Squeeze-damping effect, the air molecules are squeezed between two plates that are relatively moving towards each other. In Coutte-flow damping, the friction is occurred between two plates that are relatively moving parallel to each other. These to damping effects can be modeled and mathematical expressions can be obtained [43-44]. But these equations are obtained using some assumptions like having very large plates, hence they cannot hold in finger or etch hole regions of the MEMS sensors. Some sophisticated models for a better approach in solving this problem can be found in the literature [45-46]. However, the exact air damping calculation for specific device geometry is nearly impossible without using a FEM solver. Although an FEM solver can give some values for air damping, we cannot say the similar thing for structural damping. The structural damping is due to the energy loss in the structure of the MEMS device. The value of this damping is highly process dependent because even

the stiction of the anchor regions to the substrate is a source of this damping. The final main damping effect is the thermal damping. The main reason for this effect is the deviation of stress-strain relation with changing temperature [47]. It is very difficult for the designer to achieve a certain quality factor value due to the fact that each damping factor value extracted from the above sources is not accurate enough. However, this uncertainty in the quality factor may not be a disadvantage for the designer if he aims a quality factor value different than 0.7. From the observations that are derived from Table 2-1, we already know that the quality factor value more than 2 does not affect the response error significantly. Moreover, quality factor values smaller than 0.7 also gives similar response errors with quality factor values larger than 0.7. Hence, if the quality factor turns out to be different from what is expected in the design period, the performance of the accelerometer is not affected significantly.

The best way to achieve 0.7 quality factor is to use closed loop system [1]. In closed loop accelerometer, the proof mass is kept in its rest position using a feedback voltage proportional to the external acceleration [26]. Hence, the effects of air damping are removed due to the fact that the proof mass movement is negligibly small. So, the peak in the response plot of the accelerometer is suppressed, providing a large linear range. However, there is a major disadvantage of the close loop system, which is the complexity of the readout circuit. Although the highest performance values for accelerometers are achieved with close loop topology [7, 48], the accelerometers in this study are designed for open loop system because of the complex readout circuitry problem of the close loop systems.

2.4.2. Gyroscope Model

Figure 2.10 shows the general structure of a gyroscope. Gyroscopes are angular rate sensors, and for this purpose they use Coriolis acceleration. Due to this fact a gyroscope should have a vibratory motion generator which is needed for the generation of the Coriolis force which we call drive mode or primary mode of the

gyroscope and an acceleration sensing part to sense resultant Coriolis acceleration which we call sense mode or secondary mode.

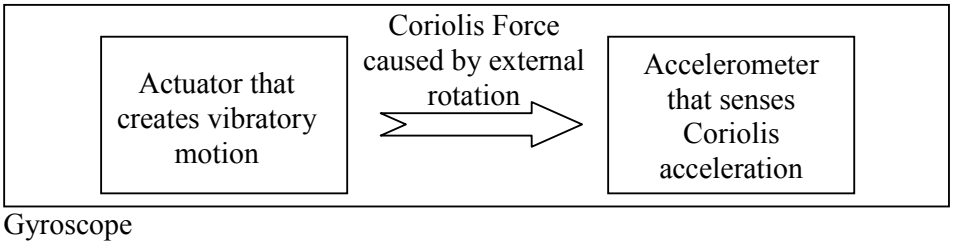

Figure 2.10: General structure of a gyroscope. The gyroscope is composed of an actuator part which creates the primary vibration, and an accelerometer part which senses Coriolis acceleration due to external rotation.

As we know from the Coriolis force generation, the Coriolis force acts on the object that makes the vibratory motion. Hence, in the gyroscope, the object that is making the vibratory motion should be the proof mass of the Coriolis acceleration sensing part. So, there is mechanical coupling between the vibratory motion, which is the primary mode or drive mode, and the Coriolis acceleration, which is the secondary mode or sense mode. Figure 2.11 shows three different coupling configurations of the gyroscopes. In the first configuration, when the gyroscope is vibrated in the drive mode, the sense mode also vibrates regardless of the external rotation, and similarly the drive mode is affected from the sense mode vibration. In the second configuration, the drive mode motion affects the sense mode directly, but the sense mode motion cannot affect the drive mode motion. In the third mode, which is the most advanced mode, the drive mode and sense mode are mechanically decoupled, and they do not affect each other. In this study, the gyroscopes are designed in the third configuration to achieve high performance gyroscopes.

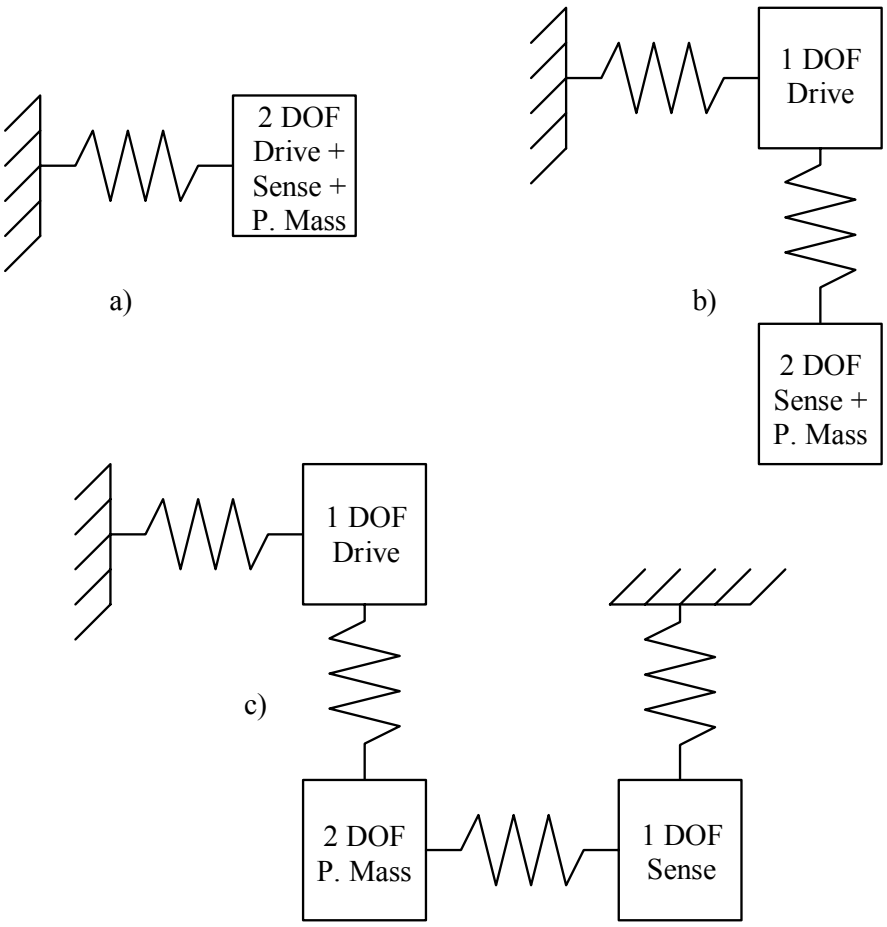

Figure 2.11: Different coupling modes of the gyroscopes. (a) shows the simplest configuration where the drive mode and the sense mode affects each other directly. (b) shows a more advanced configuration where the drive mode motion cannot be affected by the sense mode because it has only 1 degree of freedom (DOF) while it affects the sense mode. (c) shows the most advanced configuration where drive and sense modes have only 1 DOF and they are attached to each other with a 2 DOF proof mass [49].

Although the gyroscope has a Coriolis acceleration sensing accelerometer part, this accelerometer part does not act as a standard accelerometer. Figure 2.12 shows three different frequency choices of drive and sense mode of the gyroscope. The input rotation that will be transformed into Coriolis acceleration in the drive mode is carried to drive mode resonance frequency due to linear vibration of the drive mode. Hence, when a DC input rotation signal is applied, the resultant Coriolis acceleration will be a sinusoidal signal that has the frequency of the drive mode resonance

frequency. Similarly, when a timely varying input rotation signal is applied, the Coriolis acceleration frequency will be shifted according to the frequency of this input rotation. Hence, the sense mode should be capable of detecting acceleration inputs with the frequencies in the required bandwidth of the drive mode resonance frequency. In the part (a) of Figure 2.12 the resonance frequency of the sense mode is very large to achieve linear response for different Coriolis acceleration frequencies. From the accelerometer bandwidth-linear response observations, it is concluded that the sense mode resonance frequency of the gyroscope should be 20-25 times more than the drive mode resonance frequency to have a linear response. But, this will be a very inefficient solution because the signal levels at the output of the sense mode will be very low due to very high resonance frequency of the sense mode considering that the drive mode resonance frequencies of the gyroscopes are around few kHz. In the part (b) of Figure 2.12 the resonance frequencies of the drive mode and the sense mode of the gyroscope are designed to be mismatched, but their difference is not big as part (a). The response error is compensated with external electronics which is sensitive to Coriolis acceleration frequency. In the part (c) of Figure 2.12, the resonance frequencies of the drive and sense mode are designed to be matched. In this case, the magnitude of the Coriolis acceleration is multiplied with the quality factor of the system and so is very large compared to part (b) but 3dB bandwidth of the system is decreased. The response error is compensated with external electronics similarly.

In this study, the gyroscopes are designed to have matched resonance frequencies. But, due to fabrication errors that cannot be avoided, the gyroscopes will have slightly mismatched resonance frequencies [39]. So, in the gyroscope designs, there are also some control electrodes that can compensate this frequency mismatch. In the designs, there are also some electrodes that are put to cancel quadrature error which is due to misalignment of the drive mode axis with respect to sense mode axis [50-51].

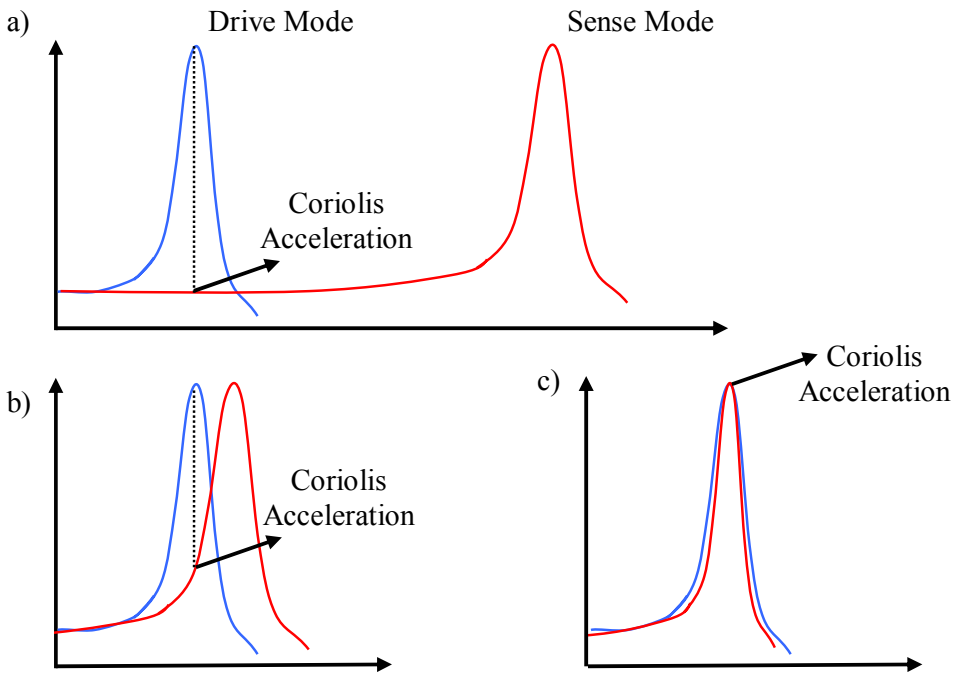

Figure 2.12: Three different frequency choices of the gyroscopes. (a) does not need any external circuit to compensate response error but this choice is not practical due to very low output signals. (b) shows mismatched resonance frequencies case and (c) shows matched resonance frequencies case. (c) shows a larger response compared to (b) but (b) has a wider 3dB bandwidth.

The sensitivity of the gyroscope is related with the amount of sense electrode vibration amplitude due to Coriolis acceleration. As in the accelerometer, we can say that if the resonance frequency of the sense mode is lowered, the sensitivity of the gyroscope also increases. However, especially in symmetric and decoupled topology that is used in this study, the quality factor value is also another factor that directly changes the sensitivity. The mathematical expression for the sense electrode vibration amplitude is:

$$Y_{sense} = \frac{\Omega Q X_{drive}}{\pi f} \tag{2.15}$$

where X_{drive} is the drive mode vibration amplitude, Q is the quality factor, Ω is the input rotation magnitude in rad/sec and f is the matched sense and drive mode resonance frequency [26].

2.5 Different Capacitive Sensing and Actuating Topologies

MEMS capacitance configurations can be characterized into three parts. First one is parallel plate capacitor configuration where the capacitance is formed between two parallel plates, second one is transverse comb capacitance configuration, and the third one is lateral comb capacitance configuration. First two configurations are used generally in sensing elements, and the last configuration is generally used in actuating schemes, due to its linear force-voltage relationship [52]. In this study, the accelerometer and gyroscope sensing schemes are formed using transverse comb configurations. Although lateral comb capacitance configuration gives a linear force-voltage relationship, the gyroscope actuating schemes are also formed using parallel plate configurations due to the requirements of the gyroscope topology. The following sections explain the capacitor basics and capacitance configurations in detail.

2.5.1 Capacitance Basics

Capacitance, sensitivity, electrostatic force, and electrostatic spring constant are the main performance metrics for the performances of the capacitance configurations. Table 2-2 shows the definitions of these performance metrics.

Table 2-2: Definitions of performance metrics for capacitance configurations

Capacitance	$N\varepsilon\frac{A}{d}$
Sensitivity	$\frac{\partial C}{\partial x}$
Electrostatic Force	$\frac{1}{2}\frac{\partial C}{\partial x}V^2$
Electrostatic Spring Constant	$\frac{1}{2}\frac{\partial^2 C}{\partial x^2}V^2$

where N is the number of capacitance plate pairs, A is the overlapping area, d is the distance between the plates, and ε is the permittivity constant.

2.5.2 Parallel Plate Capacitance Configuration

Figure 2.13 shows the parallel plate configuration. In this configuration there are two plates that are parallel to each other and the capacitance formed between these plates changes when the distance between these plates changes. This configuration is generally used to sense in the z-axis sensing schemes. Due to the possibility of large capacitance areas, this configuration may result very high sensitivity, but the main disadvantage of this configuration is the nonlinear force and sensitivity values, which occurs with the movement of one of the plates towards the other [52]. Table 2-3 summarizes the performance metrics for parallel plate capacitance configuration.

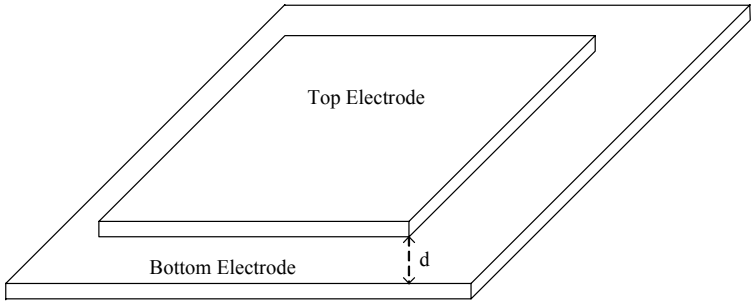

Figure 2.13: Parallel plate configuration.

Table 2-3: Parallel plate capacitance configuration performance metrics.

Capacitance	$N\varepsilon\frac{A}{d-x}$
Sensitivity	$-N\varepsilon\frac{A}{(d-x)^2}$
Electrostatic Force	$-\frac{1}{2}N\varepsilon\frac{A}{(d-x)^2}V^2$
Electrostatic Spring Constant	$N\varepsilon\frac{A}{(d-x)^3}V^2$

Another important parameter is the electrostatic spring constant. If the electrostatic spring constant trying to pull two electrodes towards each other is greater than the mechanical spring constant in that direction, "Pull-in" occurs. Analyses show that pull-in occurs when the distance of the two electrodes become 2/3 of the original distance. The voltage difference applied to the electrodes that causes pull-in is called pull-in voltage and can be calculated as [26]:

$$V_{pull-in} = \sqrt{\frac{8d^3k_{mech}}{27\varepsilon A}} \tag{2.16}$$

In this study, the actuator parts of the gyroscopes are designed using this idea. Although this topology introduces nonlinear force-voltage characteristics, the topologies of the gyroscopes required this method. However, the gyroscopes are not vibrated in the z-axis; instead electrodes are placed laterally to create lateral force.

2.5.3 Transverse Comb Capacitance Configuration

Figure 2.14 shows the transverse comb capacitance configuration. In this configuration there is a movable electrode between two stationary electrodes. Due to this differential topology, this configuration shows an almost linear force-displacement and voltage-displacement relationship. In addition to linearity,

this configuration gives a high sensitivity due to varying distance topology. The nonlinearity comes from fringing field capacitances and this effect is reduced if high aspect ratio fingers are used [52]. In this study, this method is used in the sensing parts of the sensors due to linearity and sensitivity concerns.

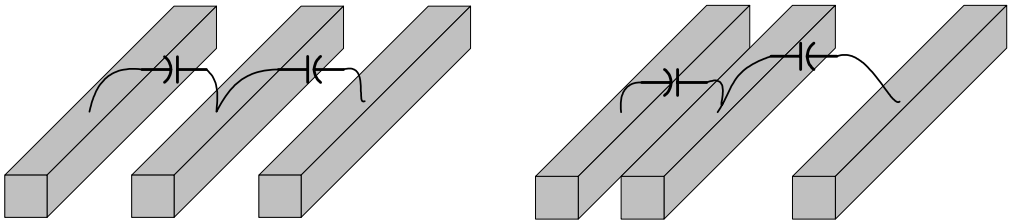

Figure 2.14: Transverse comb configuration: (a) before movement and (b) after movement.

Electrostatic force and electrostatic spring constant calculations for this configuration require a clear explanation of voltage sources applied to the electrodes. In this configuration, the general connection is to apply 0 and V_0 to fixed electrodes and to apply $V_0/2$ to the mid-electrode. The force occurs when the mid-electrode is not in the mid-point of two stationary electrodes. In fact, if the fixed electrodes are all applied with V_0 and the mod-electrode is applied with $V_0/2$, the same force expression can be found. In this study, the transverse comb capacitance configuration with the second voltage source connection idea is used for frequency tuning electrodes in the gyroscopes. Table 2-4 summarizes the performance metrics of transverse comb capacitance configuration.

Table 2-4: Transverse comb capacitance configuration performance metrics.

Capacitance	$2C_0 = 2N\frac{\varepsilon A}{d}$
Sensitivity	$\approx \frac{C_0}{d}$
Electrostatic Force	$\approx 2x\ \frac{C_0}{d^2}V^2$
Electrostatic Spring Constant	$\approx 2\frac{C_0}{d^2}V^2$

2.5.4 Lateral Comb Capacitance Configuration

Figure 2.15 shows the lateral comb capacitance configuration, and Table 2-5 gives the performance metrics of this configuration. In this configuration the capacitance forms between two combs looking each other. The change of the capacitance is formed by the change of the distance of these combs. This configuration shows a constant force-displacement characteristic, hence does not form an electrostatic spring constant, but has a very poor sensitivity due to varying overlap area topology. Due to this linearity and poor sensitivity this configuration is generally used in the actuating parts of the sensors. However, in this study this topology is not preferred in the drive ode of the gyroscopes due to the mechanical design of the gyroscopes.

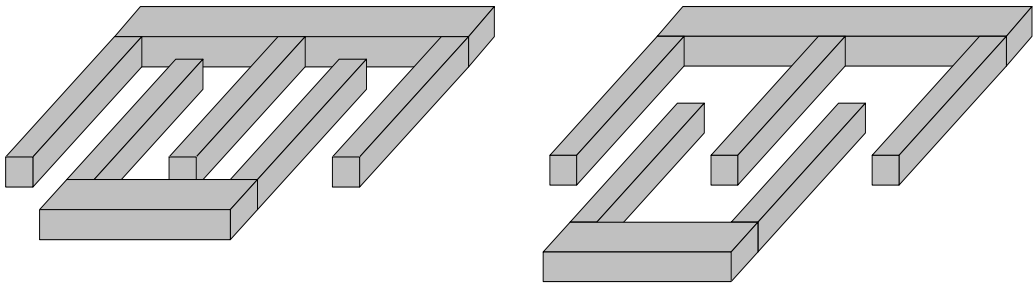

(a) (b)

Figure 2.15: Lateral comb configuration: (a) before movement and (b) after movement.

Table 2-5: Lateral comb capacitance configuration performance metrics.

Capacitance	$N\frac{\varepsilon A}{d}$
Sensitivity	$N\frac{\varepsilon h}{d}$
Electrostatic Force	$N\frac{\varepsilon h}{d}V^2$
Electrostatic Spring Constant	0

2.6 Summary

This chapter presents the theoretical background on the design of MEMS capacitive accelerometers and gyroscopes. The basic mechanical terms are introduced and Coriolis force concept is discussed. The models for accelerometers and gyroscopes are given, and some design parameters such as quality factor and bandwidth is studied. Lastly, the capacitive reading and actuating topologies are investigated for different performance indicators.

CHAPTER 3

MEMS ACCELEROMETERS AND GYROSCOPES DESIGN

This chapter gives the design details of MEMS accelerometers and gyroscopes. Section 3.1 gives the important parameters that are considered as the design challenges of the accelerometers, and Section 3.2 explains the important design parameters and challenges for gyroscopes. Section 3.3 gives the details of designed accelerometers and gyroscopes for three different processes with their estimated performances. Finally, Section 3.4 gives the summary of this chapter.

3.1 Design Parameters and Challenges for MEMS Accelerometers

The most common MEMS accelerometer design parameters are resolution, sensitivity (scale-factor), bandwidth, nonlinearity, bias drift, and scale factor asymmetry. To achieve the required design parameters, the first thing the designer should do is to choose a proper process. The process limitations directly affect the performance of the sensors. Moreover, some parameters like nonlinearity, bias drift and scale factor asymmetry cannot be estimated theoretically, because they are almost totally process dependent. Hence, the choice of the process is an important design issue. After choosing the process, the performance of the accelerometer can

be optimized with a proper mechanical design and with using a proper readout circuit. The design parameters of MEMS accelerometers are shortly explained below.

Resolution is defined as the noise floor of the accelerometer system. The noise sources in accelerometer system come from both mechanical and electrical parts of the system. The mechanical noise source is the Brownian noise [53], and is related with the mass and quality factor of the accelerometer mechanical part [26]. The electrical noise source is the readout electronics electronic noise. In today's accelerometers, due to high proof mass values, the mechanical noise floor is nearly neglected compared to electrical noise, but with a proper electrical circuitry design, electrical noise floor can be reduced significantly [7]. The unit of the resolution is g/√Hz or g in a fixed bandwidth where g is the earth gravity.

Sensitivity or scale-factor is the change in the response of the system to 1g acceleration. The unit of sensitivity can be F/g if the mechanical part sensitivity is considered only or V/g if mechanical part and readout circuitry is considered together. The voltage sensitivity is not an indicator of the performance of the accelerometer because with external amplifiers this sensitivity value can be arranged to any value. However, the capacitance sensitivity mainly shows the performance of the accelerometer mechanical part.

Bandwidth is the length of the frequency range that input signal frequency can vary. While calculating the bandwidth of the accelerometer 3dB concept may not be used. Instead, the maximum accelerometer response deviation with input acceleration frequency change defines the bandwidth of the system. The bandwidth vales are directly related to resonance frequency of the accelerometer.

Nonlinearity of the accelerometer is defined as the deviation of the accelerometer response from the best fit curve for different magnitudes of acceleration signal in its working range. Although the capacitive sensing topology may introduce nonlinearity, especially parallel plate capacitive sensing topology, this nonlinearity is almost insignificant compared to nonlinearity due to fabrication. The fabrication of the

sense capacitances does not yield perfectly matched capacitances and this mismatch causes nonlinearity.

Bias drift is defined as the maximum deviation of the accelerometer system output with time for a fixed input acceleration signal. The exact reasons of bias drift is not known very well but the reasons are believed to be the fabrication mismatches, the hysterical behaviors of the springs, the change of the mechanical properties of the material with different environment conditions, and the change of the performance of the readout circuit with different environment conditions.

Scale factor asymmetry is another parameter that is directly related to fabrication. The definition of the scale factor asymmetry is the percentage difference of scale factor best fit values for negative and positive acceleration inputs.

Other design parameters, which also affect the performance of the accelerometers, are temperature dependence of each other parameter, axis misalignment, cross-axis nonlinearities, and high order nonlinearity constants. Considering all the design parameters an accelerometer model can be constructed as [54]:

$$E_0 = K_1(K_0 + a_i + K_2 a_i^{\,2} + K_3 a_i^{\,3} + J_0 a_p + J_p a_0 + K_{ip} a_i a_p + K_{io} a_i a_o) \qquad (3.1)$$

E_0 : Accelerometer output

a_i, a_p, a_o : Acceleration inputs for each axis

K_0 : Bias

K_1 : Scale factor

K_2 : 2nd order nonlinearity

K_3 : 3rd order nonlinearity

J_o, J_p : Misalignment

K_{ip}, K_{io} : Cross-axis nonlinearities

In this study scale factor, bias, total nonlinearity, and resolution are considered as design parameters. The misalignment in the axis is packaging related problem and is not considered as a design parameter in this study.

Considering these design parameters, it can be concluded that a proper fabrication is one of the main issues for high performance accelerometers. A proper fabrication will significantly reduce undesired nonlinearities. Next important issue is the readout circuitry because readout circuit plays an important role in the resolution of the accelerometer. After choosing the process and the readout circuitry, the mechanical designs can be realized.

3.2 Design Parameters and Challenges for MEMS Gyroscopes

The most common MEMS gyroscope design parameters are resolution, sensitivity (scale factor), bandwidth, nonlinearity, and bias drift. The definitions of these parameters are similar to accelerometer parameters with some minor distinctions.

The gyroscope design requires a good topology selection, a well arranged drive and sense mode resonance frequencies, and a low noise readout circuitry. Due to the fact that gyroscope topology requires the design of two different resonance modes, the topology is more complex than the accelerometer topology. The complex topology also introduces some unwanted resonance modes that causes cross axis sensitivity. Hence the topology should be carefully designed and should be verified with FEM simulators. Selecting the topology is also correlated to selecting the resonance frequencies of drive and sense modes. From the bandwidth-sensitivity trade-off, either the frequencies should be matched to achieve large sensitivity, or the frequencies should be slightly mismatched to achieve a wider 3dB bandwidth. To have matched resonance frequencies, the best solution is to have identical spring structures and equal masses for these modes, to minimize fabrication errors and frequency shift due to environmental condition changes. Hence in matched resonance frequency gyroscope design, the topology should allow to have identical

spring structures and identical masses for drive and sense modes. The choice of the resonance frequencies for these modes is also another design issue. Selecting a low resonance frequency increases the sensitivity but also increases the effects of unwanted environment accelerations. To sum up, designing the topology of the gyroscope is one of the main design challenges that must be carefully handled.

The packaging issue is another design challenge for gyroscopes. In the matched frequency case, the quality factor of the gyroscope directly includes in the sensitivity expression. Hence, to achieve high sensitive gyroscopes the design should have a high quality factor value. The most effective solution to achieve high quality factor values is to have the sensor vacuum packaged.

The readout part is also very important to have a high performance gyroscope. The front-end circuit element for the gyroscopes is generally unity gain buffers with low input capacitances [55]. This buffer should be also very low noise to sense very small output voltages. The second challenge in the gyroscope readout is the control loops. These loops start up the drive mode, fix the drive voltage frequency to resonance frequency of the drive mode, fix the drive mode vibration magnitude, and cancel out the quadrature error [39].

3.3 Accelerometers and Gyroscopes Designed In This Study

This section explains the accelerometers and gyroscopes designed in this study. Section 3.3.1 explains the accelerometer topology and gives the FEM simulations for this topology. Section 3.3.2 explains the gyroscope topology and gives FEM simulations for this topology. Section 3.3.3 gives the design considerations for three different processes that are used in this study. Section 3.3.4 gives the performance estimations for the designed accelerometers and gyroscopes.

3.3.1 Accelerometer Topology

Figure 3.1 shows the topology of the designed accelerometer, which is a lateral accelerometer. There are two symmetrical double-folded springs that connects the suspended proof mass to the fixed anchor points. When there is an external acceleration, the proof mass moves along the line passing through the anchor points in the direction of opposite to the applied acceleration. This movement causes a differential capacitance difference in the simplified transverse comb capacitance sensing scheme. The external readout circuitry senses this differential capacitance difference and gives a voltage output related to the acceleration input.

The springs and the proof mass are the main elements that determine the resonance frequency of the accelerometer. The mass part is usually selected as big as the process allows, to have more sense capacitance fingers. So, to achieve the desired resonance frequency, the designer usually fixes the mass to its maximum value and plays with the spring constants. The reasons for using folded springs in this study are to achieve a low resonance frequency, hence a higher sensitivity, and also to decrease the total stress under an external shock. In some designs double-folded springs are used to realize even lower resonance frequencies and lower stress values, while some accelerometers have conventional folded springs to achieve higher resonance frequencies for wide bandwidth applications. The mathematical expression that gives the spring constant value for double-folded springs is:

$$k = \frac{1}{2} E \frac{hw^3}{l^3} \tag{3.2}$$

where, E is the Young's modulus, h is the height of the spring structure, w and l are the width and length of each individual spring beams that forms the double-folded spring structure, respectively. This value is half of the conventional folded spring constant. Due to this fact, the resonance frequency of the accelerometer with the same mass can be lowered with the ratio of $\sqrt{2}$. The second reason to have folded springs is the stress issue. When there is an external acceleration shock, the

maximum movement will be amount of the sense finger spacing if we assume that the rigidity of these fingers will not be deformed. Using stress expressions in [38], the maximum stress occurred in the structure for a fixed movement, x, is calculated as:

$$Stress_{\max} = 3E\frac{w}{l^2}x \tag{3.3}$$

This total stress is divided equally between each spring beam forming the folded spring structure. Hence the stress for each beam is reduced significantly. Table 3-1 shows comparison of stress formulation with the FEM simulation results.

Figure 3.2 shows transverse comb capacitance configuration and simplified transverse comb capacitance configuration. The original configuration shows a higher sensitivity compared with the simplified one, but the fabrication of original one is rather difficult. Not only the rigidity of the small anchors is a problem, but also the parasitic capacitances between proof mass fingers and the small anchors cause undesired capacitance mismatch. Due to these facts, simplified transverse comb structure is selected in this study.

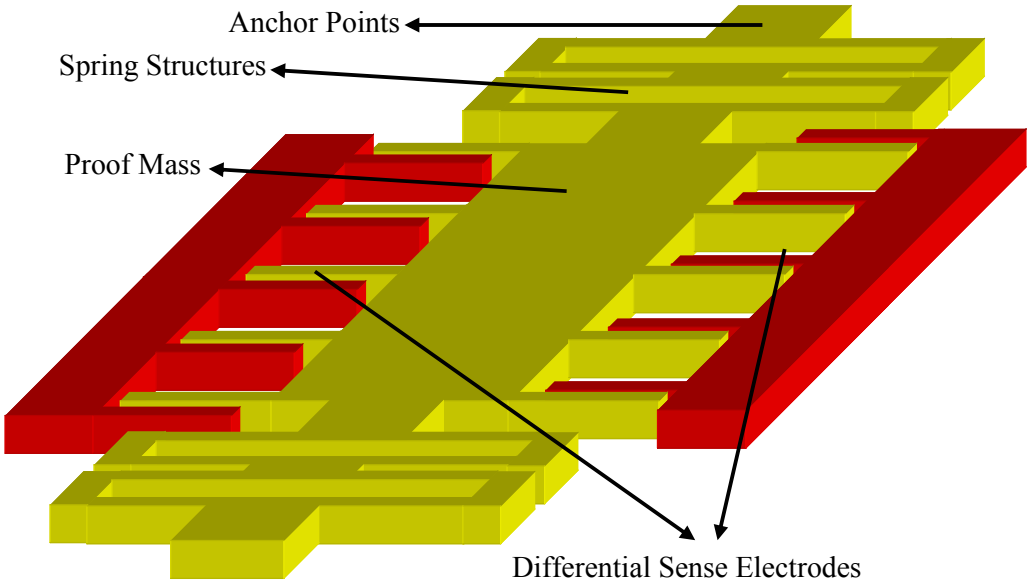

Figure 3.1: The topology of the designed accelerometers, which is the lateral accelerometer topology.

Table 3-1: The comparison of stress formulation with the FEM simulations. It is seen that the formulation result shows very similar results with the simulation results, and the stress value decreases with increasing folded beam legs.

Beam		**l (μm)**	**Formulation Result**	**Simulation Result**
Clamped		400	82.5 MPA	86 MPA
Clamped		500	52.8 MPA	54 MPA
Folded	2 Leg	500	26.4 MPA	27 MPA
	8 Leg	500	6.6 MPA	6.4 MPA
	8 Leg	700	3.4 MPA	3.3MPA
	20 Leg	500	2.6 MPa	2.5MPa
	20 Leg	700	1.3 MPa	1.4MPa

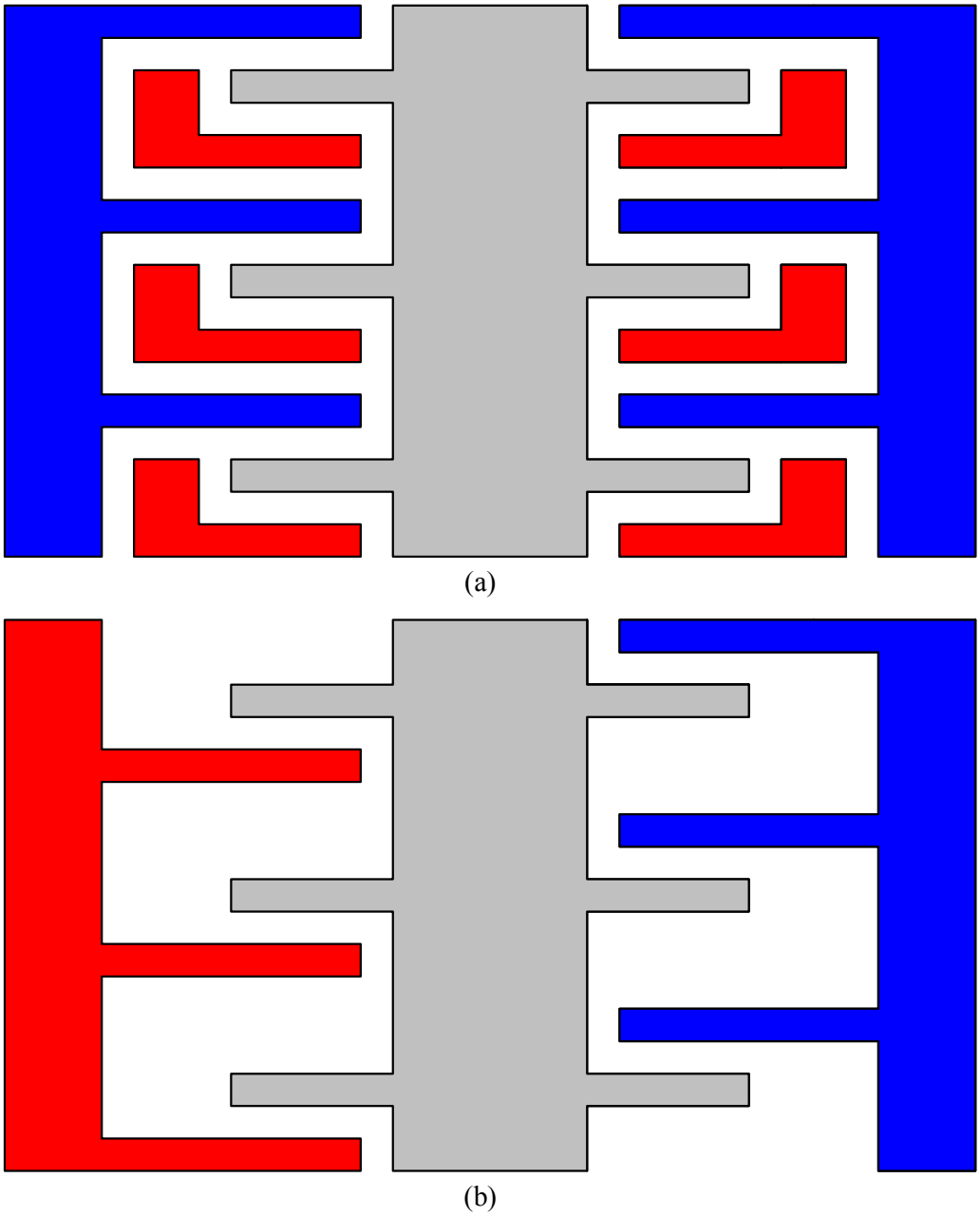

Figure 3.2: Two different configurations that can be used in accelerometers: (a) Transverse comb capacitive configuration, (b) simplified transverse comb capacitance configuration.

The resonance modes of the accelerometer are found using CoventorWare FEM simulator. The resonance modes are topology dependent, but the mechanical properties and the dimensions of the sensor determine the frequencies of each mode.

Figure 3.3 shows a FEM simulation result for determining the resonance modes of the accelerometer topology. This simulation is important to estimate the cross sensitivity of the accelerometer. The accelerometer should have only one resonance mode ideally, which is its sensitive mode, but it has also some unwanted resonance modes. When there is an external acceleration that causes the accelerometer to move along its unwanted resonance mode, this movement should be as low as possible not to create cross-axis sensitivity. To achieve that, the difference between resonance frequencies of sensitive mode and the cross mode should be as high as possible.

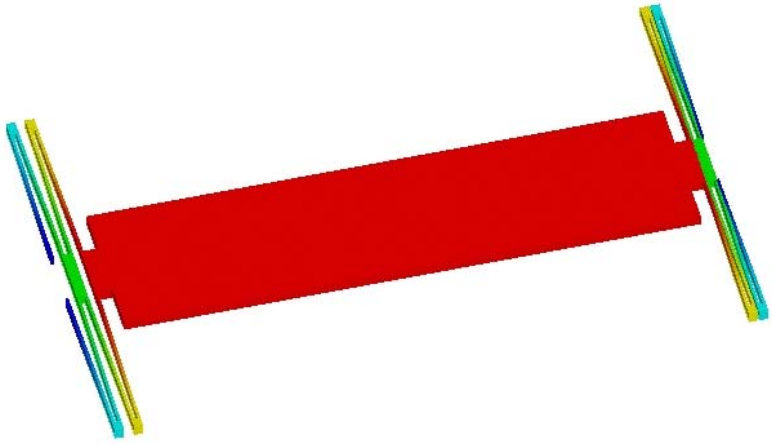

(a)

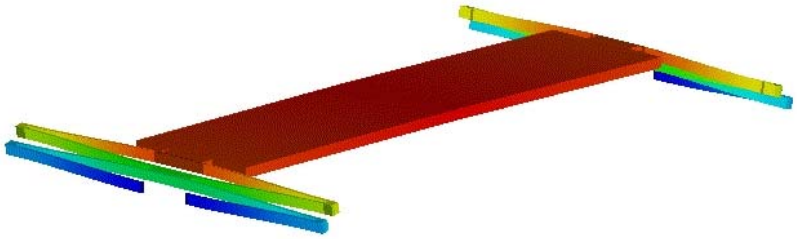

(b)

Figure 3.3: FEM simulation results for determining the resonance modes of the accelerometer topology: (a) the desired sensitivity mode, (b) the unwanted cross mode.

3.3.2 Gyroscope Topology

Figure 3.4 shows the topology of the designed gyroscope, which is a z-axis sensitive gyroscope. The gyroscope is driven in the drive mode with two symmetrical drive mode fingers. When there is an external rotation in the z-axis, the Coriolis acceleration causes the proof mass to move also in the sense mode. The sense electrodes also move in the sense mode and create a differential capacitance change in the sense mode fingers. A low noise interface circuitry senses this differential capacitance difference and turns this difference into voltage signal.

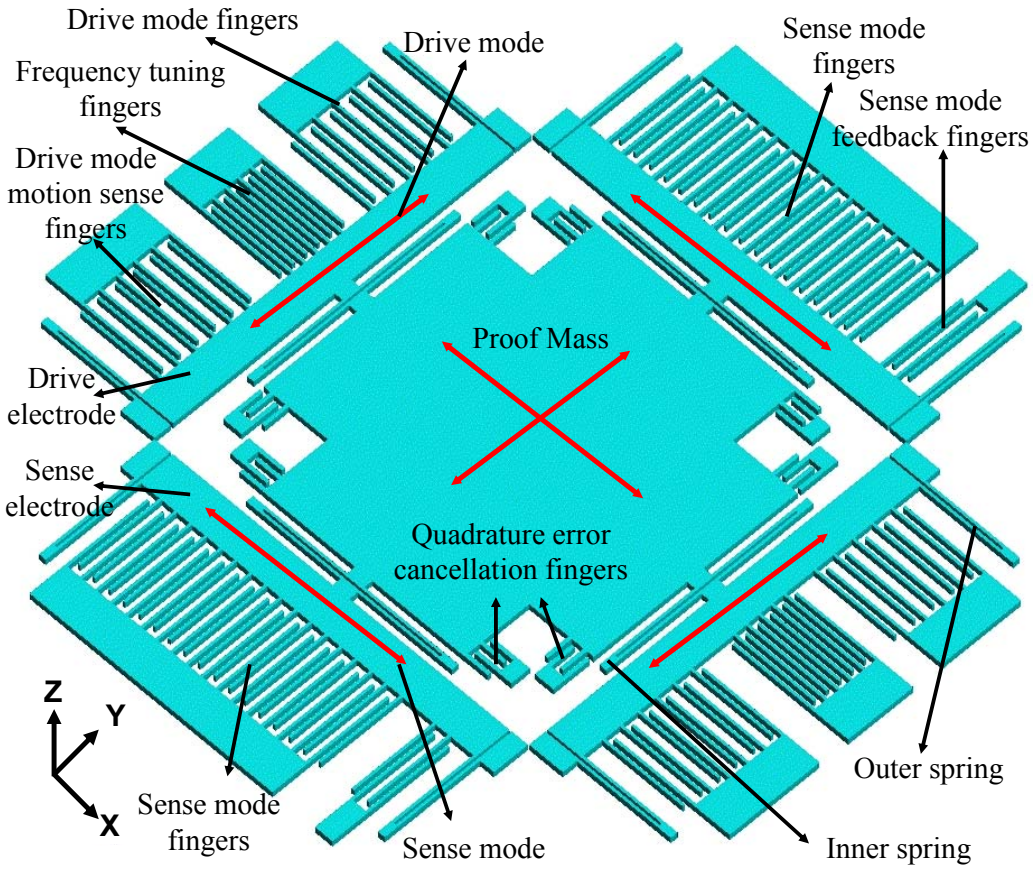

Figure 3.4: The topology of the designed gyroscope. The proof mass has 2DOF (degree of freedom) while sense and drive mode electrodes have 1DOF. Drive electrodes mechanically cannot move in the sense mode, and sense electrodes mechanically cannot move in the drive mode due to the decoupled mechanical design of the gyroscope.

The gyroscope is a symmetrical and decoupled gyroscope to achieve a high sensitivity [3]. Springs are all identical in shape in two modes and the drive mode and the sense mode has the same mass values. This provides a symmetrical operation. However, due to electrical spring constant difference in sense and drive mode, and to cancel fabrication errors in resonance frequencies, drive mode has some frequency tuning fingers. These fingers create an electrical spring constant in the drive mode and may decrease the drive mode frequency in some range relative to the applied DC voltage on them [56]. Hence, the drive mode resonance frequency is designed to be a little more than the sense mode resonance frequency. The decoupled operation of the gyroscope is provided by the inner and outer springs. The outer springs connect the electrodes to the anchor points and the inner springs connect the proof mass to the electrodes. Moreover, the springs are designed so that the outer springs do not allow the sense electrode to move in the drive mode, and the drive electrode to move in the sense mode. And the inner springs provides the proof mass to have 2 degree of freedom. This provides the decoupled operation.

The quadrature error cancellation electrodes are to cancel the misaligned movement of the proof mass. When the proof mass vibrates in the drive mode, it may have a motion component in the sense mode due to fabrication errors. This motion component of the proof mass causes sense mode electrodes to move. Hence, it causes a differential capacitance difference in the sense mode electrodes and affects the output. To cancel out this unwanted component, the quadrature error cancellation electrodes apply proper electrostatic force to the proof mass [51].

The gyroscope has also sense mode feedback fingers. These fingers are designed to create an analog feedback force to cancel out the sense mode motion [57]. Hence, when there is an external rotation signal, the Coriolis acceleration forces the proof mass to move in the sense mode. The inner springs force the sense electrode to follow the motion of the proof mass in the sense axis. Then, the feedback fingers in the sense mode give a proper electrostatic force to the sense electrode to cancel this motion. Hence, the magnitude of the rotation signal is proportional to the magnitude of the voltage signal applied to the feedback fingers.

The resonance modes of the gyroscope topology are found using CoventorWare FEM simulator. Figure 3.5-7 show the resonance modes of the gyroscope topology. There are two designed modes which are drive mode and the sense mode. The resonance frequencies of these modes should be very similar to each other with drive mode resonance frequency being slightly larger. It can be seen that when the gyroscope is moving in one mode, the electrode of the other mode does not move. This is due to decoupled operation. The third mode is the unwanted cross mode. This mode is a z-axis resonance mode and directly related to the height of the sensor. Hence, this mode resonance frequency may be larger or lower than the drive and sense mode resonance frequency due to different processes providing different sensor heights.

Drive mode fingers have parallel plate capacitance topology. When this topology is used in the actuators, nonlinear force-displacement characteristics occur. However this nonlinearity can be negligible if the maximum drive mode displacement is very small compared to drive mode finger spacing. Due to this fact, drive mode finger spacing is the biggest spacing in the topology. The frequency tuning fingers are designed as transverse comb capacitance configuration with both stationary fingers being applied to same voltage potential. This topology is achieved with connecting all the stationary fingers to the same anchor.

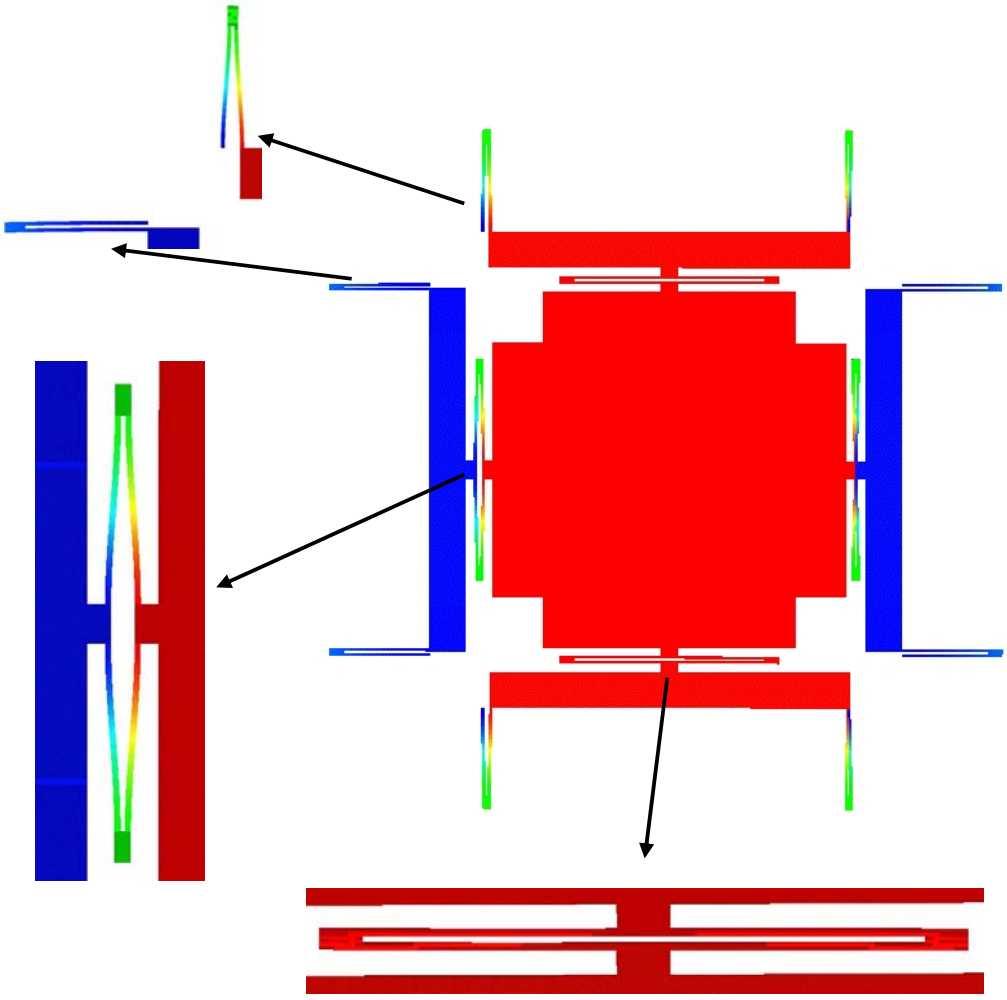

Figure 3.5: Simulation result of sense mode of the gyroscope using CoventorWare FEM simulator. Drive mode electrodes do not move in the sense mode verifying the decoupled operation.

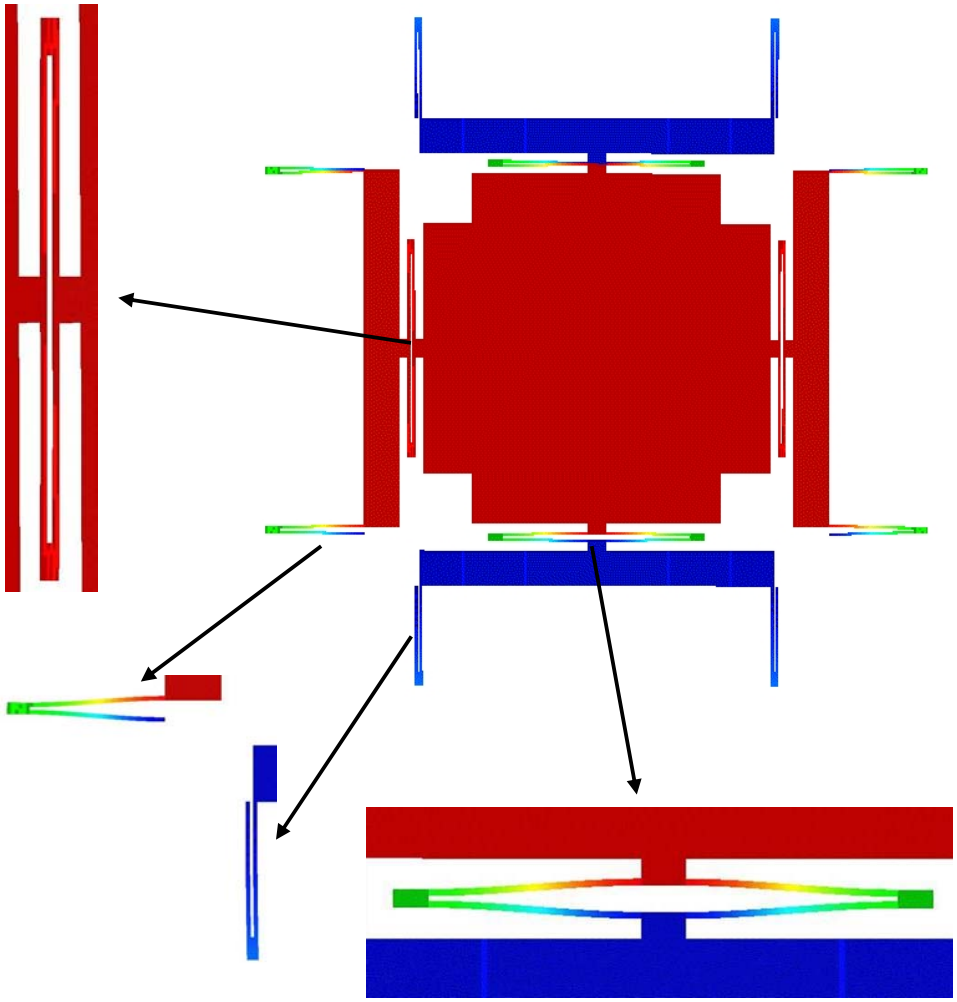

Figure 3.6: Simulation result of drive mode of the gyroscope using CoventorWare FEM simulator. Sense mode electrodes do not move in the drive mode verifying the decoupled operation.

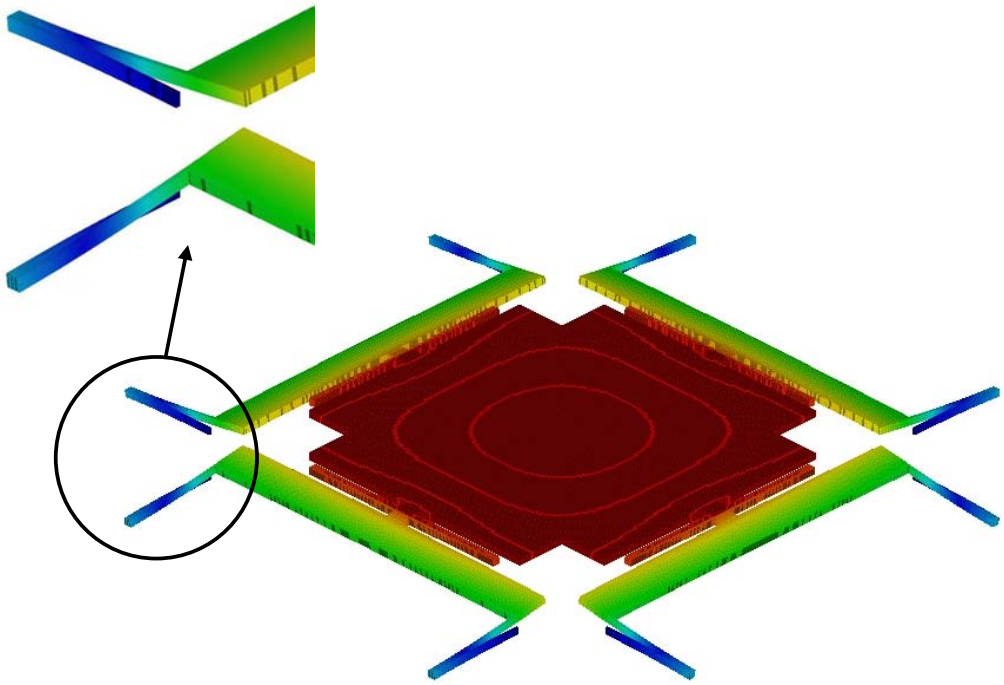

Figure 3.7: Cross mode of the gyroscope topology. This mode is an unwanted mode and the resonance frequency of this mode should be as far as possible from the drive/sense mode resonance frequencies.

3.3.3 Design Considerations for Three Different Processes

In this study, three different processes are considered to fabricate MEMS accelerometers and gyroscopes. These processes are the SOIMUMPs process, electroplating process, and DRIE process. The details of these processes are given in Chapter 4. However, the design of each MEMS sensor is limited by the fabrication process. Some important dimensions like height and minimum spacing are determined by the fabrication. Moreover, the critical dimensions of the sensors may change with the fabrication errors. If the fabrication is adequately understood, these fabrication errors can be compensated with a proper design.

The SOIMUMPs process is a commercial MUMPs (Multi-User MEMS Processes) provided by CRONOS Inc. The process uses upper silicon of SOI wafers for the

structural material and patterns this layer with DRIE providing 10 μm silicon structural layer with a 2 μm minimum line and gap spacing [58]. The most important design considerations are the minimum line and gap spacing, maximum comb finger length, and die length.

The nickel electroplating process is realized with the facilities in METU-MET. The process starts with glass wafers and creates patterned nickel structures with electroplating using a thick photoresist mold. The main design consideration in this process is the change in the critical dimensions due to the change in the dimensions of the photoresist mold. During the exposure of the photoresist, the photoresist mold tries to increase the dimensions of the structural parts and so decrease the dimensions of the spacing parts. This change in the dimensions is most critical in finger regions and in spring regions. Without considering this change, the small finger spacing may vanish due to shrinking, and the resonance frequency of the sensor may come up to be larger then expected due to the increase of the widths of the springs. With our previous studies [11], the magnitude of this dimension change is estimated. Considering a typical mold of thickness more then 15 μm, we can say that the structural regions try to increase by 1 μm in each direction, hence the spacing parts try to decrease by 1 μm in each direction. In this study, all the Ni electroplating designs, calculations, and FEM simulations are done considering this dimension change.

The DRIE process is also developed to be done at the facilities in METU-MET. The process starts with a glass wafer. The structural layer is silicon, and it is anodic bonded to the glass wafer. The DRIE machine patterns the structural layer. The main design consideration in DRIE process is the silicon etching step. In this step, the dimensions of the etched parts, which are the spacing parts, tend to increase [18, 59]. This change is the opposite of Ni electroplating process. The magnitude of the dimension change changes with conditions, and the conditions is not optimized yet but we consider a change of 1-2 μm [18, 59]. Hence in this study the critical structural dimensions in DRIE process are designed to be more than desired value and the critical spacing parts are designed to be smaller than the desired value.

3.3.4 Performance Estimations for the Designed Accelerometers and Gyroscopes

In this study, eight different accelerometer prototypes are designed with two of them having conventional folded springs and six of them having double-folded springs. In addition to accelerometers, four different gyroscope prototypes are designed. The accelerometer topologies in these prototypes are the same except the spring types, but the dimensions and the fabrication process are different. Similarly, the gyroscope topologies are identical for each process but the dimensions are different.

Table 3.2-9 summarizes the designed accelerometer prototypes. Each table gives the fabrication process, sensor size, mass and thickness of the proof mass, calculated and simulated resonance frequency, sense capacitance, sensing gap distance, and capacitive sensitivity of the corresponding accelerometer. In the calculations Young's Modulus of the nickel and silicon are taken as 150 GPa and 130 GPa, respectively; while the densities of nickel and silicon are taken as 8910 kg/m^3 and 2330 kg/m^3, respectively.

Table 3-2: The summary of accelerometer prototype-1.

Fabrication process	SOIMUMPs
Sensor size	1400μm x 980μm
Mass of the proof mass	$7.32x10^{-9}$ g
Thickness of the proof mass	10 μm
Spring type	Conventional folded
Sense finger gap	2 μm
Sense capacitance	2 x 520 fF
Calculated resonance frequency *	31.5 kHz
Simulated resonance frequency	31.2 kHz
Simulated cross mode resonance frequency	34.2 kHz
Calculated mechanical noise	207 μg/√Hz
Expected open loop bandwidth	1.5 kHz
Sensitivity	0.13 fF/g

* Electrostatic spring constant calculation is included.

Table 3-3: The summary of accelerometer-prototype-2

Fabrication process	SOIMUMPs
Sensor size	1400µm x 980µm
Mass of the proof mass	7.32×10^{-9} g
Thickness of the proof mass	10 µm
Spring type	Conventional folded
Sense finger gap	2.5 µm
Sense capacitance	2 x 415 fF
Calculated resonance frequency *	11.1 kHz
Simulated resonance frequency	11.4 kHz
Simulated cross mode resonance frequency	17.1 kHz
Calculated mechanical noise	125 µg/√Hz
Expected open loop bandwidth	500 Hz
Sensitivity	0.67 fF/g

* Electrostatic spring constant calculation is included.

Table 3-4: The summary of the accelerometer prototype-3.

Fabrication process	SOIMUMPs
Sensor size	1400µm x 980µm
Mass of the proof mass	7.32×10^{-9} g
Thickness of the proof mass	10 µm
Spring type	Double-folded
Sense finger gap	2 µm
Sense capacitance	2 x 520 fF
Calculated resonance frequency *	3.73 kHz
Simulated resonance frequency	4.25 kHz
Simulated cross mode resonance frequency	9.24 kHz
Calculated mechanical noise	71.0 µg/√Hz
Expected open loop bandwidth	150 Hz
Sensitivity	9.25 fF/g

* Electrostatic spring constant calculation is included.

Table 3-5: The summary of accelerometer prototype-4.

Fabrication process	Nickel electroplating
Sensor size	1390μm x 890μm
Mass of the proof mass	4.34×10^{-8} g
Thickness of the proof mass	19 μm
Spring type	Double-folded
Sense finger gap	2.5 μm
Sense capacitance	2 x 557 fF
Calculated resonance frequency *	2.66 kHz
Simulated resonance frequency	2.68 kHz
Simulated cross mode resonance frequency	8.44 kHz
Calculated mechanical noise	24.5 μg/√Hz
Expected open loop bandwidth	100 Hz
Sensitivity	15.70 fF/g

* Electrostatic spring constant calculation is included.

Table 3-6: The summary of accelerometer prototype-5.

Fabrication process	Nickel electroplating
Sensor size	1890μm x 1240μm
Mass of the proof mass	1.31×10^{-7} g
Thickness of the proof mass	19 μm
Spring type	Double-folded
Sense finger gap	3 μm
Sense capacitance	2 x 696 fF
Calculated resonance frequency *	2.05 kHz
Simulated resonance frequency	2.05 kHz
Simulated cross mode resonance frequency	5.37 kHz
Calculated mechanical noise	12.7 μg/√Hz
Expected open loop bandwidth	100 Hz
Sensitivity	27.41 fF/g

* Electrostatic spring constant calculation is included.

Table 3-7: The summary of accelerometer prototype-6.

Fabrication process	Nickel electroplating
Sensor size	1890µm x 1240µm
Mass of the proof mass	1.31×10^{-7} g
Thickness of the proof mass	19 µm
Spring type	Double-folded
Sense finger gap	3 µm
Sense capacitance	2 x 696 fF
Calculated resonance frequency *	1.54 kHz
Simulated resonance frequency	1.57 kHz
Simulated cross mode resonance frequency	4.86 kHz
Calculated mechanical noise	10.9 µg/√Hz
Expected open loop bandwidth	75 Hz
Sensitivity	48.84 fF/g

* Electrostatic spring constant calculation is included.

Table 3-8: The summary of the accelerometer prototype-7.

Fabrication process	DRIE
Sensor size	2500µm x 1600µm
Mass of the proof mass	2.78×10^{-7} g
Thickness of the proof mass	100 µm
Spring type	Double-folded
Sense finger gap	3 µm
Sense capacitance	2 x 5.12 pF
Calculated resonance frequency *	2.97 kHz
Simulated resonance frequency	3.29 kHz
Simulated cross mode resonance frequency	21.86 kHz
Calculated mechanical noise	2.7 µg/√Hz
Expected open loop bandwidth	150 Hz
Sensitivity	48.01 fF/g

* Electrostatic spring constant calculation is included.

Table 3-9: The summary of accelerometer prototype-8.

Fabrication process	DRIE
Sensor size	2950µm x 2100µm
Mass of the proof mass	1.08×10^{-6} g
Thickness of the proof mass	200 µm
Spring type	Double-folded
Sense finger gap	5 µm
Sense capacitance	2 x 10.5 pF
Calculated resonance frequency *	2.76 kHz
Simulated resonance frequency	2.79 kHz
Simulated cross mode resonance frequency	19.96 kHz
Calculated mechanical noise	1.3 µg/√Hz
Expected open loop bandwidth	125 Hz
Sensitivity	68.75 fF/g

* Electrostatic spring constant calculation is included.

We can conclude that a high performance accelerometer design is directly related with the accelerometer resonance frequency and the chosen technology. If the accelerometer resonance frequency is lowered, the movement response of the proof mass to a fixed amplitude acceleration signal will increase; hence the sensitivity will increase at the expense of open loop bandwidth. Moreover, if the technology allows high aspect ratio sense structures with high capacitance values, the sensitivity will also increase significantly.

Table 3.10-13 summarizes the designed gyroscopes. The gyroscope properties are more than that of the accelerometers including dimensions of the die, mass and thickness of the proof mass, sense finger gaps, sense capacitance, calculated and simulated drive and sense mode resonance frequencies, simulated cross mode resonance frequencies, expected drive mode vibration magnitude, and the polarization voltage.

Table 3-10: The summary of the gyroscope prototype-1.

Fabrication process	SOIMUMPs
Sensor size	2050µm x 2050µm
Mass of the proof mass	1.44×10^{-8} g
Thickness of the proof mass	10 µm
Sense finger gap	2 µm
Sense capacitance	2 x 153 fF
Calculated drive mode resonance frequency	15.82 kHz
Calculated sense mode resonance frequency	15.70 kHz
Simulated drive mode resonance frequency	14.34 kHz
Simulated sense mode resonance frequency	14.16 kHz
Simulated cross mode resonance frequency	7.09 kHz
Drive mode vibration amplitude	0.1 µm
Polarization voltage	10 V
Expected quality factor in vacuum	300
Sensitivity	1.62 aF/(°/sec)

Table 3-11: The summary of the gyroscope prototype-2.

Fabrication process	Nickel Electroplating
Sensor size	2200µm x 2200µm
Mass of the proof mass	1.96×10^{-7} g
Thickness of the proof mass	19 µm
Sense finger gap	3 µm
Sense capacitance	2 x 363 fF
Calculated drive mode resonance frequency	6.07 kHz
Calculated sense mode resonance frequency	6.05 kHz
Simulated drive mode resonance frequency	5.95 kHz
Simulated sense mode resonance frequency	5.94 kHz
Simulated cross mode resonance frequency	4.26 kHz
Drive mode vibration amplitude	0.1 µm
Polarization voltage	10 V
Expected quality factor in vacuum	300
Sensitivity	6.67 aF/(°/sec)

Table 3-12: The summary of the gyroscope prototype-3.

Fabrication process	DRIE
Sensor size	3530µm x 3530µm
Mass of the proof mass	7.64×10^{-7} g
Thickness of the proof mass	100 µm
Sense finger gap	3 µm
Sense capacitance	2 x 1.97 pF
Calculated drive mode resonance frequency	6.57 kHz
Calculated sense mode resonance frequency	6.54 kHz
Simulated drive mode resonance frequency	6.36 kHz
Simulated sense mode resonance frequency	6.34 kHz
Simulated cross mode resonance frequency	8.63 kHz
Drive mode vibration amplitude	0.1 µm
Polarization voltage	10 V
Expected quality factor in vacuum	300
Sensitivity	33.40 aF/(°/sec)

Table 3-13: The summary of the gyroscope prototype-4.

Fabrication process	DRIE
Sensor size	3530µm x 3530µm
Mass of the proof mass	1.53×10^{-6} g
Thickness of the proof mass	200 µm
Sense finger gap	5 µm
Sense capacitance	2 x 2.36 pF
Calculated drive mode resonance frequency	6.57 kHz
Calculated sense mode resonance frequency	6.54 kHz
Simulated drive mode resonance frequency	6.63 kHz
Simulated sense mode resonance frequency	6.66 kHz
Simulated cross mode resonance frequency	9.04 kHz
Drive mode vibration amplitude	0.1 µm
Polarization voltage	10 V
Expected quality factor in vacuum	300
Sensitivity	23.04 aF/(°/sec)

Similar to the accelerometer conclusion, we can say that to decrease the resonance frequencies of the gyroscope and to use a better process providing higher aspect ratio with higher capacitance values will increase the sensitivity of the gyroscope. Moreover, if the quality factor value is increased, due to symmetric operation principle, the sensitivity of the gyroscope will also increase.

3.4 Summary

This chapter presents the design considerations of MEMS accelerometers and gyroscopes and explains the designed sensors. In MEMS accelerometers and gyroscopes, the main considerations for the evaluation of the sensor are the resolution, scale factor, bias drift, and bandwidth. To realize a high performance sensor, each design consideration must be handled carefully.

In this study, we have designed 8 accelerometer prototypes, and 4 gyroscope prototypes. For the realization of these prototypes, we have used three different fabrication processes. The fabrication errors from these processes are also considered in each design. The next chapter explains the details of the fabrication processes used in this study.

CHAPTER 4

MEMS ACCELEROMETERS AND GYROSCOPES FABRICATION

This chapter gives the details of fabrication steps of the processes used in this study. Section 4.1 gives an introduction to the MEMS fabrication techniques. Section 4.2 explains the SOIMUMPs process in detail, and gives the structural dimensions. Section 4.3 gives the details of nickel electroplating process, and explains the material layers that we use in this process. Section 4.4 explains the DRIE process. Finally, Section 4.5 gives a summary of this chapter.

4.1 Introduction to MEMS Fabrication Techniques

MEMS fabrication or micromachining refers to fabrication of devices with at least one of their dimensions in micrometer range with the help of etching techniques to remove part of the substrate or deposit thin film [60-61]. There are basically two micromachining techniques: bulk and surface micromachining.

In bulk micromachining, the wafer is etched deeply from either front or back side. However, the surface micromachining tries to build up structures onto the wafer with depositing techniques. Although the definitions of these micromachining techniques seem to be clear, it is not easy to say whether a process is surface or bulk

micromachining due to the fact that the process can use proper steps from both surface and bulk micromachining.

The bulk micromachining is usually realized using silicon substrate. There are various methods to etch silicon using wet or dry silicon etching techniques [62]. In the early times when the researchers used bulk micromachining to form MEMS sensors, they used wet etchants to etch silicon. The etchants may realize an isotropic etching where the silicon is etched with the same etch rate in each directions, or anisotropic etch, where the etch rates in different crystalline planes of silicon is significantly different. But, with wet etching, vertical comb fingers with high aspect ratio capacitances cannot be obtained. Moreover, wet etching, especially isotropic wet etching is not very controllable. In addition, the etchants may be dangerous for human health (EDP), or be problematic for the CMOS circuitry (KOH). However, the main advantageous of wet etching is to realize very thick proof mass structures easily. After the realization of the RIE machine (Reactive Ion Etching), the possibility of forming vertical comb structures is born, but the RIE machine could not handle high thicknesses. Finally, DRIE machine solved this problem creating very high trenches with high aspect ratio capacitances [63].

The surface micromachining uses thin film deposition techniques and then etches sacrificial layers to create suspended mechanical structures [26]. The process steps of surface micromachining are similar to CMOS circuitry fabrication, and hence the main advantage of surface micromachining is its compatibility with the standard IC process. In addition to this, the vertical comb fingers can be easily realized with this technique. However, the main disadvantage of the surface micromachining is the thin structural layer thicknesses and stress issues due to these thin films. But, with the advanced machines like DRIE, or using high aspect ratio high thickness photoresist for structural layer mold in electroplating process started to remove this disadvantage of the surface micromachining with providing high thickness proof masses [64].

There are various accelerometers and gyroscopes fabricated with bulk [65-68] or surface micromachining [69-73]. Moreover, some sophisticated processes are developed using both surface and bulk micromachining for realization of MEMS sensors [74-75].

4.2 Details of SOIMUMPs Process

SOIMUMPs process is a commercial MUMPs (Multi-User MEMS Processes) provided by CRONOS Inc. Figure 4.1 shows the overview of the SOIMUMPs process. The process uses an SOI (Silicon on Insulator) wafer and patterns the top silicon layer for the structural layer. The process starts with the phosphorus doping of top silicon layer. This doping is to arrange the resistivity values of the silicon layer. After this step, Cr/Au metal layer is patterned. For this layer, first a negative photoresist is coated, exposed, and developed according to metal mask, and then Cr/Au is e-beam evaporated. A successful lift-off step patterns the metal layer. After first metallization, structural layer is patterned. To achieve this, masking photoresist is coated, exposed and developed according to structural mask. After lithography, the structural silicon is etched with DRIE up to the oxide layer. After this point, the front part of the wafer is coated with a protective layer and a masking photoresist layer is patterned on to the backside of the layer. The bulk silicon part of the wafer is etched all the way with DRIE up to the oxide layer. This etching defines the suspended regions of the sensors. After this step the oxide layer and the protective layer is etched. From this point on, the substrate connection can be achieved and the structures are suspended. A shadow mask technique is used to pattern second metallization which provides substrate connection. The process ends after the shadow mask is removed.

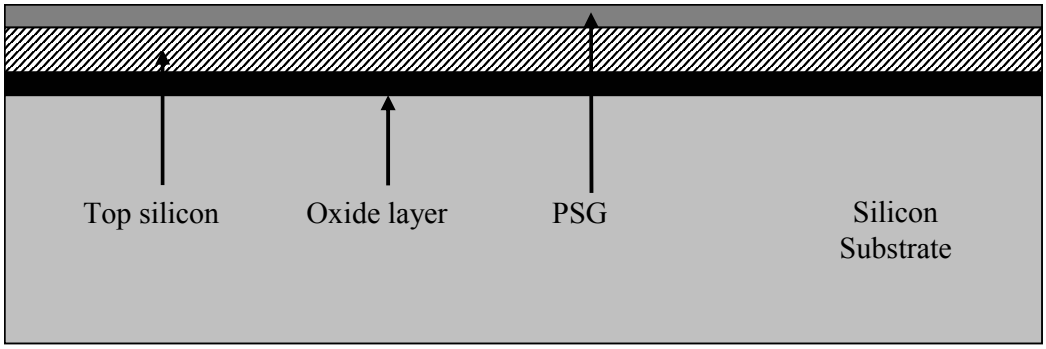

a) The wafer is coated with PSG (phosphosilicate glass) and annealed to dope the top silicon layer with phosphorus. PSG is removed afterwards.

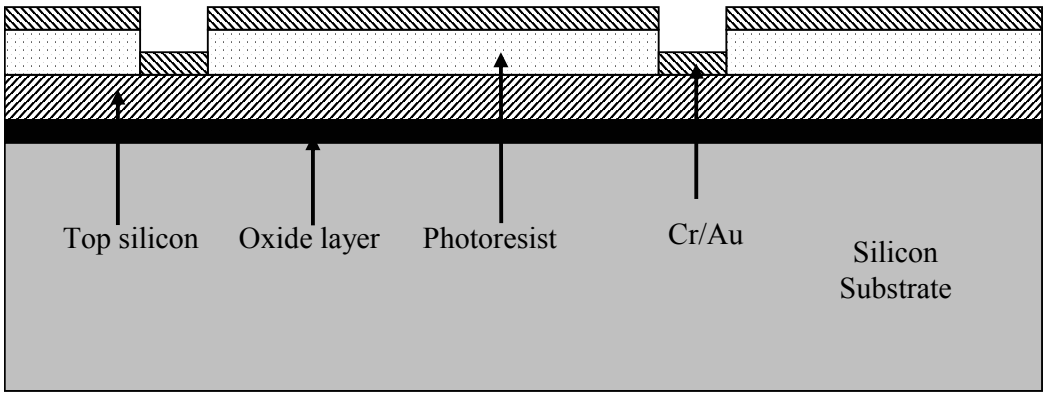

b) A negative photoresist is patterned by exposure and then Cr/Au metallization layer is deposited using e-beam deposition.

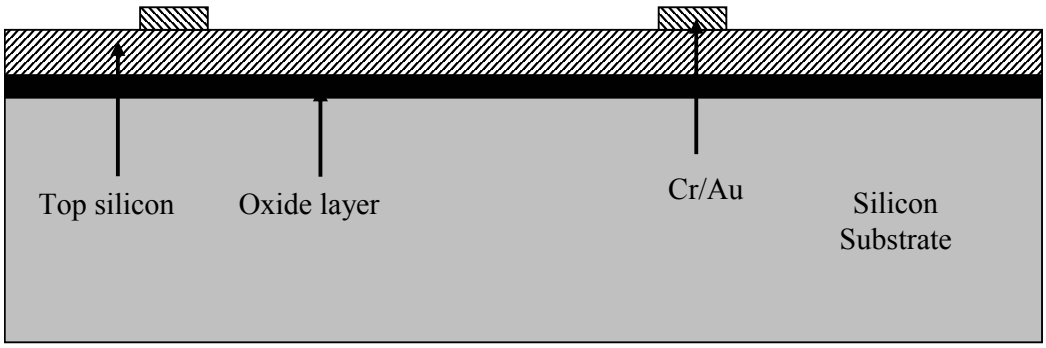

c) The photoresist is lifted-off and the metal layer on top is also removed this way. The remaining metal parts define the first metallization layer.

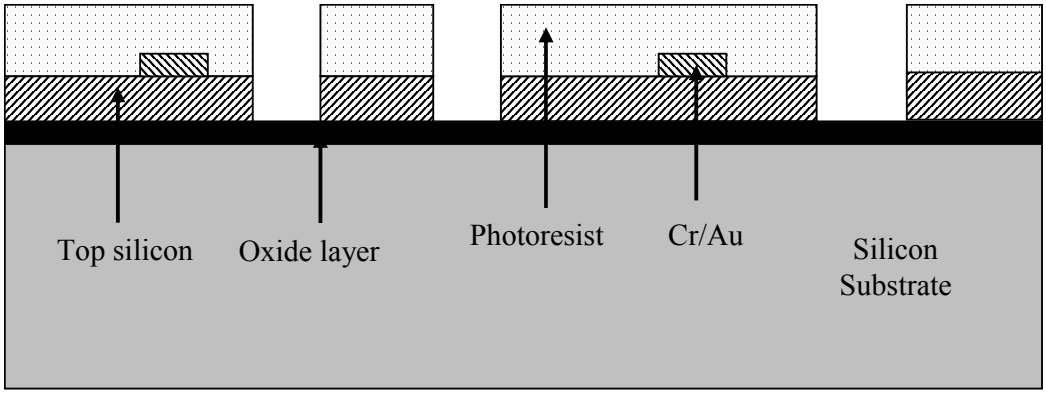

d) A masking photoresist is coated on to the front side and patterned with exposure. Using this photoresist mask the top silicon layer is etched with DRIE up to oxide layer. Photoresist is removed afterwards.

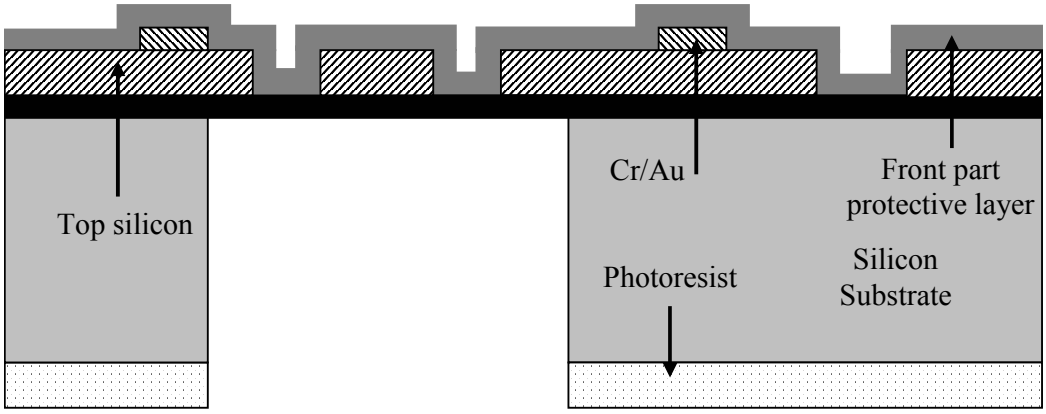

e) A masking photoresist is coated on to the back side and patterned with exposure and front layer is coated with a protective layer. Using this photoresist mask the bulk silicon layer is etched with DRIE up to oxide layer. Photoresist is removed afterwards.

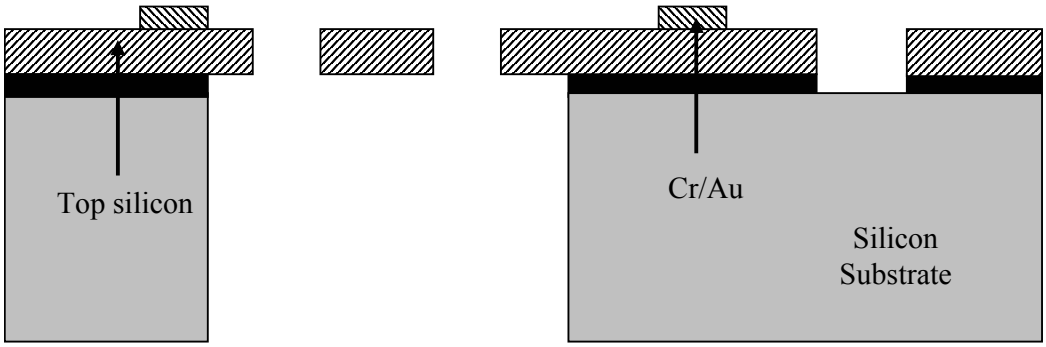

f) The protective layer is removed. After that the oxide layer is removed making the structures suspended.

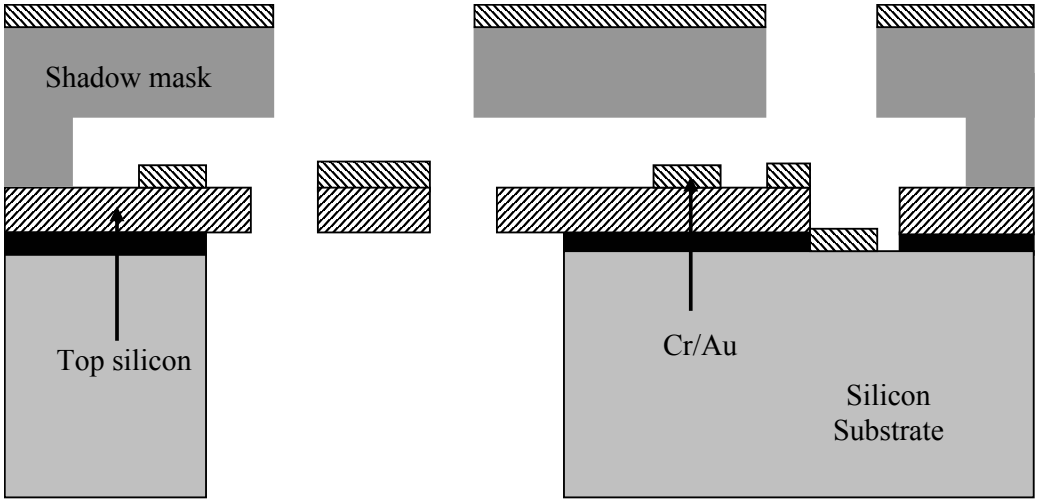

g) Silicon made shadow mask is bonded to the SOI wafer for the masking layer of final metallization. The metal is evaporated and through the holes and stick to the SOI wafer. This metallization is important for substrate contact.

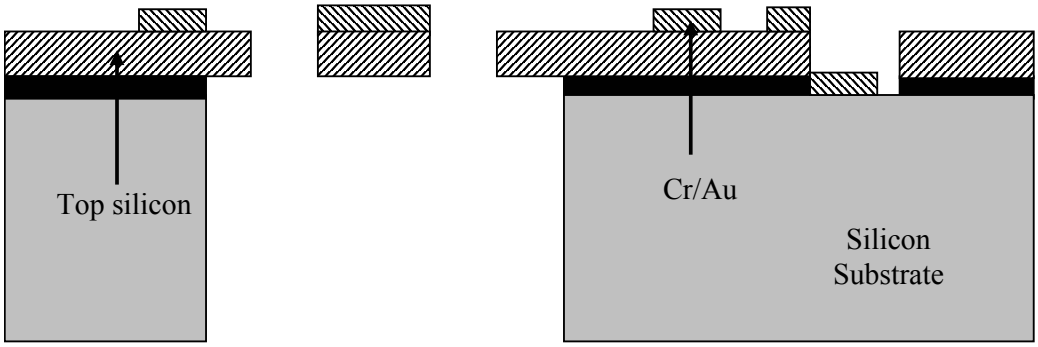

h) The final view of SOIMUMPs samples.

Figure 4.1: The overview of SOIMUMPs process [58].

Figure 4.2 shows the total layout of the overall SOIMUMPs chip. The chip includes accelerometers and gyroscopes for this study and also some test structures and a gyroscope for another MEMS related study. The total chip occupies 10mm x 10mm total die area.

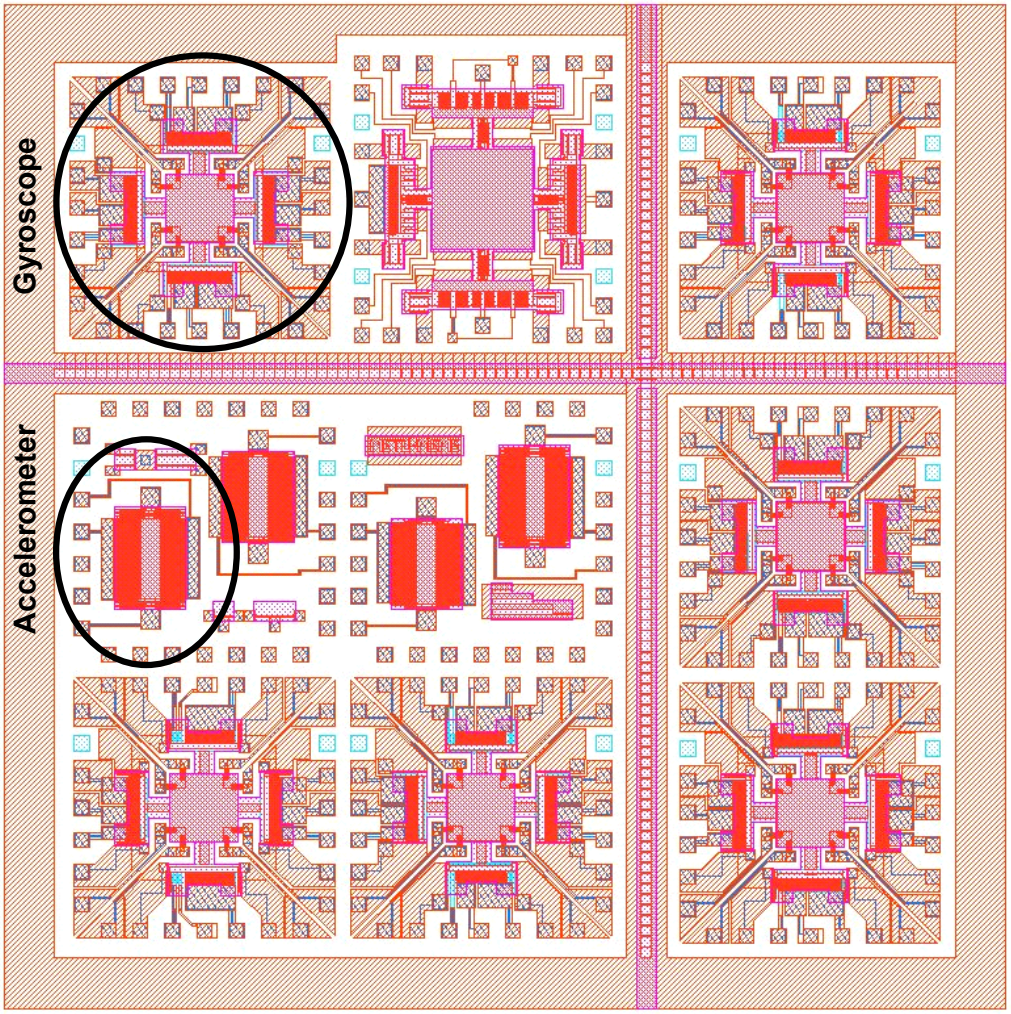

Figure 4.2: The overall layout of SOIMUMPs chip. The chip includes accelerometers and gyroscopes for this study and also some test structures and a gyroscope for another study. The chip occupies 10mm x 10mm total chip area.

Table 4-1 gives the thicknesses and purposes of material layers in SOIMUMPs process. The main advantage of this process is using single crystal silicon as its structural layer. Single crystal silicon shows great mechanical and electrical properties and is highly preferred is MEMS devices [26]. Moreover, DRIE patterning on the front size provide 5 aspect ratio capacitive walls for vertical comb structures. Combining this moderately high aspect ratio with 10 µm structural height, reasonably high capacitances can be achieved with this process. Due to these

advantages, we have chosen SOIMUMPs process as one of the fabrication processes for realizing our sensors.

Table 4-1: Thicknesses and purposes of material layers in SOIMUMPs process [58].

Material Layer	Thickness (μm)	Purpose
Metal 1 (Cr/Au)	0.52	Provides electrical connections.
Top silicon	10	Structural silicon layer.
Oxide	1.0	Substrate isolation.
Silicon substrate	400	Substrate.
Metal 2 (Cr/Au)	0.65	Provides substrate connection.

4.3 Details of Nickel Electroplating Process

The nickel electroplating process used in this study is a surface micromachining process which is developed in the facilities of METU-MET. The fabrication steps of this process are leaded by Said Emre Alper, and realizing these steps is also a part of this study. Figure 4.3 shows the overall fabrication details of nickel electroplating process. The process uses glass as the substrate layer and nickel as the structural layer. The structural nickel is formed using electroplating with the help of thick photoresist mold.

Table 4-2 gives the thicknesses and purposes of material layers in nickel electroplating process. The use of a glass substrate is one of the major advantages of this process due to the fact that glass being an insulator will not cause parasitic capacitances in the pad regions and will not cause levitation effect [76]. In addition to this advantage, the electroplating process provides a high possibility of material choices due to the fact that photoresist mold provides the possibility of electroplating various metals for various purposes. In this process, nickel is selected for the structural material for its attractive material properties such as Young's modulus and yield strength [11, 77]. Moreover, gold is suitable for interconnect material due to its high conductivity and ease of fabrication [78].

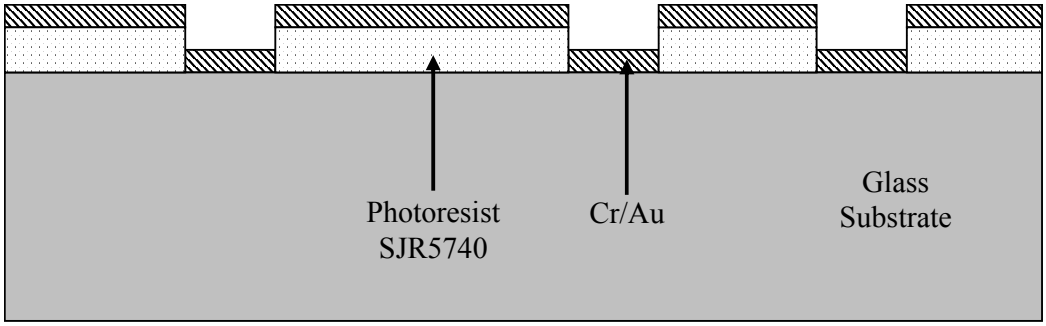

a) SJR5740 is patterned onto the glass wafer using exposure and then Cr/Au is evaporated.

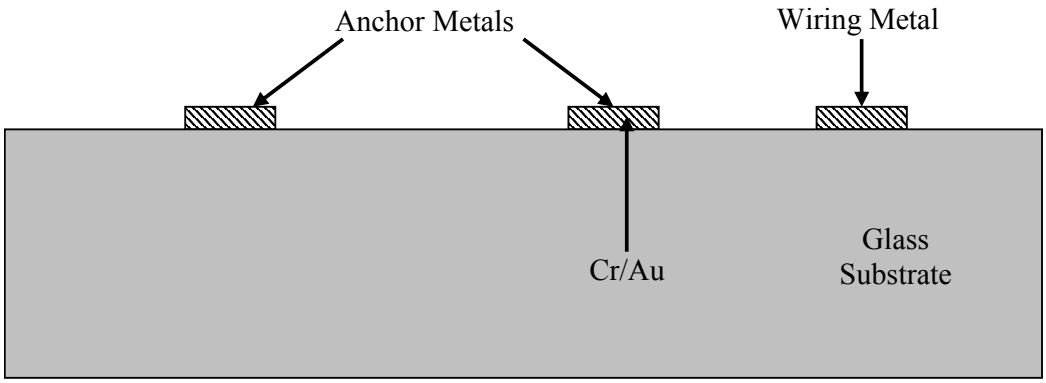

b) SJR5740 is lifted-off and metallization layer is formed.

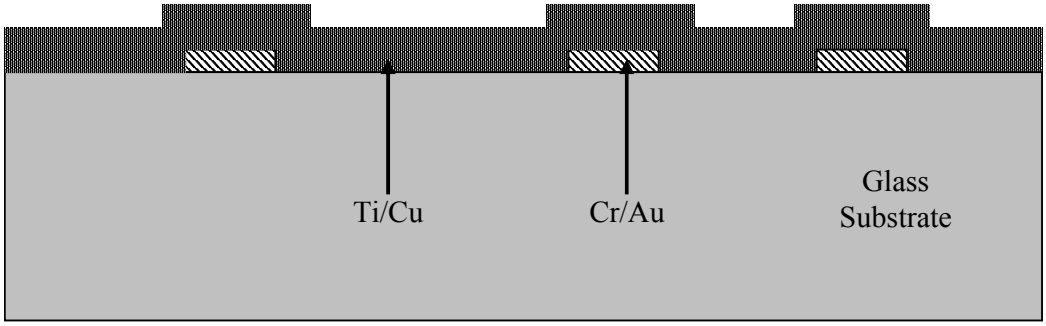

c) Ti/Cu is sputtered onto the wafer. This layer is the seed layer for the sacrificial cupper electroplating.

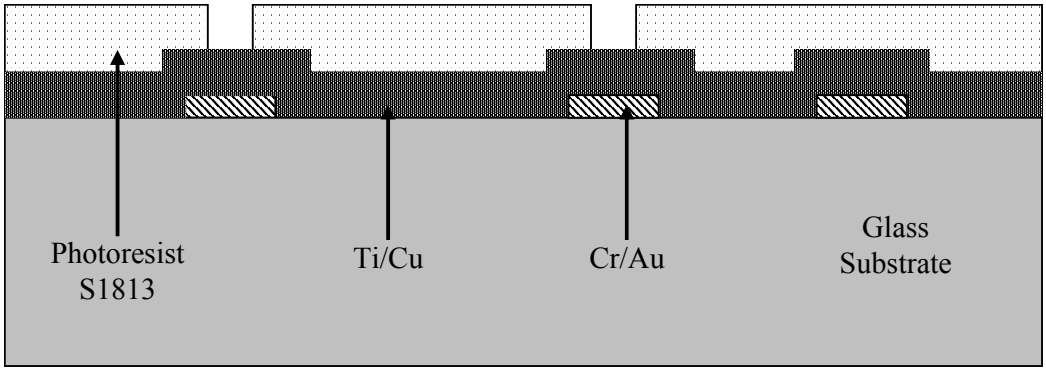

d) S1813 is patterned with exposure. This photoresist is used for the masking layer of anchor region Ti/Cu etches.

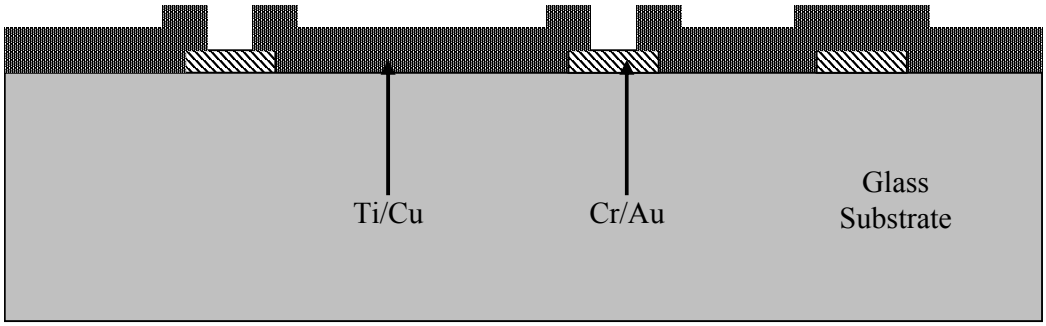

e) Ti/Cu in the anchor regions is etched.

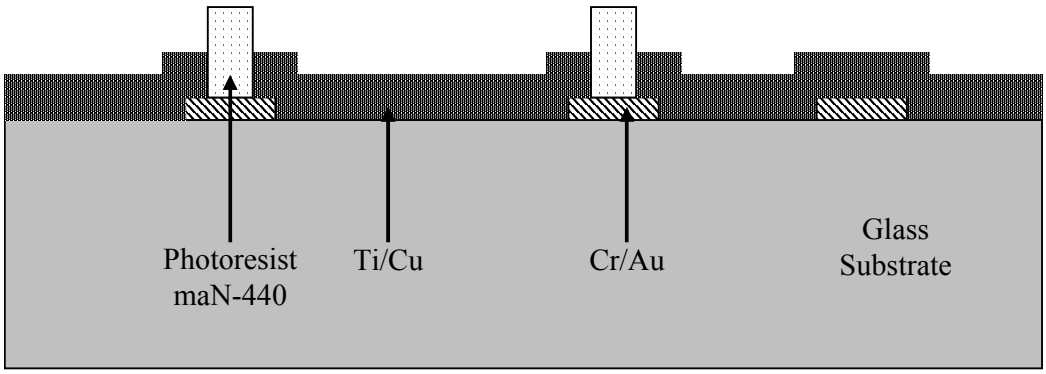

f) maN-440 is patterned with exposure. This photoresist prevents sacrificial Cu electroplating in the anchor regions.

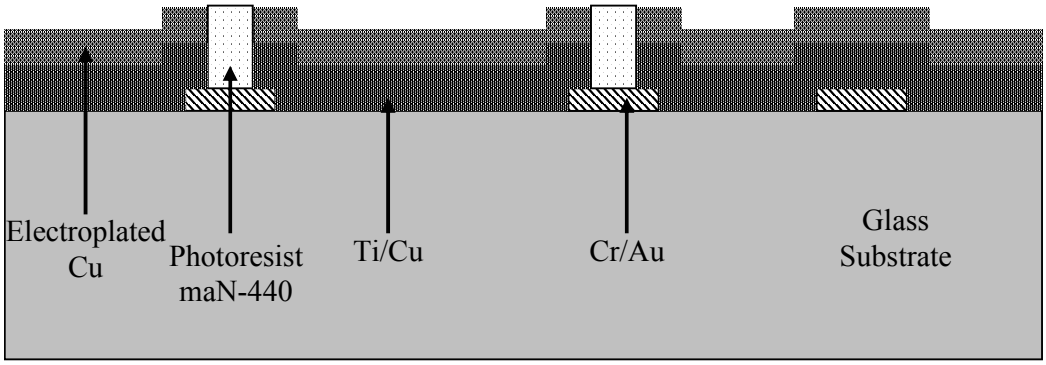

g) The sacrificial Cu is electroplated. maN-440 is stripped afterwards.

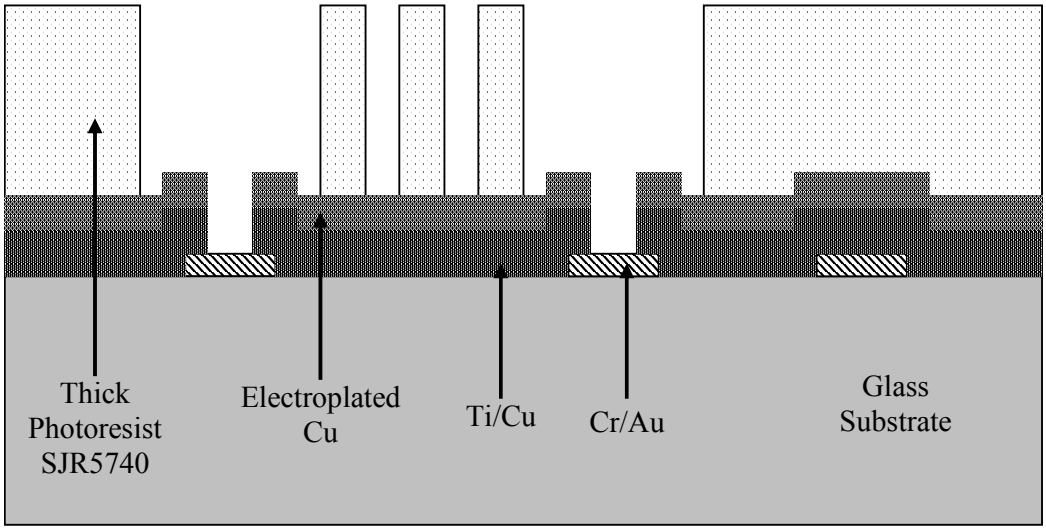

h) Structural mold resist SJR5740 is patterned with exposure.

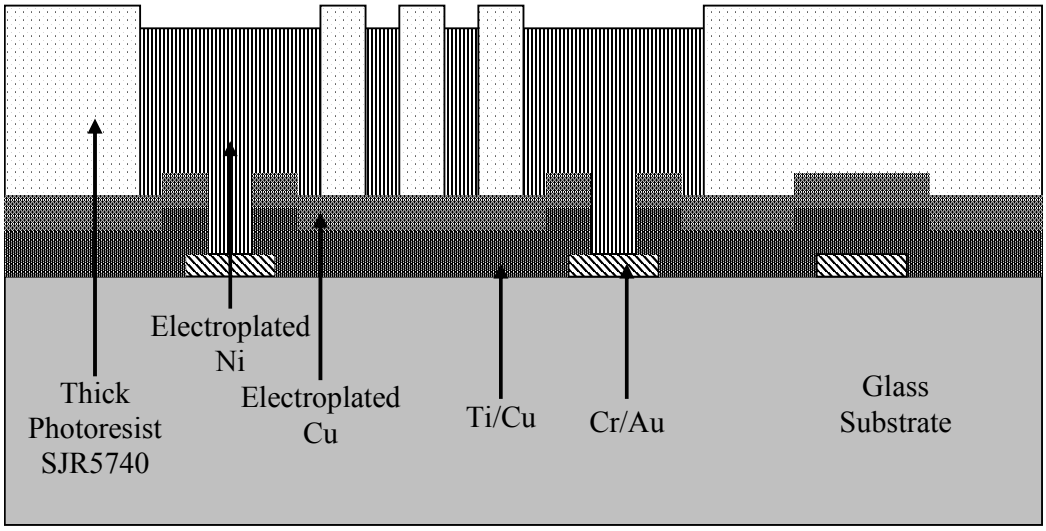

i) Structural nickel is electroplated.

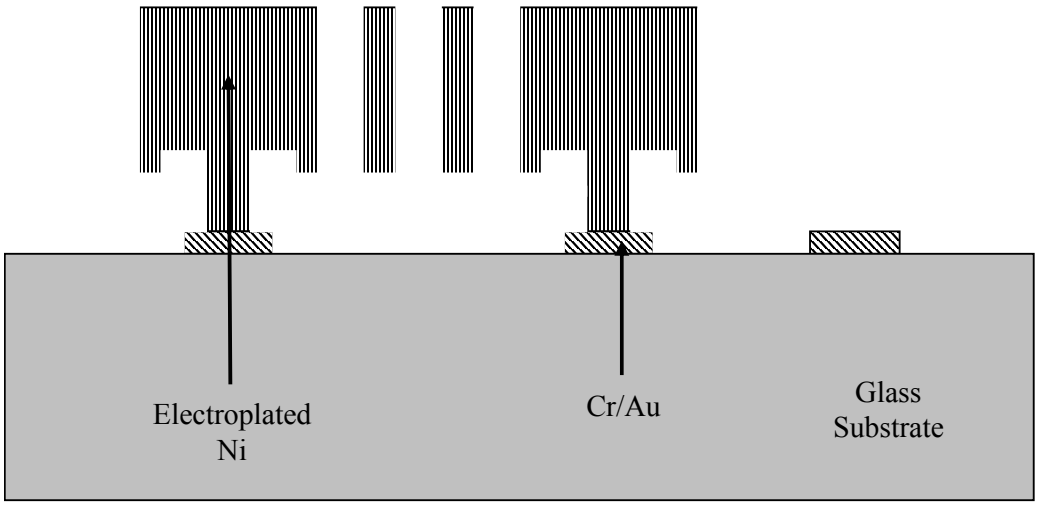

j) First the structural mold photoresist is stripped and then the sacrificial Cu is etched. The process finishes with etching Ti layer.

Figure 4.3: Overall fabrication details of nickel electroplating process.

Table 4-2: Thicknesses and purposes of material layers in nickel electroplating process.

Material Layer	**Thickness (µm)**	**Purpose**
Glass substrate	500	Substrate
Metal (Cr/Au)	0.17	Provides electrical connections
Sacrificial cupper	5	Provides suspended regions
Structural nickel	17-20	Structural material

Due to these advantages, the nickel electroplating process is chosen as one of the fabrication process for realizing the sensors developed in this study. Sections 4.3.1-4.3.3 will explain the fabrication steps of this process in detail.

Figure 4.4 shows the overall layout of the nickel electroplating wafer. The wafer is a 4 inch wafer and consists of not only accelerometers and gyroscopes designed within this study, but also some other gyroscope designs and some test structures for another study in our group.

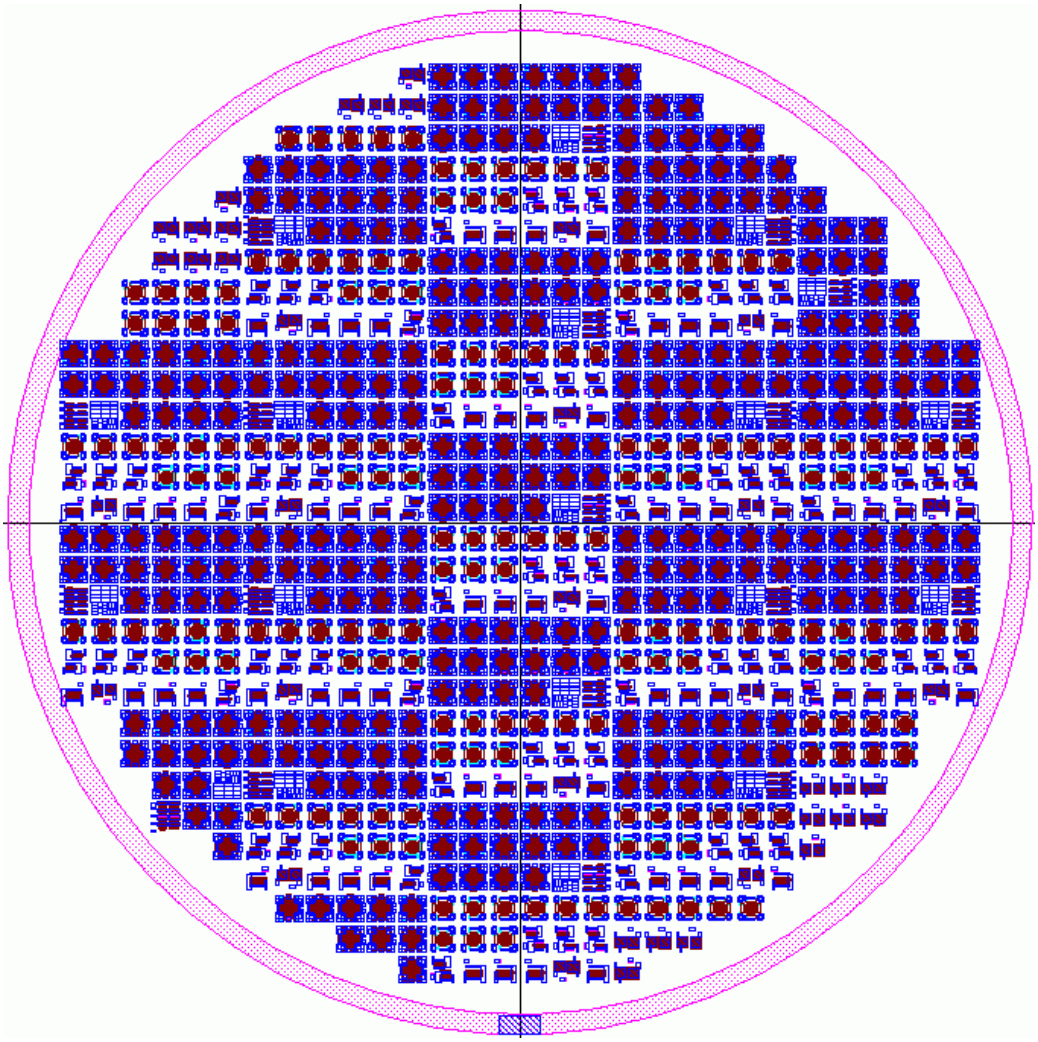

Figure 4.4: The overall layout of the nickel electroplating wafer. The chip is a 4 inch wafer including several accelerometers and gyroscopes for this study and also gyroscopes for another study. The sensors are placed into 3mm x 3mm die areas. After the process, these dies are separated using a dicer machine.

4.3.1 Fabrication of Metallization Layer in Nickel Electroplating Process

The metallization layer in the nickel electroplating process is used for both electrical connections and for the adhesion layer of nickel structural layer to the glass substrate. For this purpose, the chromium/gold layer is patterned with lift-off. Gold is the main layer for electrical connections and the adhesion of nickel to glass. However, gold

needs an adhesion layer between itself and glass substrate and hence chromium is used for this purpose.

The metallization process is the first process step and realized with lift-off. The process starts with the preparation of the glass wafer. The wafer is first put into piranha etchant (1:1 H_2SO_4:H_2O_2) for 15 min for organic cleaning. After this step, the wafer is dipped into BHF (Buffered HF, 6:1 NH_4:HF) for 30 sec. This step is important for the adhesion of chromium to the glass substrate. BHF slowly etches the glass and creates a rough surface. This rough surface increases the adhesion of chromium to the glass surface.

After the preparation of the glass wafer, the wafer is coated with 7-8 μm SJR5740 photoresist. This photoresist is patterned with exposure. After development, the anchor regions and the routing metal regions will be developed, while in all the remaining regions the photoresist will remain. The wafer is then put into evaporation machine and first chromium (200 Å) then gold (1500 Å) is evaporated (Figure 4.3 (a)).

Evaporation does not have good step coverage; however this property of evaporation turns out to be advantageous in lift-off process. The wafer is put into a petry dish full of acetone and with the help of ultrasonic buzzer the photoresist and the metal layer on top of photoresist is lifted-off (Figure 4.3 (b)). After this step the metallization layer is formed. This layer provides electrical connections and also is used as an adhesion layer of nickel to glass substrate.

4.3.2 Fabrication of Sacrificial Layer in Nickel Electroplating Process

The sacrificial layer in the electroplating process provides suspended regions of the sensor. For selecting the sacrificial layer, a thick sacrificial layer is preferred to achieve lower air damping. Moreover, a more important issue is the etchant that etches the sacrificial layer. The etchant should not deform other materials while

etching the sacrificial layer. According to these criteria, cupper is selected as the sacrificial layer.

The sacrificial layer covers the entire wafer except the anchor regions. To achieve this, the cupper is electroplated while the anchor regions are filled with a proper photoresist. Hence, the sacrificial formation process starts with the formation of seed layer for cupper electroplating. The wafer is put into the sputtering machine for titanium/cupper (300 Å / 3000 Å) seed layer sputtering. The main seed layer is cupper, but to achieve a good adhesion between glass substrate and cupper, titanium layer is used. After sputtering (Figure 4.3 (c)), to etch the titanium/cupper in the anchor regions, S1813 thin photoresist is patterned with exposure (Figure 4.3 (d)). With S1813 masking layer, the sputtered metal layers in the anchor regions are removed by first cupper etch (1:1:18 CH_3HOOH:H_2O_2:DI H_2O) and then titanium etch (1:1:600 HF:H_2O_2:DI H_2O) (Figure 4.3 (e)). After these etchings, the masking photoresist is removed.

After preparation of the seed layer, the wafer is coated with maN-440 negative photoresist and patterned with exposure. This time the photoresist in the anchor regions remained in the other regions the photoresist is developed (Figure 4.3 (f)). This remaining photoresist prevents sacrificial cupper electroplating in the anchor regions. After the development, 5 μm thick sacrificial cupper of is electroplated (Figure 4.3 (g)). The fabrication of sacrificial layer finishes with the removing of the photoresist.

4.3.3 Fabrication of Structural Layer in Nickel Electroplating Process

The fabrication of the structural layer in the electroplating process is achieved by first patterning the mold photoresist, then electroplating the structural nickel, and finally stripping the stripping the mold photoresist and the sacrificial layer.

The structural mold formation is one of the most critical steps of the whole process. This step defines the aspect ratio of the sensor, as it defines the structural part and

spacing part in the comb finger regions. To achieve a high aspect ratio, and high proof mass thicknesses, the photoresist mold should be thick and can be patterned with high aspect ratio. SJR5740 is a thick photoresist that can realize these conditions [79]. In the literature, there are some studies that achieved 6.8 aspect ratio structures [80].

For the formation of the mold, first SJR5740 is coated with a low spin rate. After this step, the wafer should wait on the chuck of the spinner for a while until the stress related lines on the photoresist surface vanishes. After this waiting period, the wafer is softbaked on the hotplate. After softbake, there is relaxation time period for this photoresist in high humidity levels. To achieve this level, we put few water drops in a wafer holder, put the wafers in this holder, close the holder, and wait for 2 hours. After this relaxation time, exposure is done. There is another relaxation period after the exposure again in the high humidity levels for 2 hours. After this relaxation period, the development can be done (Figure 4.3 (h)).

After the formation of the mold photoresist, the mold should be hardbaked. This bake is prevents deformation of the mold photoresist in the nickel electroplating solution. However, SJR5740 is sensitive to high temperatures and if applied to high temperatures, it deforms its shape. To avoid any shape change due to hardbake, the wafer is applied to 80 °C for 16 hours. With this hardbake, the photoresist shape changes a little in the bulky photoresist regions, but it withstands the electroplating solution.

The next step is the nickel electroplating step. We have made several electroplating trials with dummy wafers to achieve the optimum nickel electroplating conditions. The applied current, the agents in the solution are important effects in the nickel electroplating process, and playing with these conditions we have achieved very shiny and low stress nickel structures (Figure 4.3 (i)).

The process finishes with removing all the sacrificial layers. However, due to the fact that dicing of the wafer may cause damage to the suspended structures, the

release operation is done after dicing. However, we have observed that, the cupper sacrificial layer is deformed in the dicing operation, and deformed cupper also deforms the metal pads underneath. To avoid this problem, before the dicing operation, the cupper in the pad regions should be etched away, but the samples should not be totally released not to cause any damage in the dicing operation. Hence, first mold photoresist is stripped, and then sacrificial cupper is etched half way. Due to the fact that the cupper in the open regions are gone first, with a proper timing, we have achieved to remove the cupper in the pad regions while keep the cupper under the devices. After the half cupper etch, the wafer is coated with a protective photoresist and then diced. After dicing, the release operation is done sample by sample. First, the protective photoresist is removed, then the remaining cupper is etched away, then the titanium layer under the cupper layer is etched. After titanium etch, the samples are totally released. Not to cause any stiction problem, the last step is to dip the samples into IPA, and evaporate the IPA on the hot plate. Figure 4.3 (i) shows the final view of the electroplated samples.

4.4 Details of DRIE Process

The DRIE process is an advanced process that uses bulk micromachining. The DRIE process is currently being developed in the facilities of METU-MET. The fabrication steps of this process are leaded by Said Emre Alper, and realizing these steps is also a part of this study. Figure 4.5 shows the overall fabrication details of the DRIE process. This process uses glass substrate similar to nickel electroplating process. The silicon wafer that will be used as the structural layer is bonded onto the glass wafer with anodic bonding and then silicon is etched from the top with DRIE machine. Most of the process steps in the DRIE process have been completed. The DRIE tool that is necessary for the deep trench etching in silicon is also purchased, and the installation of it is still continuing.

a) Cr/Au is evaporated.

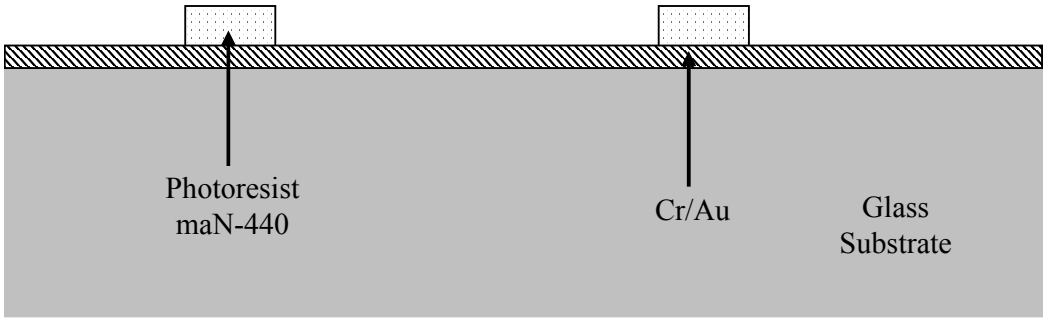

b) Negative resist is patterned with exposure. This photoresist defines the metal mask for the glass etch.

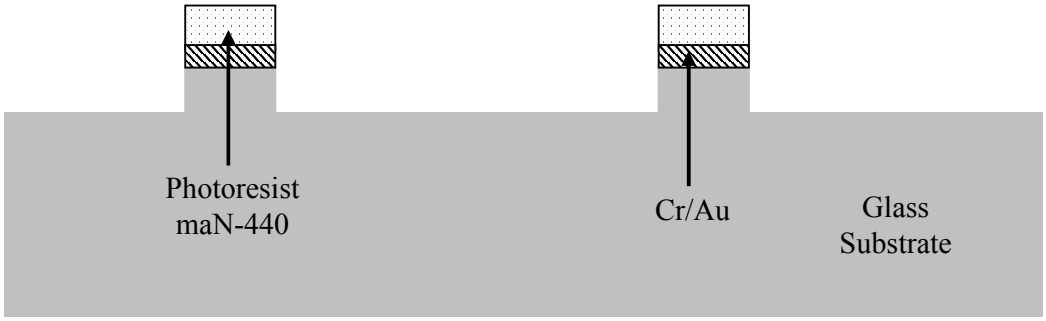

c) First Cr/Au is etched and glass etch mask is formed. After that, glass is etched.

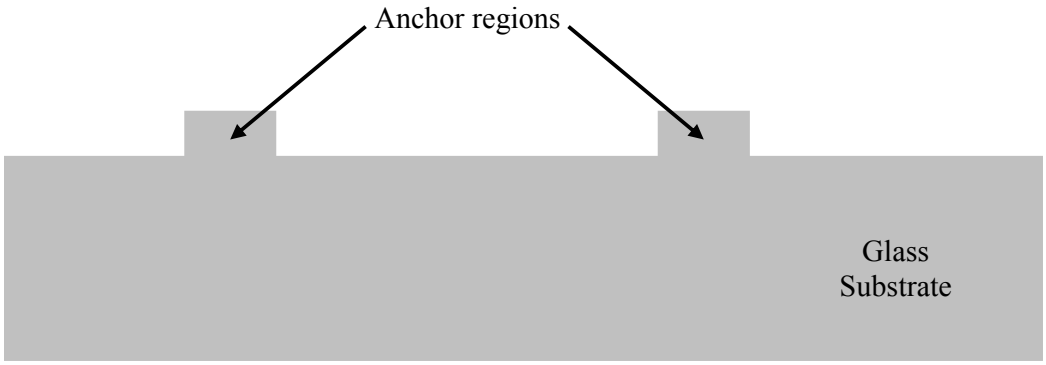

d) Photoresist and metal mask is stripped. The anchor regions are now available for anodic wafer bonding.

e) S1828 is patterned with exposure. This photoresist defines the regions for metal shield layer.

f) Using S1828 as the masking layer, a shallow glass etch is done. This etching will not prevent shield layer connection to the silicon wafer but it will make increase the bonding region by decreasing the level difference between the glass and silicon wafers.

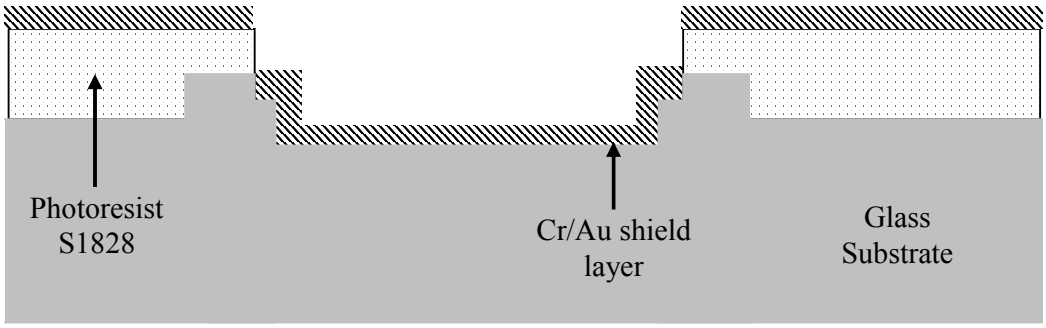

g) Cr/Au metal shield layer is evaporated.

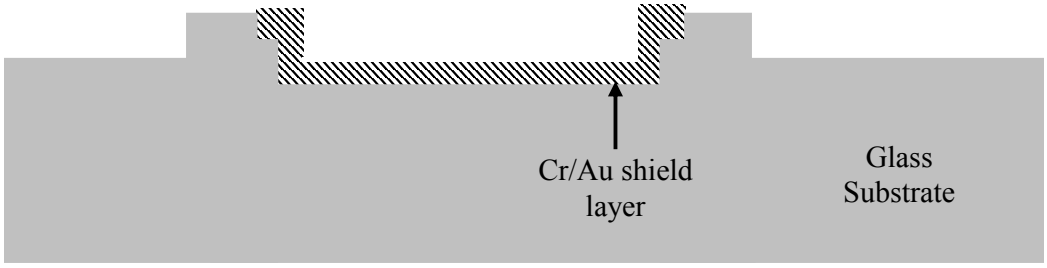

h) Cr/Au metal shield layer is patterned with lift-off. This layer minimizes the notching effect in DRIE step [82].

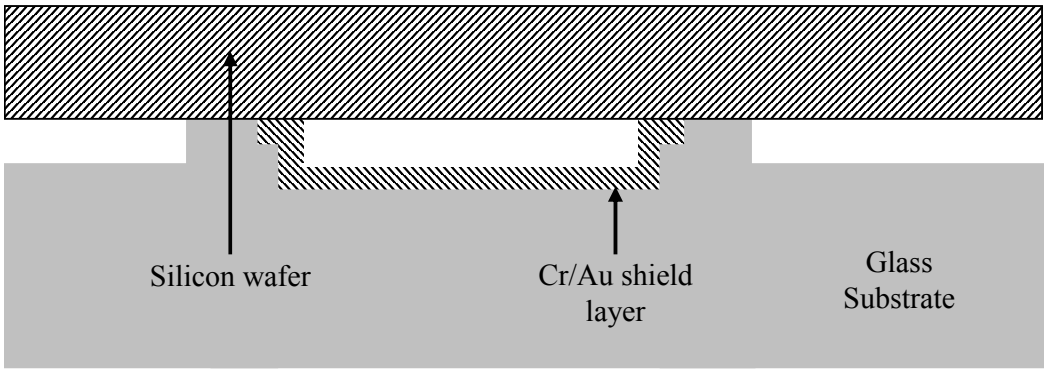

i) Silicon wafer is anodic bonded to the glass substrate.

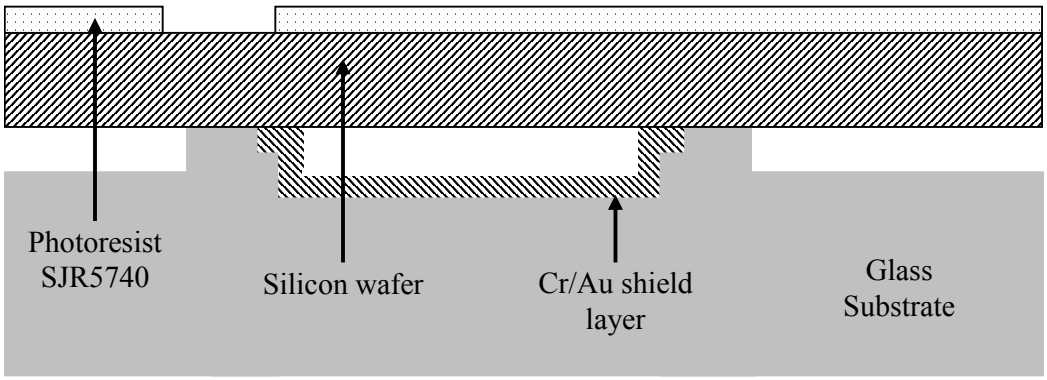

j) SJR5740 is patterned with exposure. This photoresist defines the metallization regions.

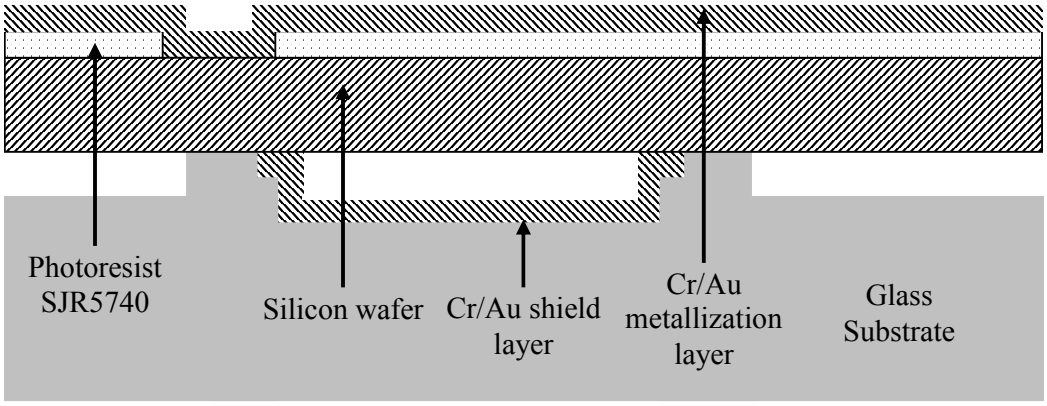

k) Cr/Au metallization layer is evaporated.

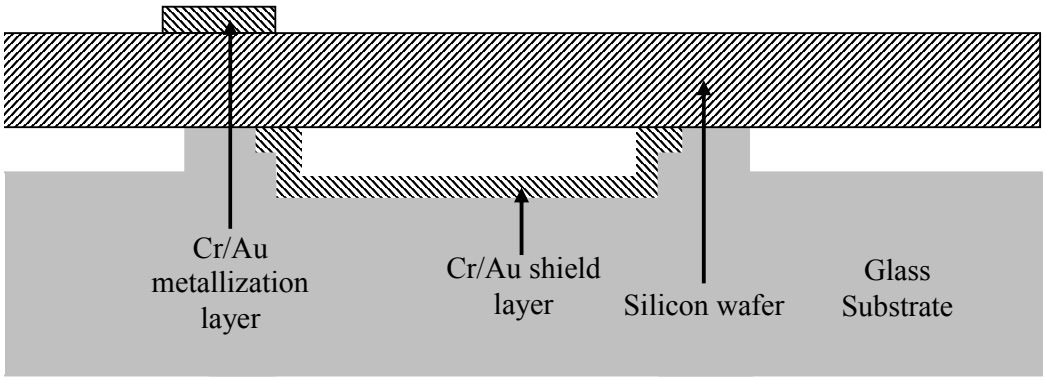

l) Cr/Au metallization layer patterned with lift-off.

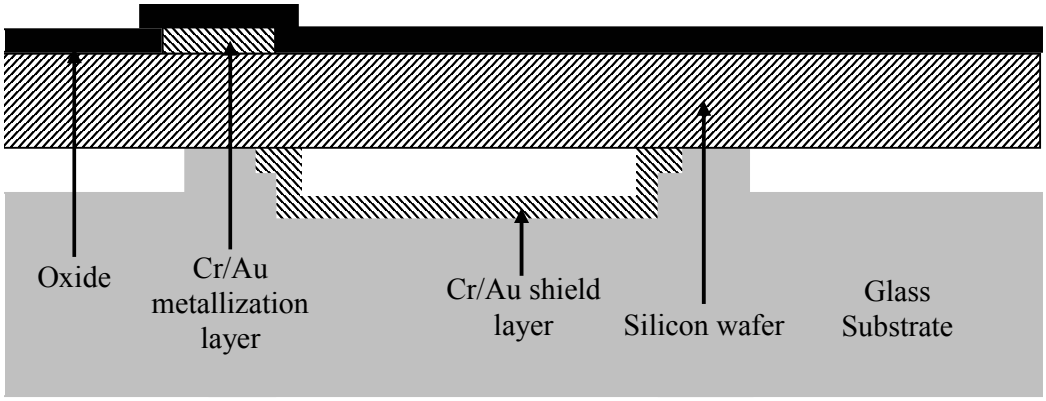

m) Oxide is coated with PECVD. This layer is the masking layer for the DRIE step.

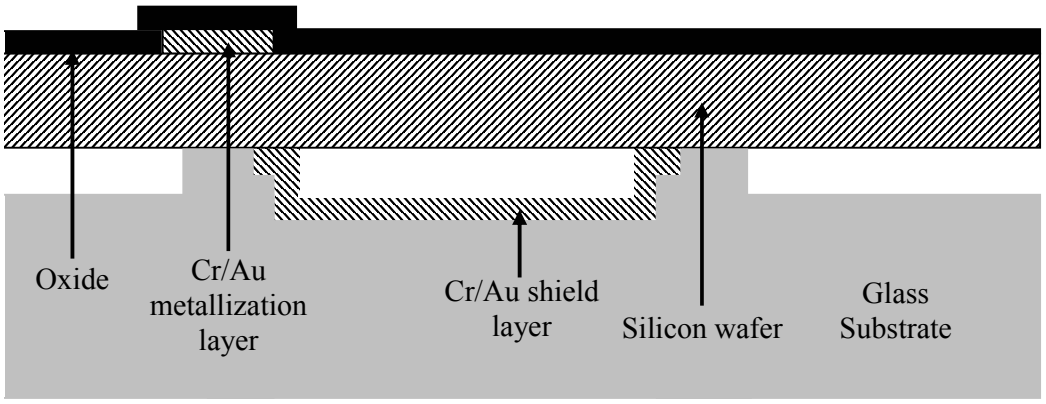

n) S1813 is patterned with exposure. This photoresist defines the oxide mask regions for DRIE step.

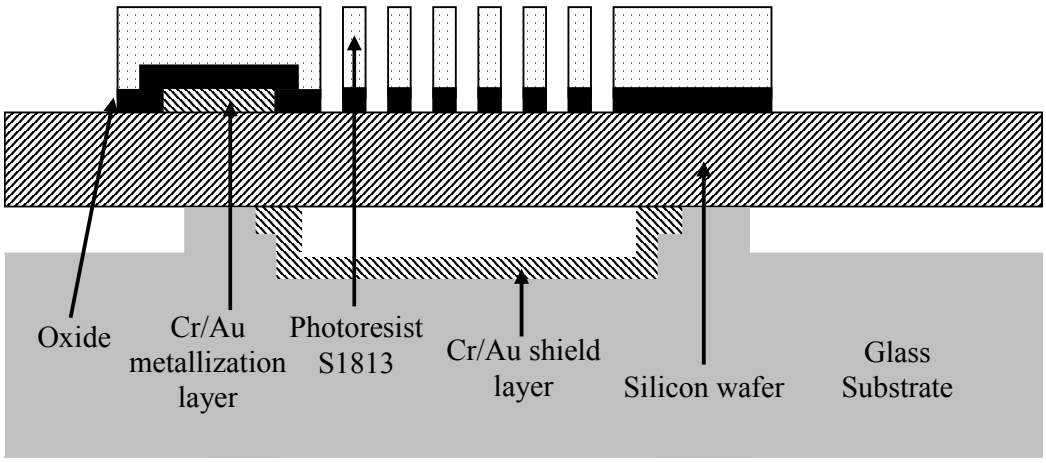

o) The oxide is etched with RIE.

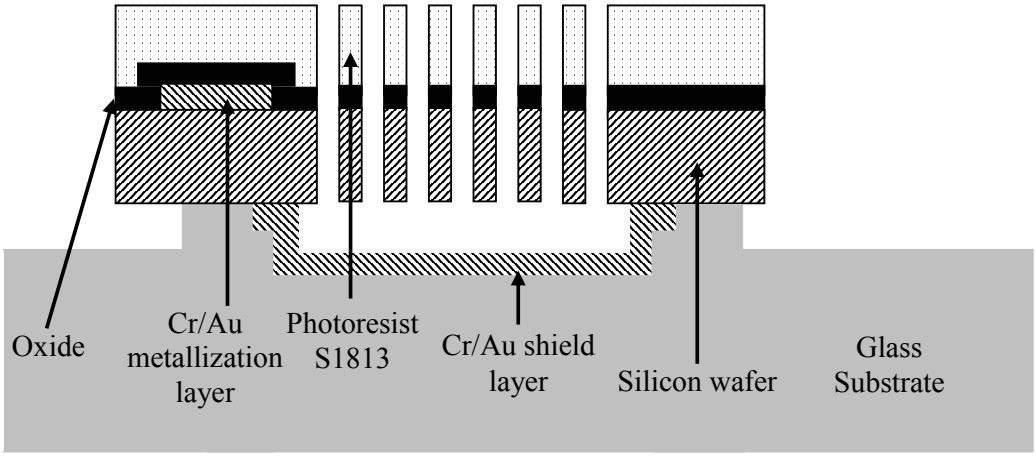

p) Silicon is etched with DRIE.

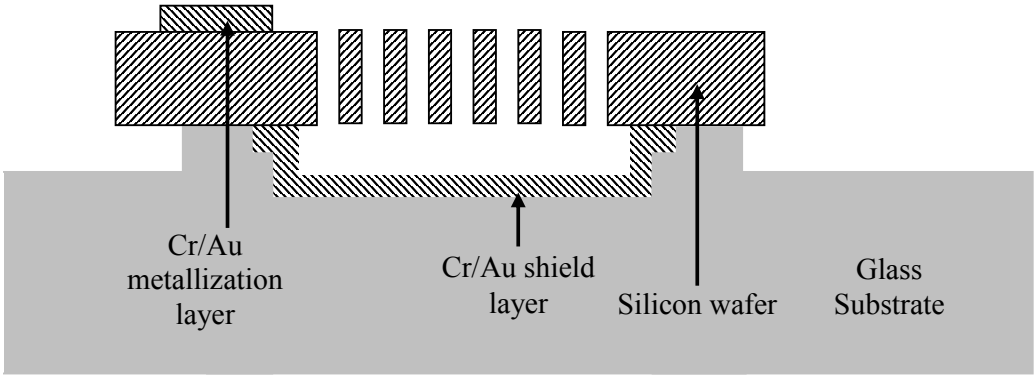

r) The process finishes after the masking photoresist and the oxide is stripped.

Figure 4.5: Overall fabrication details of the DRIE process.

DRIE process has several advantages compared to other processes [81]. The most important advantage of this process is realizing very high aspect ratio vertical capacitances. High aspect ratio capacitances is the key element for realizing high performance capacitive sensors, hence DRIE provides the realization of very high performance MEMS sensors. In addition to that, this process provides single crystal silicon structural layer which is highly preferred in MEMS devices due to its mechanical and electrical properties [26]. Moreover, the wafer can be bonded to an

insulator substrate such as glass, and hence unwanted levitation effect can be avoided [76].

Table 4-3 the thicknesses and purposes of the material layers used in DRIE process, and Figure 4.6 shows the overall DRIE wafer. Similar to nickel electroplating process, this wafer consists of accelerometers and gyroscopes designed within this study and also some gyroscopes designed for another study going on in our group.

Table 4-3: Thicknesses and purposes of material layers in DRIE process.

Material Layer	**Thickness (μm)**	**Purpose**
Glass Substrate	500	Substrate
Mask metal (Cr/Au)	0.12	Masking layer for glass etch
Glass anchor	5	Provides suspended regions
Shield metal (Cr/Au)	0.12	Minimizes notching effect in DRIE step [82].
Structural silicon	100 or 200	Structural material
Silicon Oxide	1-2	Masking layer for DRIE
Metal (Cr/Au)	0.12	Provides electrical connections

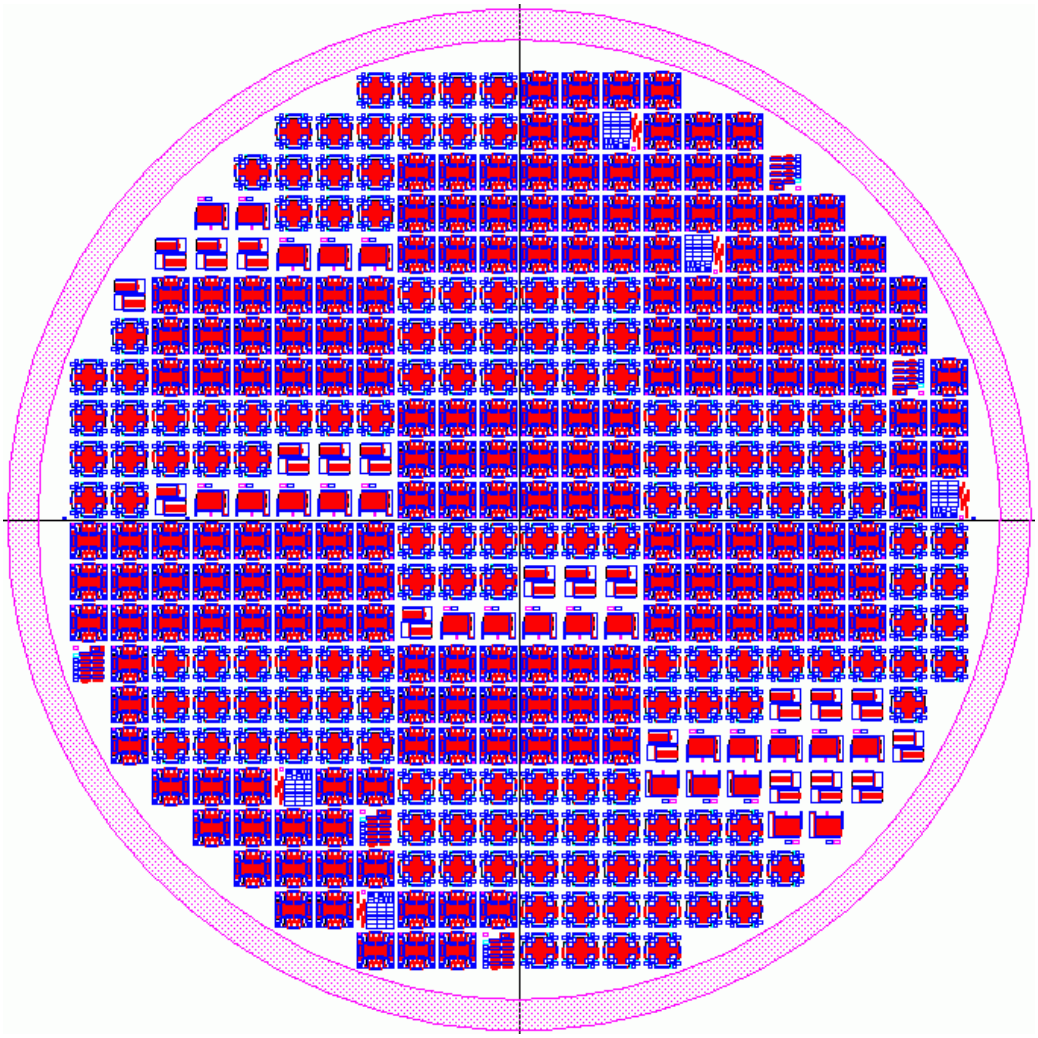

Figure 4.6: The overall layout of the DRIE wafer. This is a 4-inch wafer including several accelerometers and gyroscopes for this study and also gyroscopes for another study. The sensors are placed into 4mm x 4mm die areas.

4.4.1 Fabrication of Anchor Regions and Shield Metal in the DRIE Process

Anchor regions are the support points that connect the suspended regions to the substrate. Unlike the nickel electroplating process, in DRIE process the material of the anchor regions is not the same material with the structural material. In DRIE process, the anchor material is the same material with the substrate material. To process this structure, the glass substrate is etched from the top side with anchor regions protected.

The anchor region formation is the first process step and hence the process starts with the preparation of the glass wafer. Similarly with the nickel electroplating process, the wafer is first put into piranha etchant (1:1 H_2SO_4:H_2O_2) for 15 min for organic cleaning. After this step, the wafer is dipped into BHF (Buffered HF, 6:1 NH_4:HF) for 30 sec to increase the adhesion of chromium to the glass substrate. The masking layer for the glass etch is the evaporated chromium/gold, hence BHF step is critical. After chromium/gold evaporation (200 Å / 1000 Å) (Figure 4.5 (a)) maN-440 negative resist is patterned with exposure. This patterned photoresist defines the masking region of the metal mask underneath (Figure 4.5 (b)).

The wafer is dip into gold etchant and then chromium etchant. After these etching steps the masking metal layer is formed. Then without stripping the photoresist, using both photoresist and the metal as the masking layer the glass etch process is done (Figure 4.5 (c)). The glass etchant (10:7:3 DI H_2O:HF:HNO_3) creates a very large undercut, decreasing the actual anchor region, but we have considered this undercut in the design period. After glass etch, the photoresist, the masking gold, and the masking chromium is stripped (Figure 4.5 (d)).

The next step is the formation of shield metal. The shield metal minimizes the undesired notching effect in DRIE process [82]. The shield metal should be electrically connected to the structures and during the DRIE step, the ions that etches though the silicon will not etch under the silicon afterwards but will bombard the shield metal layer [82]. Hence, the shield metal should touch the structural silicon in the anchor points. This can be realized with a thin metal layer placed onto the anchor points. During the anodic bonding, the silicon can touch the shield layer in these regions. However, this thin layer will decrease the bonding region, and also will create a level difference that will further decrease the bonding area. Hence, in the process flow, we first create a shallow etch region for the shield layer to decrease the level difference. First, S1828 is patterned with exposure (Figure 4.5 (e)). This photoresist is the masking layer for shallow glass etch and also enables shield metal patterning with lift-off. After patterning the photoresist, the wafer is dipped into BHF (Buffered HF, 6:1 NH_4:HF) for the shallow glass etch (Figure 4.5 (f)). Then

chromium/gold (200 Å / 1000 Å) is evaporated (Figure 4.5 (g)). After lift-off, shield metal patterning is finished (Figure 4.5 (h)).

4.4.2 Anodic Bonding and Fabrication of Metallization Layer in the DRIE Process

The anodic bonding process is a very popular bonding process with high bond strengths and relatively low bonding temperatures [83-85]. In DRIE process, the silicon wafer which will form the structural material is bonded to the glass substrate with anodic bonding.

Figure 4.5 (i) shows the bonded wafers using anodic bonding. After this bonding step, the next process step is the formation of metallization layer. Similar to the nickel electroplating process, the metallization layer is formed using lift-off. The photoresist used in this process is again SJR5740 for its high thickness. After SJR5740 is patterned with exposure (Figure 4.5 (j)), chromium/gold (200 Å / 1000 Å) is evaporated (Figure 4.5 (k)). The metallization layer is formed after the lift-off process (Figure 4.5 (l)).

4.4.3 Fabrication of Oxide Mask and DRIE Step in the DRIE Process

After the metallization step, the wafers are ready for DRIE step. This step is the most critical step in this process since it defines the minimum dimensions and high aspect ratio vertical comb fingers.

The masking layer for the DRIE is the silicon oxide layer. The reason for using silicon oxide for the masking layer is its high selectivity in DRIE process. To create silicon oxide mask, the first process step is to deposit silicon oxide using PECVD (Figure 4.5 (m)). After the deposition of the oxide, S1813 is patterned with exposure (Figure 4.5 (n)). This patterned photoresist is used as the masking layer to pattern the silicon oxide layer. To patterns silicon oxide, regular RIE step is used. After the

RIE step (Figure 4.5 (o)), DRIE etching is done using both the oxide layer and the photoresist as the masking layer (Figure 4.5 (p)). The process ends with stripping masking photoresist and oxide layers (Figure 4.5 (r)).

Similar to the nickel electroplating process, the dicing issue is also important in DRIE process. After DRIE step, the wafers are coated with a protective photoresist before the dicing process and then the dicing is performed. After the dicing, the protective photoresist is removed sample by sample.

The process steps in this process have already been completed at METU-MET facilities, except the DRIE step. The DRIE step has been done at STS, one of the producers of the DRIE machine. A DRIE machine is already purchased from STS and the installation of it was in progress during the writing of this thesis.

4.5 Summary

This chapter presents the fabrication processes and the details of these processes for the realization of MEMS accelerometers and gyroscopes. The processes used in this study are SOIMUMPs process, nickel electroplating process, and DRIE process.

SOIMUMPs process is a commercial MUMPs (Multi-User MEMS Processes) process which uses SOI wafers and pattern the top silicon layer for the structural material. This process is realized by CRONOS Inc. Nickel electroplating process is a surface micromachining process which creates nickel electroplated structures on top of the glass wafer. All the process steps of this process are realized in METU-MET facilities. The DRIE process is an advanced process that uses dry anisotropic bulk micromachining technique. The structural material is silicon and the substrate is glass. The glass substrate is bonded to silicon wafer using anodic bonding and then the silicon wafer is etched with DRIE for structural layer formation. All the process steps, except masking oxide formation and DRIE step, are realized in METU-MET facilities.

CHAPTER 5

FABRICATION AND TEST RESULTS

This chapter presents the fabrication and test results of designed accelerometers and gyroscopes. The chapter also gives the test results of the accelerometers hybrid connected to a readout circuit to achieve accelerometer systems. Section 5.1 briefly discusses the fabrication results of each three fabrication processes. Section 5.2 explains the basic tests done to each accelerometer and gyroscope sample and summarizes these test results. Section 5.3 gives the open loop test results of hybrid connected accelerometer prototypes using SOIMUMPs accelerometer and nickel electroplated accelerometer with MS3110 commercial capacitive readout circuit. Finally, Section 5.4 summarizes the chapter and discusses the test results.

5.1 Fabrication Results of Each Three Processes

This section explains the fabrication results of each three processes. Our first process is SOIMUMPs process which is fabricated by CRONOS Inc. The devices are designed and sent for fabrication in CRONOS fabrication facilities. The second process is nickel electroplating process, which is realized in METU-MET facilities. The last process is the DRIE process. The fabrication steps of this process are also realized in METU-MET facilities except the oxide formation and DRIE etching steps.

5.1.1 Fabrication Results of SOIMUMPs Process

In SOIMUMPs process, the sensors are fabricated and sent to us. The main problem in this process is that, the sensors are diced after released. Hence, the critical dimensions are severely damaged in the dicing step.

Figure 5.1 shows SOIMUMPS accelerometers. An open-loop hybrid connected accelerometer prototype is prepared using a low frequency, high sense capacitance SOIMUMPs accelerometer sample.

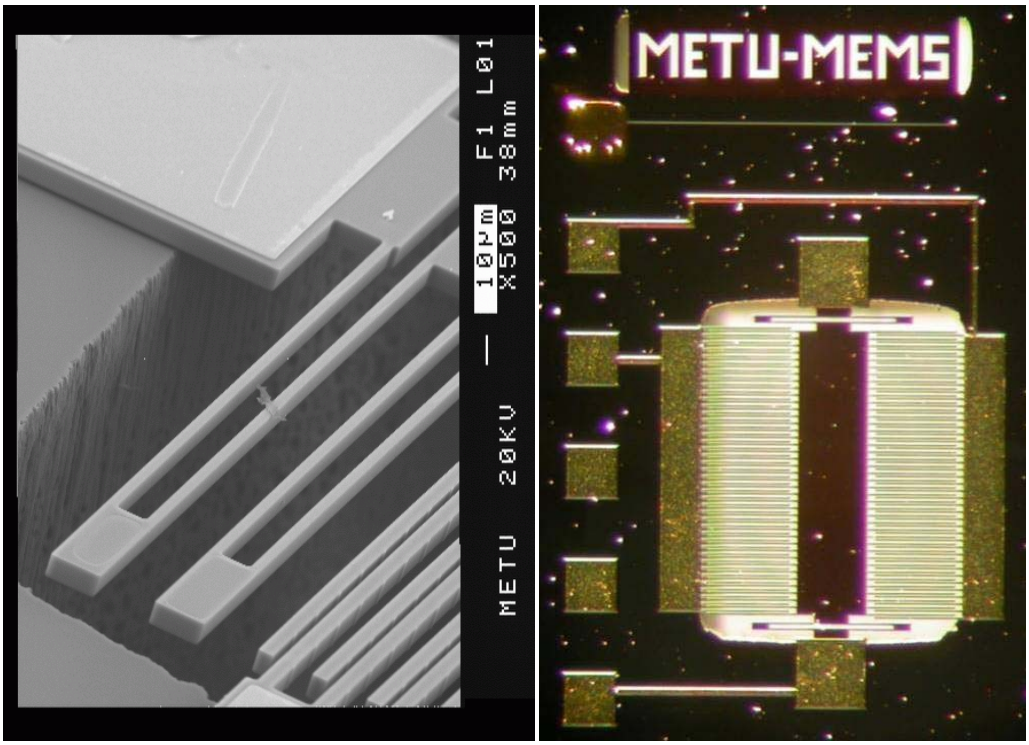

Figure 5.1: SOIMUMPs accelerometers. Due to thicker features, the accelerometer samples do not suffer from transportation problems.

Figure 5.2 shows the broken SOIMUMPs gyroscope structures. The gyroscope structures have thinner but shorter finger structures but the accelerometers have thicker and longer finger structures. Hence, the gyroscope features are severely

damaged during the die separation of the sensors. An undamaged gyroscope sample cannot be obtained due to this dicing problem; however basic tests can be done to the gyroscope samples for the verification of the sensor operation.

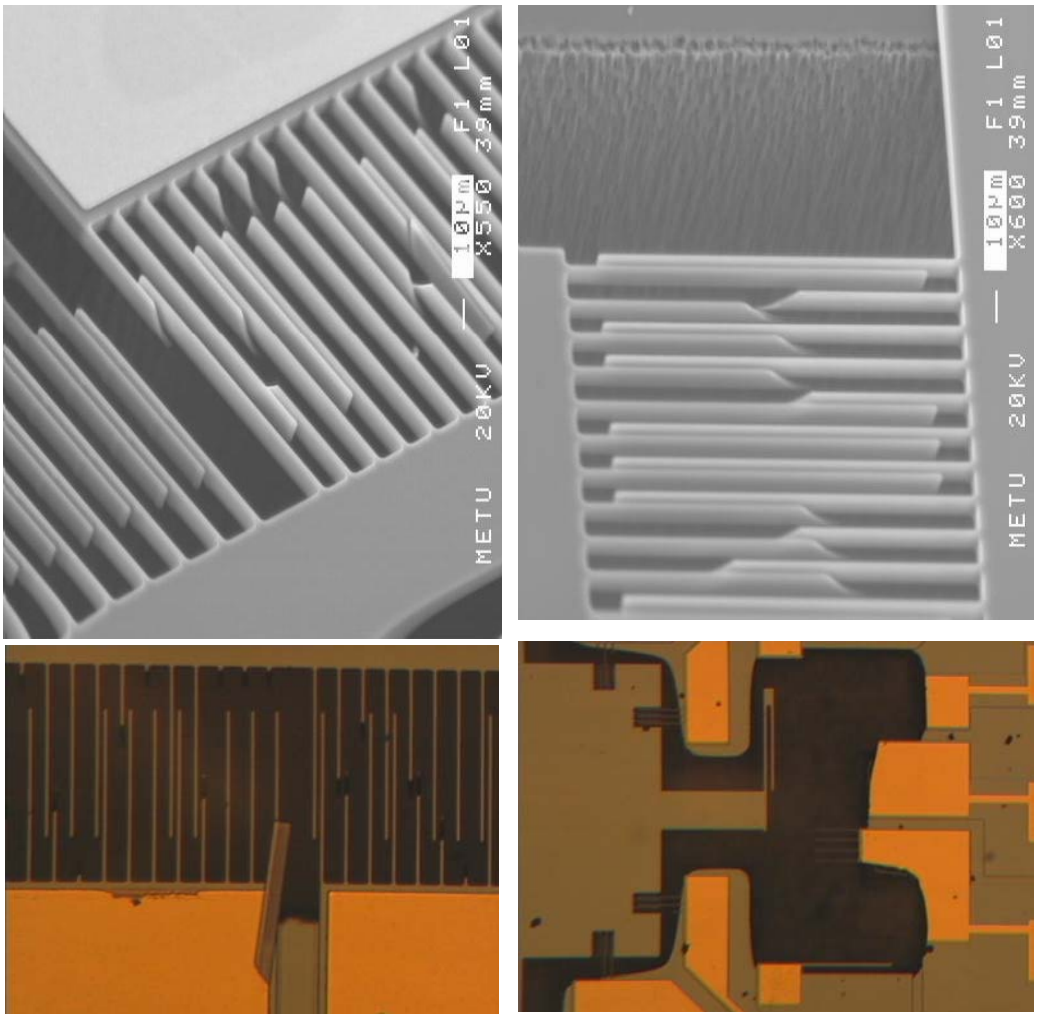

Figure 5.2: Broken SOIMUMPs gyroscope structures.

5.1.2 Fabrication Results Nickel Electroplating Process

The nickel electroplating process results have turned out to be the most expected fabrication results. In the design period, we have expected that the mold photoresist will shrink in each direction during the exposure; hence the electroplated region area will increase. So, we compensate this shrinking of the mold photoresist in our design drawings. As expected, the mold photoresist shrink in each direction during the exposure, hence the electroplated area increase during the fabrication. Hence we have achieved designed resonance frequency values for our sensors. We have also expected that during the hardbake of the mold photoresist, the shape of the photoresist will change, especially in the bulky regions. This deformation in the shape is also observed after the fabrication, especially near the spring regions of the accelerometers. We expect that this deformation will cause drift in the accelerometer system and will also change the resonance frequency of the accelerometer, but the hardbake part is critical due to the fact that the photoresist cannot withstand the electroplating solution without the hardbake. Moreover, we expect that the uniformity of the electroplating thickness will not be perfect, and hence there will be height difference throughout the wafer. The fabricated samples also verify our expectations.

Figure 5.3 shows a fabricated nickel electroplated accelerometer sample and shows the deformation in the spring regions. Figure 5.4 shows the SEM pictures of accelerometer samples. A hybrid connected accelerometer prototype is formed using a high performance fabricated accelerometers.

Figure 5.5 shows a fabricated nickel electroplated gyroscope. The operation of the gyroscopes is verified with basic tests that will be explained in Section 5.2.

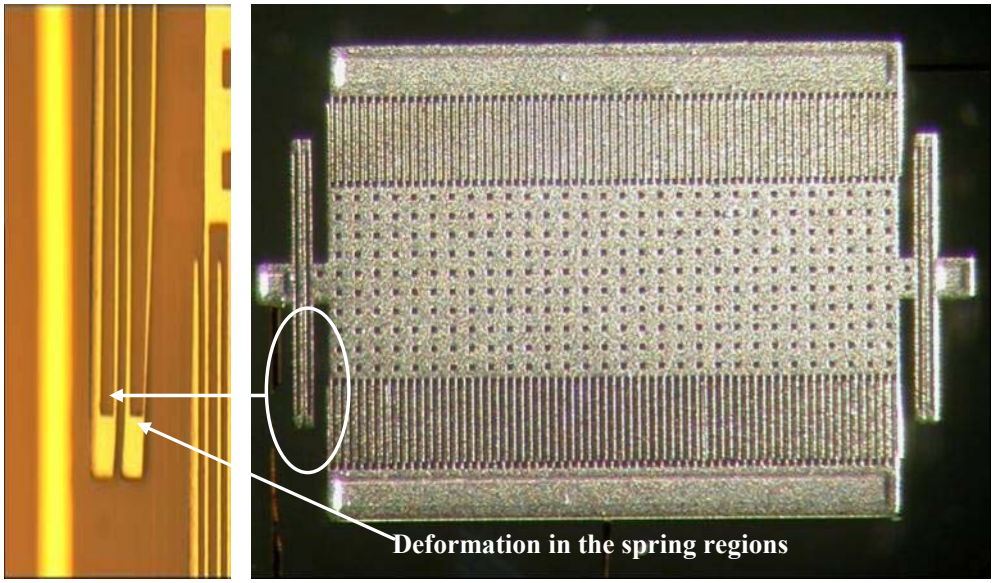

Figure 5.3: A fabricated nickel electroplated accelerometer and the deformation in the spring regions.

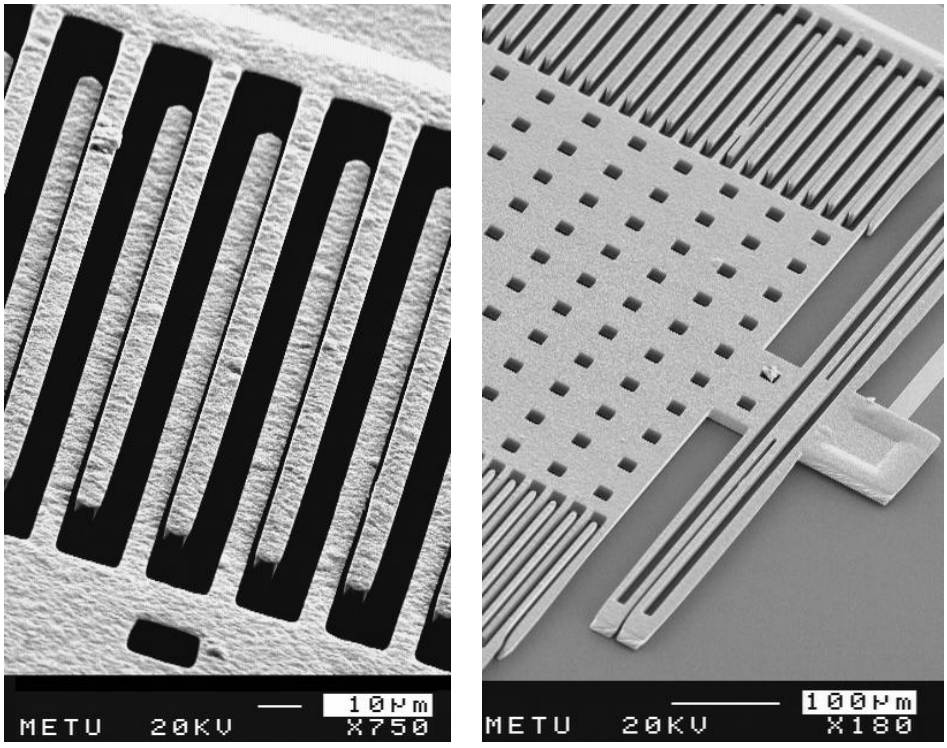

Figure 5.4: SEM pictures of fabricated nickel electroplated accelerometers.

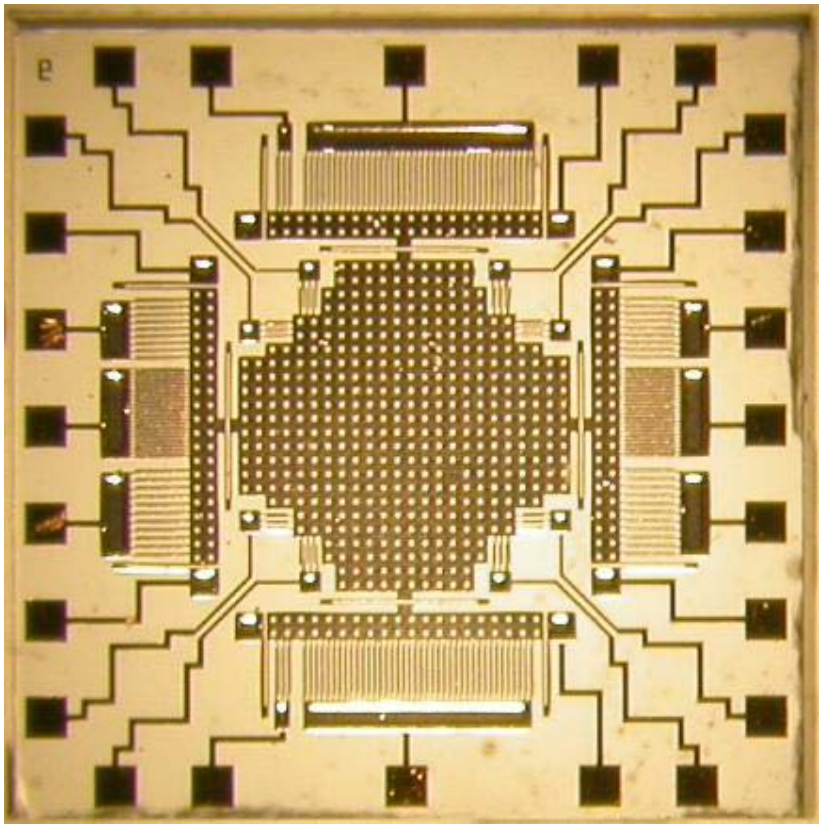

Figure 5.5: A photograph of fabricated nickel electroplated gyroscope.

5.1.3 Fabrication Results of DRIE Process

The DRIE process results show that this process still needs optimization. The DRIE etch step is the most critical step in this process and it seems that we have lost all our samples during this step. The wide openings of the samples are etched away with a faster etch rate and then while the smaller opening regions are being etched, there occurs large under etches in the wide opening regions, or in the small opening regions the etching is not finished. These are the main problems in DRIE process.

Figure 5.6 shows a SEM picture of a DRIE gyroscope. The fabrication of this gyroscope seems to be good; however the gyroscope still suffers from the DRIE fabrication problems. Figure 5.7 shows SEM pictures of DRIE samples, and the problematic regions are better seen from this picture. In this figure, it can be shown

that in wide opening regions the etching is finished, but in small opening regions the etching is not finished. We can also see some notching effect. The problems may be minimized with a better mask set. The DRIE mask should be designed such that, the etch regions should be minimized and also the opening dimensions should be as similar as possible. However, with the mask sets designed in this study, a working accelerometer or gyroscope cannot be achieved.

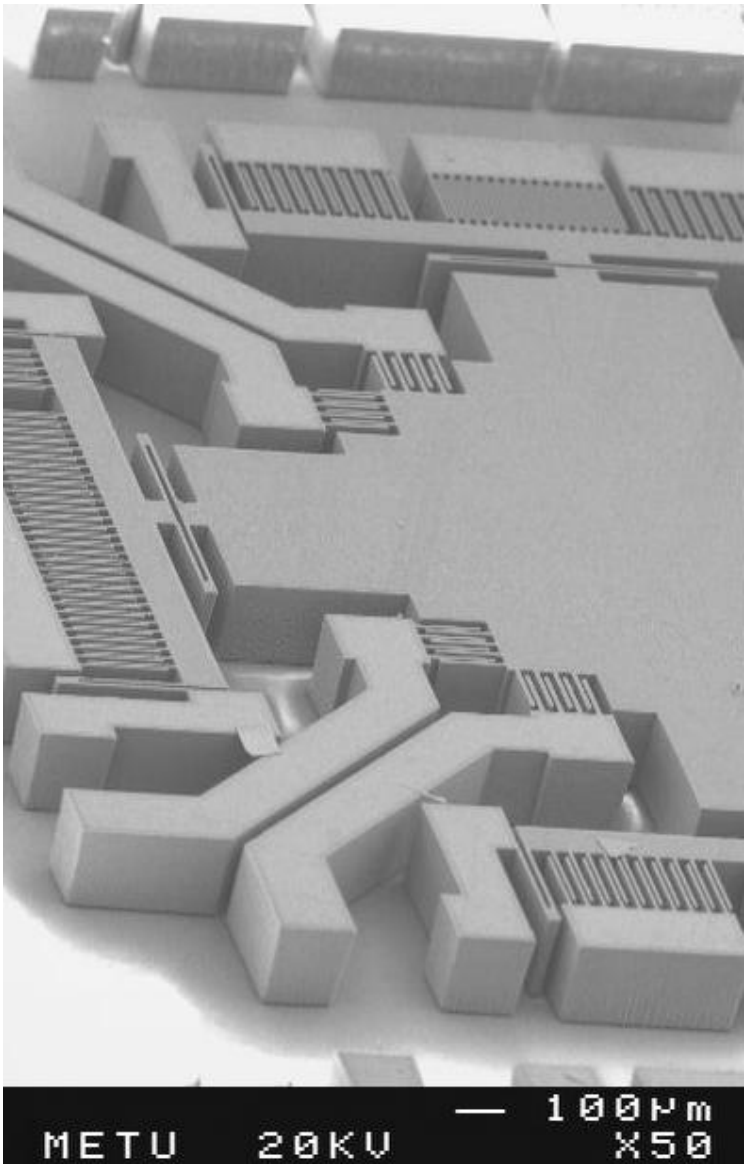

Figure 5.6: SEM picture of a DRIE gyroscope. The structure is 200 µm thick.

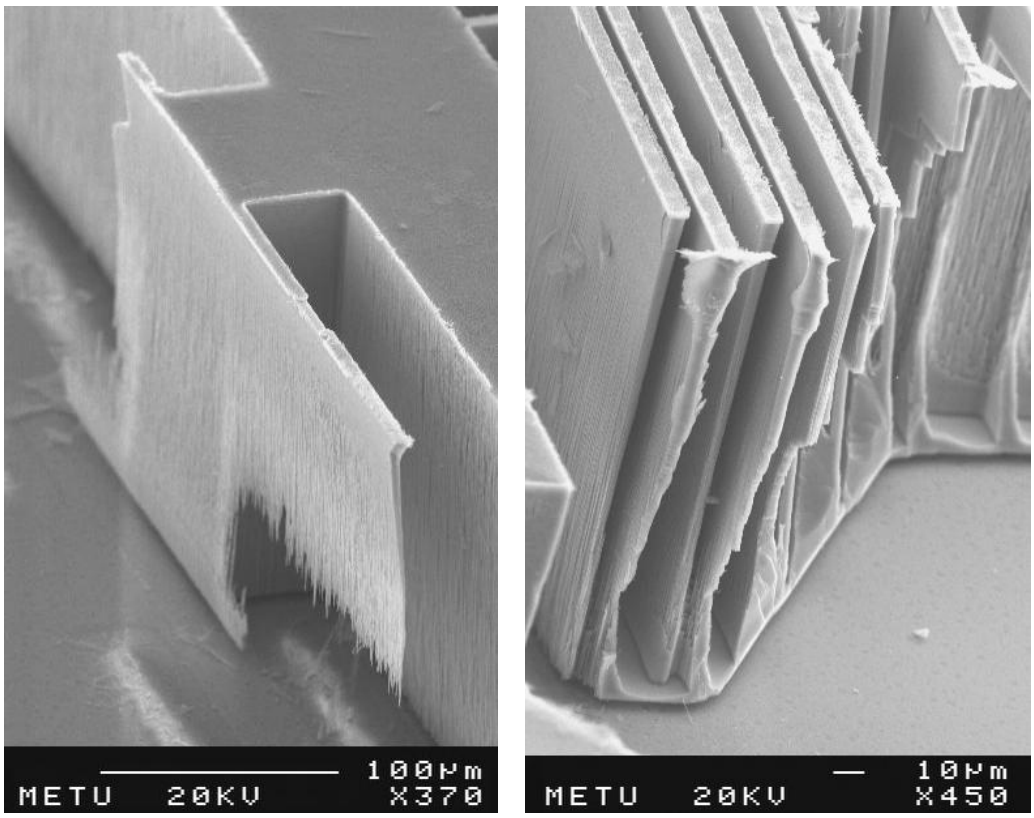

(a) (b)

Figure 5.7: SEM pictures of DRIE samples. (a) The critical structures are damaged due to notching effect. (b) The etching in small openings is not finished.

5.2 Basic Tests Performed on the Accelerometer and the Gyroscope Samples

When the fabrication period is finished, four basic tests are performed on capacitive micromachined sensors. These are the stiction test, short circuit test, capacitance test, and resonance frequency test. After these tests, the accelerometer samples showing the highest performance are used for constructing hybrid connected accelerometer systems.

The stiction test is performed using a probe station. Firstly, if the samples have glass substrate as in DRIE and nickel electroplating process, the samples are put backwards and observed with a microscope. This microscope check is a quick check to determine whether the samples are released or not. If the samples seem to be released, then the samples are put on to the probe station with the front sides looking up. Using a probe, the proof mass is pushed a little in the sensitive direction. If the deflection is seen in the springs, it means that the structure is released.

The short circuit test is also performed using the probe station. Using two probes and connecting these probes to the multimeter, we can understand if the proof mass is short circuited to the sense or drive electrodes or not. If we encounter a short circuit, we may remove this region with the laser cut. But this step is only applicable to nickel electroplated sensors because the electroplated nickel is rather soft material that can be cut with the laser cutter.

The third test is the capacitance test. The samples that pass from the previous two tests are tested with the impedance analyzer to measure the capacitances between sense electrodes and the proof mass and between drive electrodes and the proof mass. This test is also performed using the probe station. First, the probes are connected to the impedance analyzer. Then, the probes are touched to the pads of appropriate capacitances. Then, the impedance analyzer gives the capacitance value of the appropriate capacitance. Moreover, sweeping the voltage between the pads forming the capacitor, pull-in voltage of the sensor is extracted. The key point in these measurements is the calibration step. Before taking any data, the calibration should be done not to measure false values.

The last test is resonance frequency test. Figure 5.8 shows the test setup. This test is also performed using the probe station. The sensor is driven with a varying frequency AC signal from one end of the drive or sense electrode and then the output is taken from the other end of the electrode. The magnitude and the phase of the output shows the magnitude and phase response of the system. From this data, we

can see that the peak value of the magnitude response, which corresponds to the resonance frequency of the sensor.

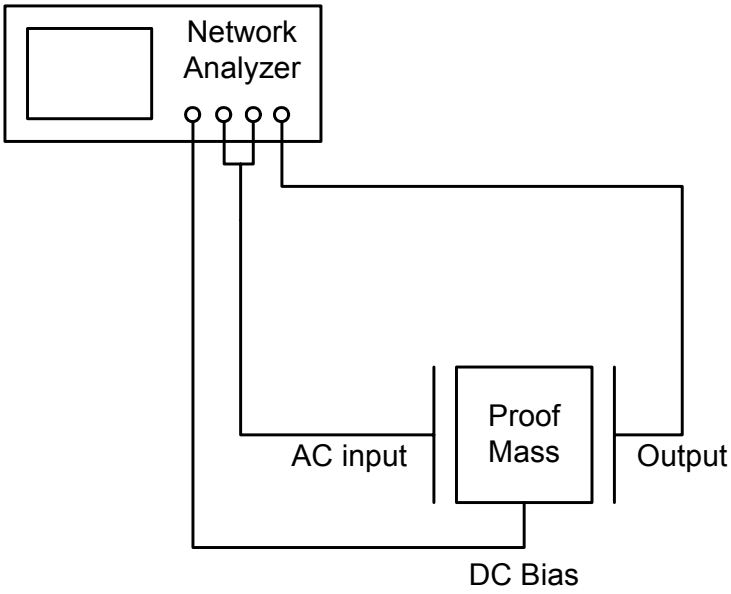

Figure 5.8: Resonance frequency test setup.

For SOIMUMPs and nickel electroplating process, capacitance and resonance frequency tests can be performed, but for DRIE process, there is not any testable sensor for these tests.

Figure 5.9-16 show the capacitance test results of each sensor. The capacitance between the proof mass and the sense electrode increases with the applied voltage across them. Hence, after the pull-in voltage, the proof mass sticks to the sense electrode. Table 5-1 compares the designed pull-in voltages with the measured values.

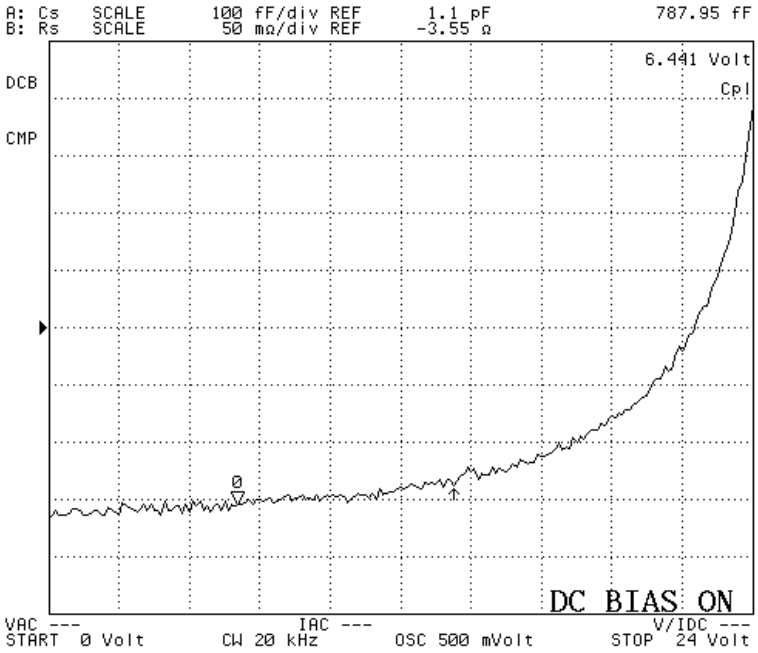

Figure 5.9: Capacitance test result of accelerometer prototype-1. The pull-in voltage is measured as 25 V.

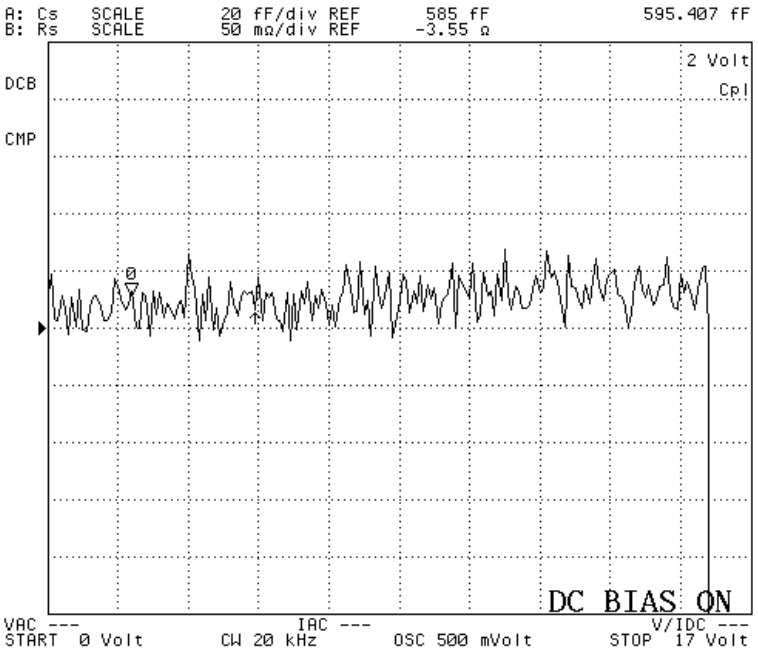

Figure 5.10: Capacitance test result of accelerometer prototype-2. The pull-in voltage is measured as 16V.

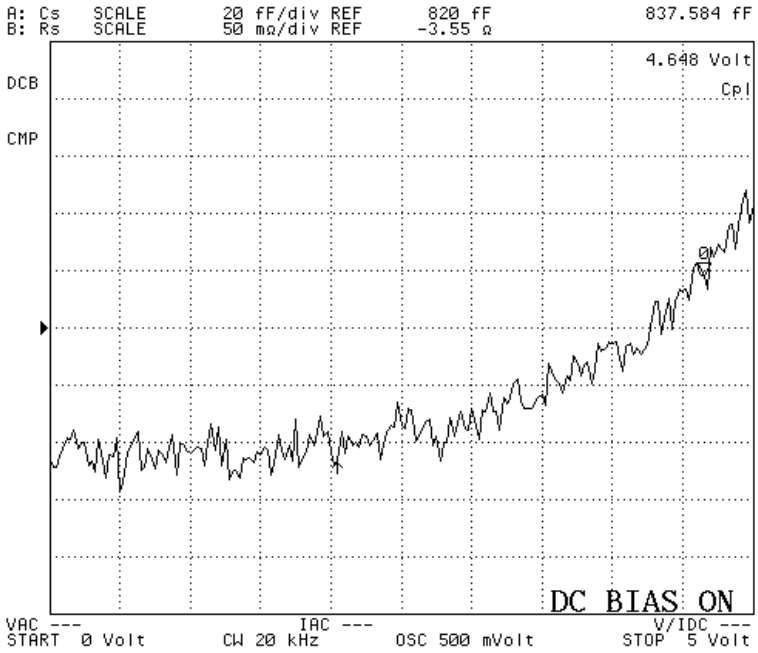

Figure 5.11: Capacitance test result of accelerometer prototype-3. The pull-in voltage is measured as 5.2 V.

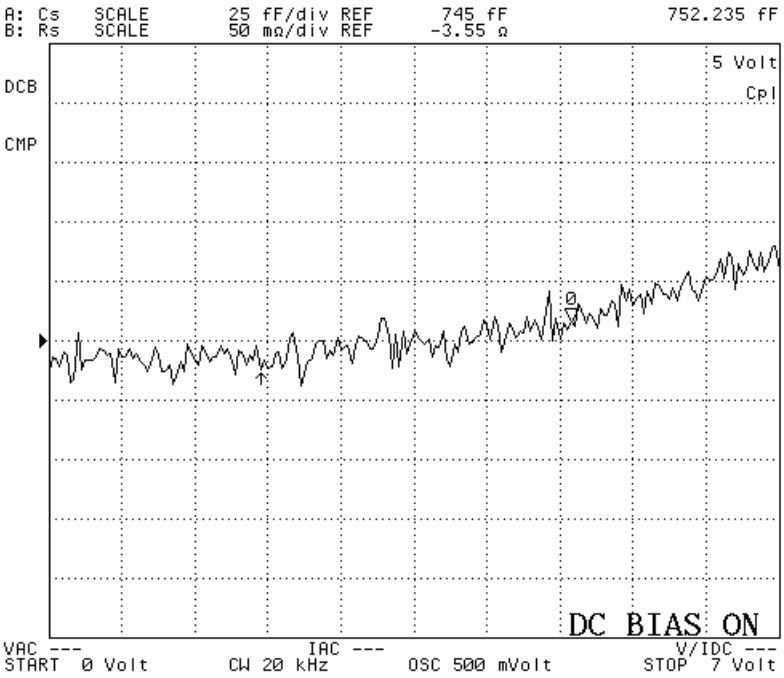

Figure 5.12: Capacitance test result of accelerometer prototype-4. The pull-in voltage is measured as 8.8V.

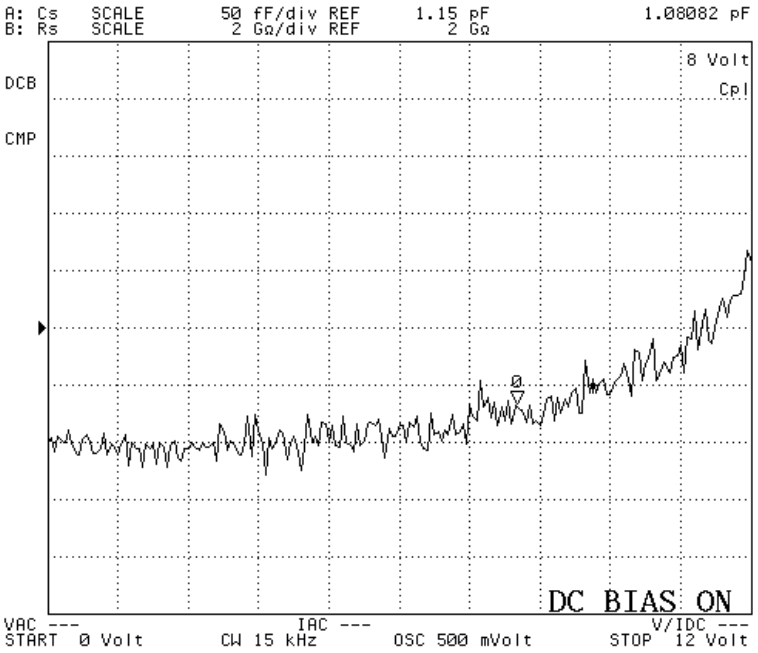

Figure 5.13: Capacitance test result of accelerometer prototype-5. The pull-in voltage is measured as 12V.

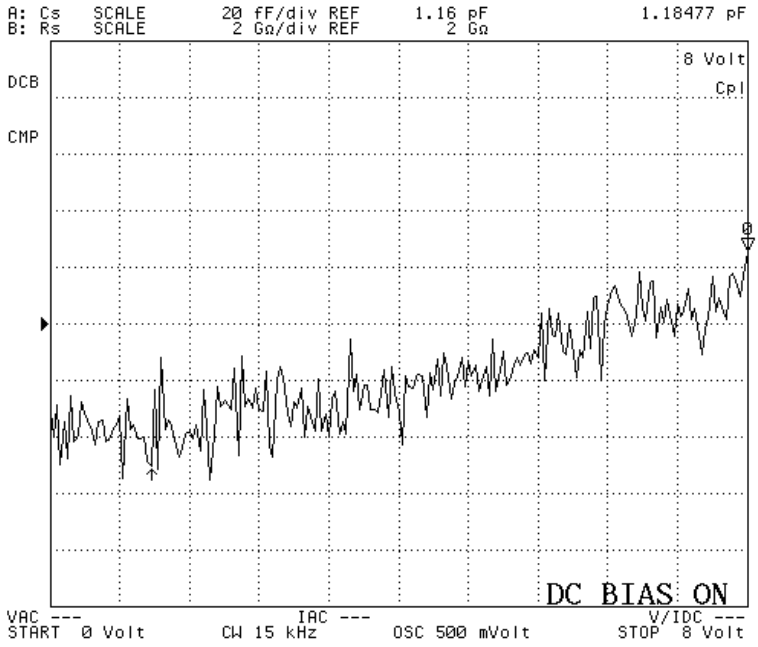

Figure 5.14: Capacitance test result of accelerometer prototype-6. The pull-in voltage is measured as 10V.

Figure 5.15: Capacitance test result of gyroscope prototype-1. The pull-in voltage is measured as 19V.

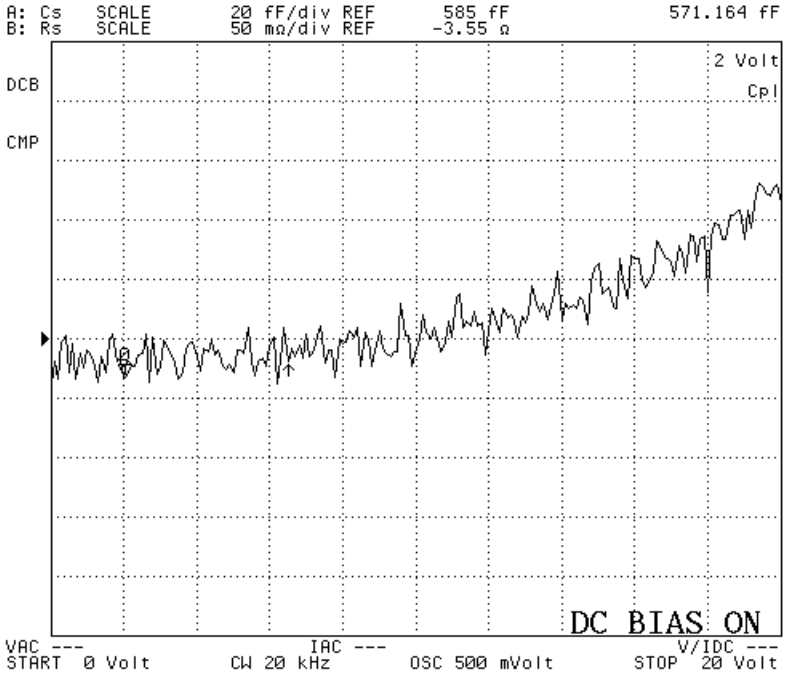

Figure 5.16: Capacitance test result of gyroscope prototype-2. The pull-in voltage is measured as 24V.

Table 5-1: The comparison of measured pull-in voltages with the designed values.

Sensor	Process	Calculated pull-in voltage	Measured pull-in voltage
Accelerometer prototype-1	SOI	26 V	25 V
Accelerometer prototype-2	SOI	13 V	16 V
Accelerometer prototype-3	SOI	3.0 V	5.2 V
Accelerometer prototype-4	Nickel	6.2 V	8.8 V
Accelerometer prototype-5	Nickel	10 V	12 V
Accelerometer prototype-6	Nickel	6.7 V	10 V
Accelerometer prototype-7	DRIE	7.1 V	-
Accelerometer prototype-8	DRIE	15 V	-
Gyroscope prototype-1	SOI	33 V	19 V
Gyroscope prototype-2	Nickel	50 V	24 V
Gyroscope prototype-3	DRIE	43 V	-
Gyroscope prototype-4	DRIE	92 V	-

Figure 5.17-22 shows the resonance frequency test result of designed accelerometers, and Table 5-2 compares the test results with the designed values for capacitance and resonance frequency tests. The upper and lower pictures in each figure show the magnitude and phase response, respectively. The frequency value provided on top right of the each display window shows the resonance frequency value of the sensor. Theoretically, the magnitude response should make a sharp decrease after making a peak value, and the phase response should decrease and stay at its low value. However, theoretical magnitude and phase response cannot be obtained due to parasitic effects. However, the resonance peak can still be observed clearly. We can say that the fabricated sensors have very similar resonance frequency values as the designed values and have a larger capacitance values due to fringing field capacitances as the designed capacitance values as expected. Especially the resonance frequency values of nickel electroplating accelerometers show that the magnitude of shrinking of the mold photoresist in the exposure step is well characterized and the Young's Modulus of the electroplated nickel is well estimated in the design section. However, the deformation of the mold photoresist due to hardbake creates a small displacement in the original rest position of the proof mass and creates a capacitance mismatch in nickel electroplate accelerometers. This capacitance mismatch may cause nonlinearity and offset at the output of the hybrid

connected accelerometer system because proof mass displacement due to external acceleration will not create a symmetric capacitance difference for same magnitude, different direction acceleration inputs. Considering the bandwidth issue and these tests results, prototype-3 and prototype-5 are selected as the sensor element for the hybrid connected accelerometer system prototypes.

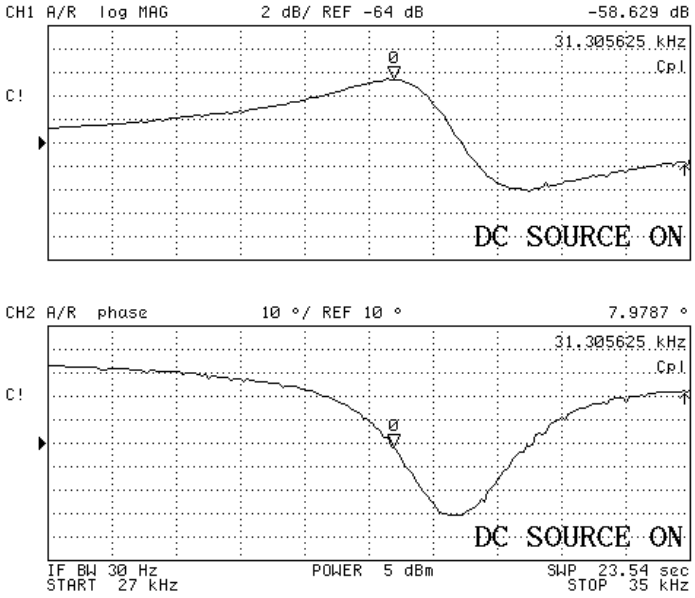

Figure 5.17: Resonance frequency test result of accelerometer prototype-1. The measured resonance frequency is 31.3 kHz. The upper and lower pictures show the magnitude and phase response, respectively. The frequency value shown on top right of the each display window shows the resonance frequency value of the sensor. Theoretically, the magnitude response should make a sharp decrease after making a peak value, and the phase response should decrease and stay at its low value. However, due to parasitic effects theoretical results cannot be obtained.

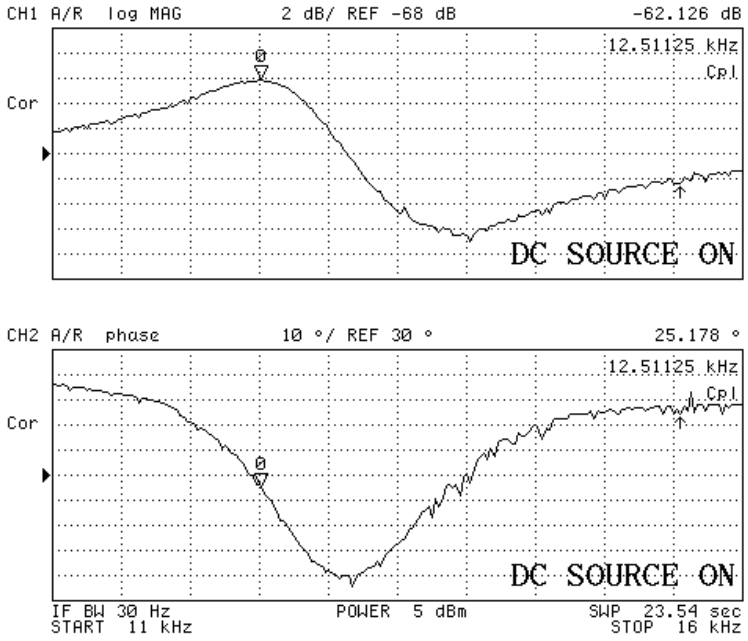

Figure 5.18: Resonance frequency test result of accelerometer prototype-2. The measured resonance frequency is 12.51 kHz.

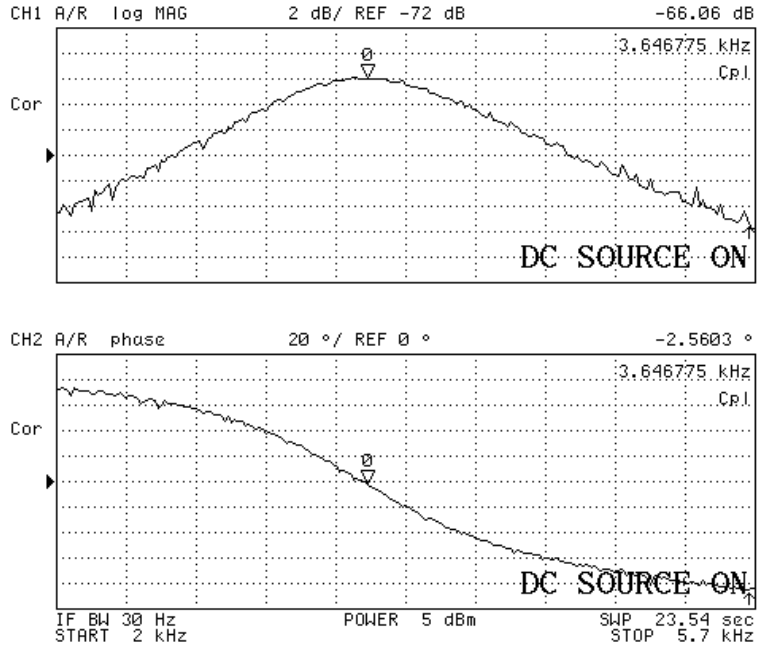

Figure 5.19: Resonance frequency test result of accelerometer prototype-3. Measured resonance frequency is 3.65 kHz.

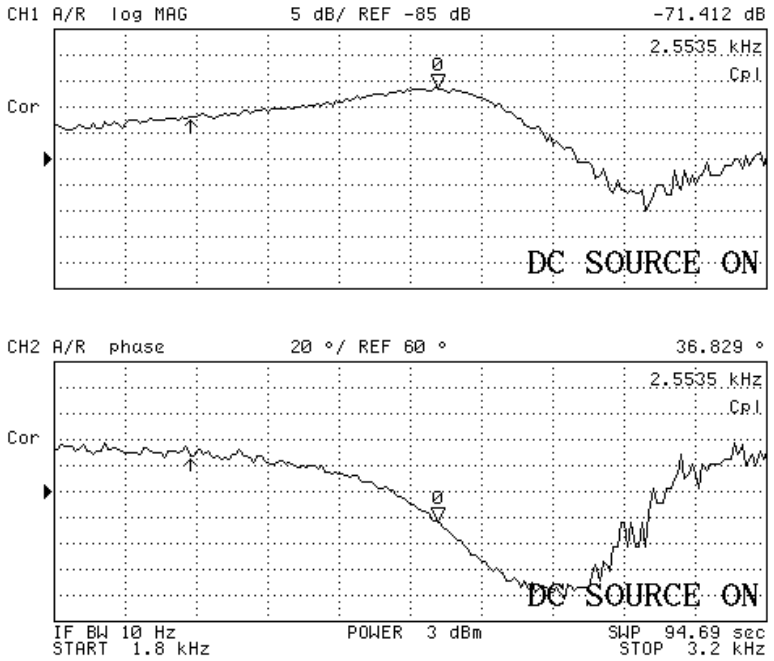

Figure 5.20: Resonance frequency test result of accelerometer prototype-4. Measured resonance frequency is 2.55 kHz.

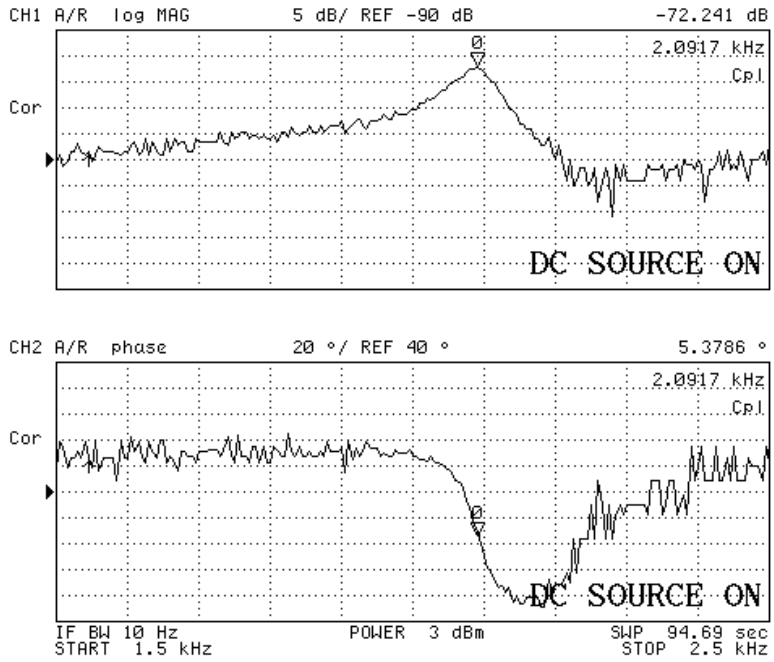

Figure 5.21: Resonance frequency test result of accelerometer prototype-5. Measured resonance frequency is 2.09 kHz.

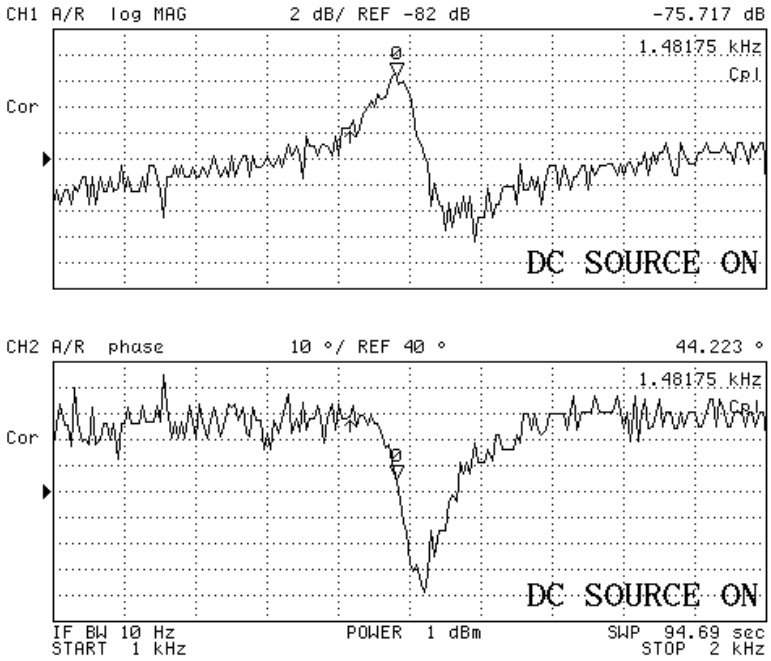

Figure 5.22: Resonance frequency test result of accelerometer prototype-6. Measured resonance frequency is 1.48 kHz.

Table 5-2: Comparison of capacitance and resonance frequency test results with the designed values for the designed accelerometers.

Prototype	Process	Calculated Sense Cap.	Measured Sense Cap.	Calculated Resonance Frequency	Measured Resonance Frequency
1	SOI	2 x 520 fF	750 fF	31.5 kHz	31.3 kHz
2	SOI	2 x 415 fF	620 fF	11.1 kHz	12.5 kHz
3	SOI	2 x 520 fF	750 fF	3.73 kHz	3.65 kHz
4	Ni	2 x 557 fF	800 fF	2.66 kHz	2.55 kHz
5	Ni	2 x 696 fF	920 fF	2.05 kHz	2.09 kHz
6	Ni	2 x 696 fF	900 fF	1.54 kHz	1.48 kHz
7	DRIE	2 x 5.12 pF	-	2.97 kHz	-
8	DRIE	2 x 10.5 pF	-	2.76 kHz	-

For the gyroscopes, the resonance frequency test is done for both drive and sense modes. For nickel electroplated gyroscopes, the sensor is connected to a unity gain buffer circuitry and then the resonance frequency test is performed. This unity gain buffer increases the signal level to reasonably high values. However, in SOIMUMPs

gyroscopes, the tests are done without connecting buffer circuits. Figure 5.23-26 gives the results of resonance frequency tests of drive and sense mode of designed gyroscopes. For the capacitance test, the gyroscopes are connected to impedance analyzer with the help of probe station. However, for SOIMUMPs gyroscopes, due to the broken comb fingers reasonable results are not expected. Table 5-3 summarizes the capacitance and resonance frequency test results for gyroscopes and compares these results with the designed values. The measured resonance frequencies are very similar to the designed values. For the capacitance values, the results are larger than the calculated values due to fringing field capacitances as expected. For DRIE samples, there is no testable gyroscope sample.

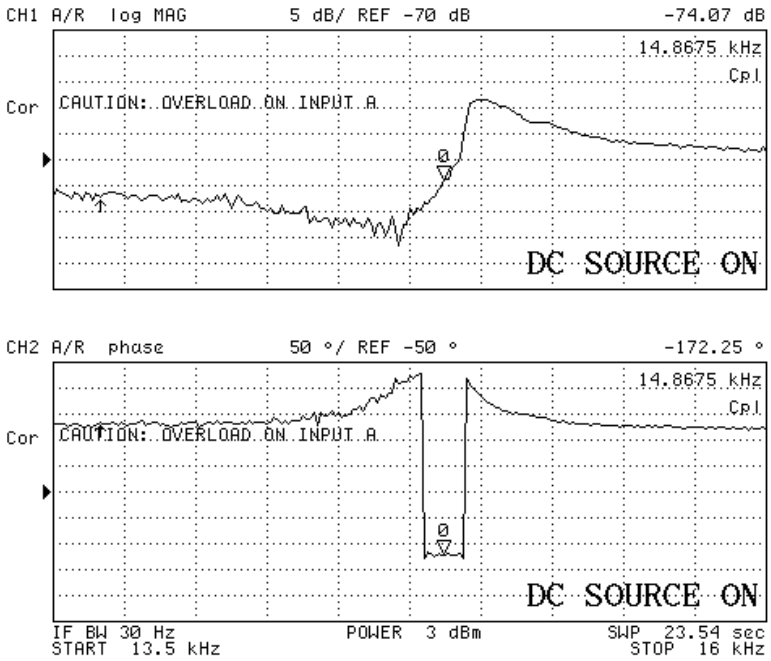

Figure 5.23: Resonance frequency test result of the drive mode of prototype-1, which is the SOIMUMPs gyroscope. The measured resonance frequency is 14.87 kHz. In the drive mode of the gyroscope, theoretically the magnitude response makes a step instead of a peak, and the phase response makes a peak instead of a step. This is due to the configuration of the drive mode capacitances. In this figure, the phase response indeed makes a peak; however, this peak cannot be observed clearly due to 360° phase change. This is a display error due to network analyzer. One of the reasons for this error is low capacitance values due to process limitations and broken sense comb fingers.

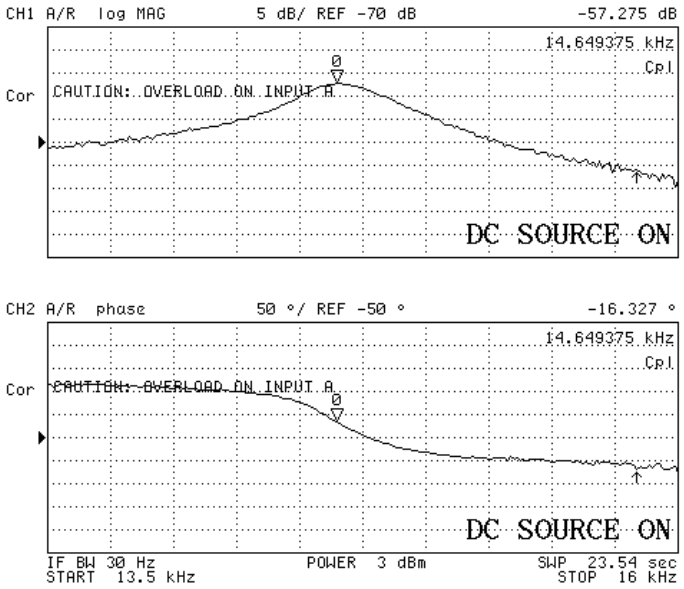

Figure 5.24: Resonance frequency test result of the sense mode of prototype-1. The measured resonance frequency is 14.65 kHz. Sense mode magnitude/phase response is similar to that of the accelerometers.

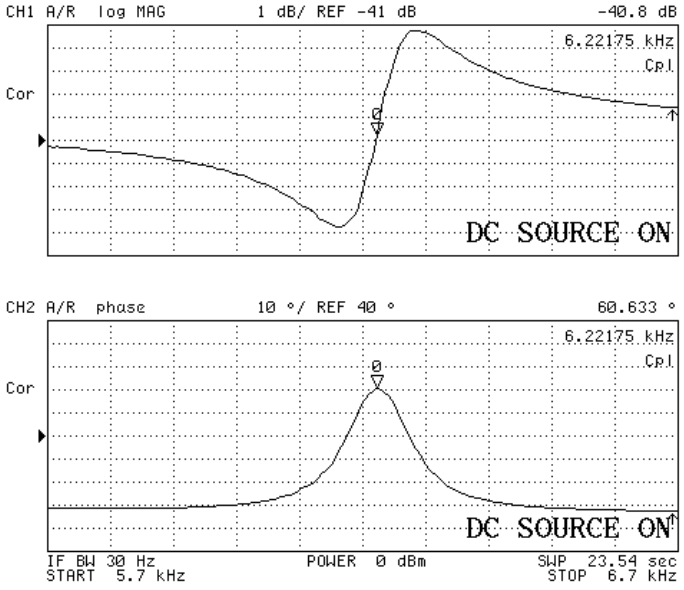

Figure 5.25: Resonance frequency test result of the drive mode of prototype-2, which is a nickel gyroscope. The measured resonance frequency is 6.22 kHz. The response is clearer than the response of SOIMUMPs sample, because this sample has more sense capacitance and is connected to a buffer circuitry which improves the output response.

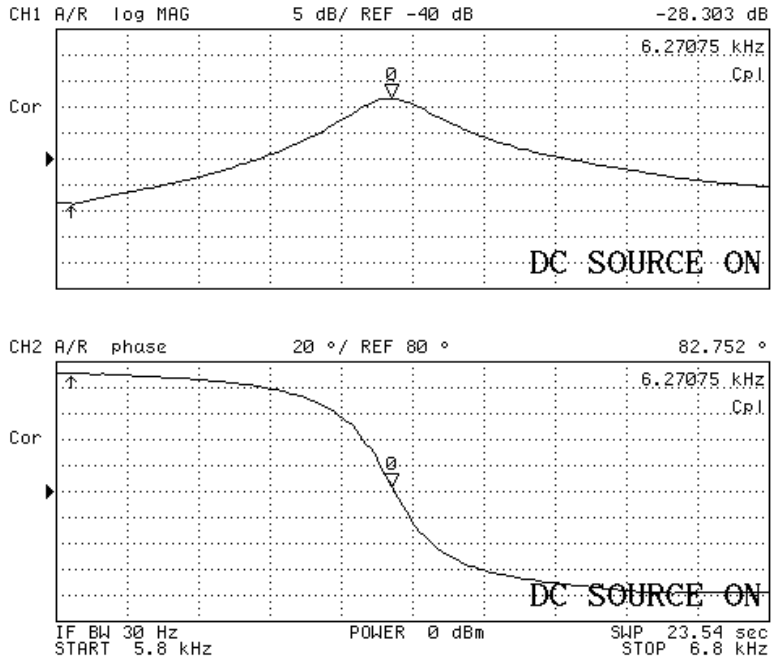

Figure 5.26: Resonance frequency test result of the sense mode of prototype-2. The measured resonance frequency is 6.27 kHz.

Table 5-3: Capacitance and resonance frequency test results for the designed gyroscopes and comparison of these test results with the designed values.

Parameter	Prototype-1	Prototype-2	Prototype-3	Prototype-4
Process	SOIMUMPs	Nickel electroplating	DRIE	DRIE
Calculated drive mode resonance frequency	15.82 kHz	6.07 kHz	6.57 kHz	6.57 kHz
Measured drive mode resonance frequency	14.87 kHz	6.22 kHz	-	-
Calculated sense mode resonance frequency	15.70 kHz	6.05 kHz	6.54 kHz	6.54 kHz
Measured sense mode resonance frequency	14.65 kHz	6.27 kHz	-	-
Calculated sense capacitance	153 fF	363 fF	1.97 pF	2.36 pF
Measured sense capacitance	240 fF	450 fF	-	-

5.3 Open Loop Tests of Accelerometers and MS3110 Readout Circuitry Hybrid System

Accelerometer prototype-3 and prototype-5 are selected for the sensor element of the hybrid system. The aim of these prototypes is to form an accelerometer system that satisfies the goals of this study. Hence, the prototypes should have bias circuitries, sensor part, MS3110 readout part, and amplifier stages that bring the output signal to desired levels.

Figure 5.27 shows the first generation hybrid accelerometer system that uses accelerometer prototype-3 and MS3110 readout circuitry, and Figure 5.28 shows the block diagram of this prototype. MS3110 is a switched-capacitor integrator type differential open-loop capacitive readout circuit. The circuit generates the clock signals necessary for the reading of capacitance mismatch due to external acceleration input, and then converts this capacitance mismatch to voltage with the help of a switched capacitor integrator. Next, the circuit eliminates high frequency component of the signal with a Low-Pass-Filter (LPF), and finally amplifies the resultant signal. The pole of this LPF is 500 Hz, and this pole determines the total 3dB bandwidth of the system, because the 3dB bandwidth of the accelerometer is nearly its resonance frequency. The bias voltages required for MS3110 circuit, and amplifier stages to adjust the voltage gain of the system is not provided with the first generation hybrid system, but these circuitries can be constructed, and the bias voltages can be supplied externally.

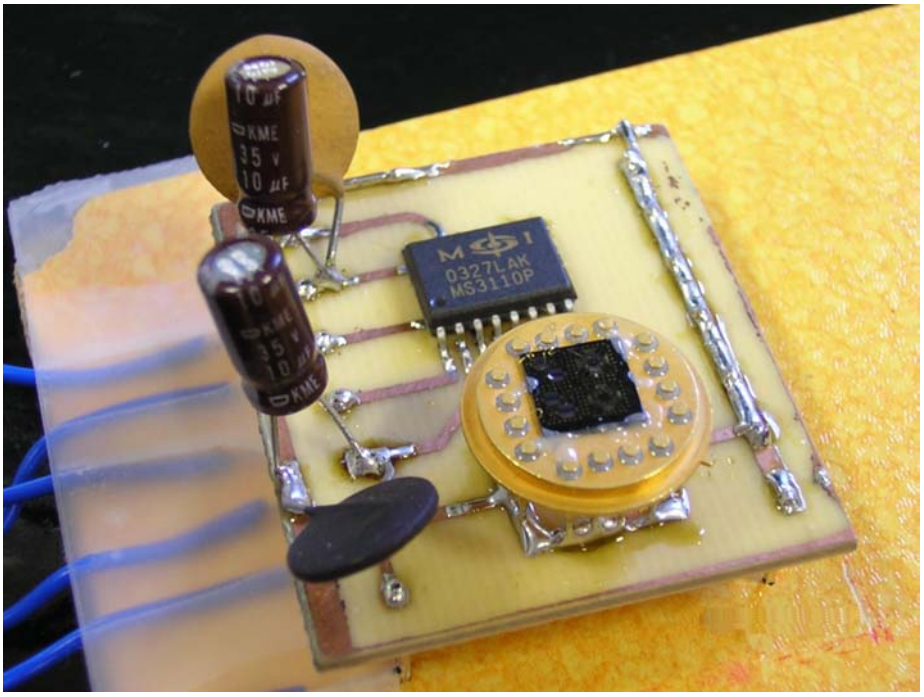

Figure 5.27: First generation hybrid accelerometer system that uses accelerometer prototype-3 and MS3110 readout circuitry.

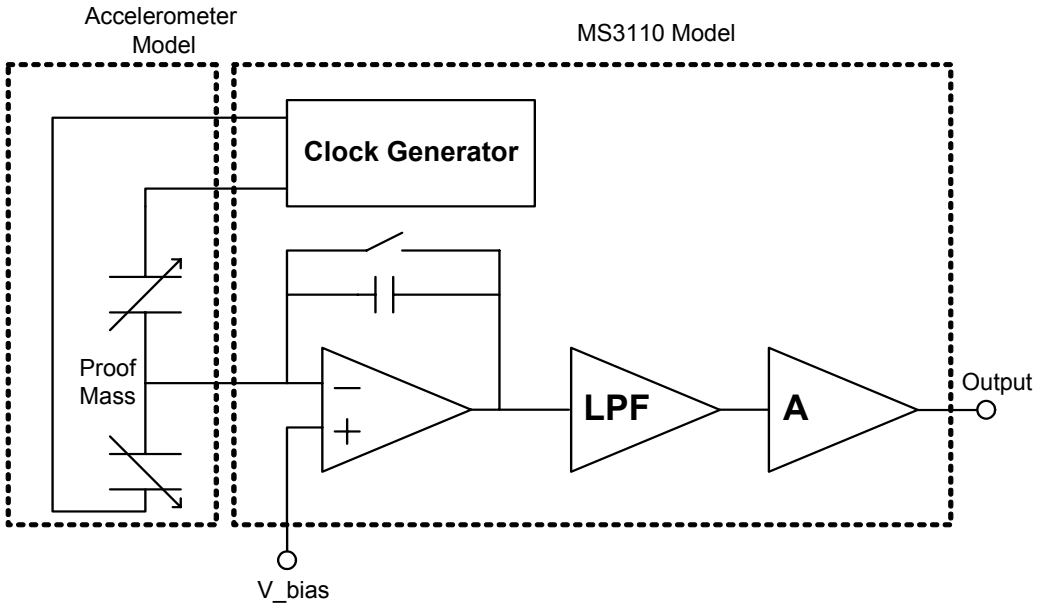

Figure 5.28: Block diagram of the first generation hybrid system. The system is composed of the accelerometer and MS3110 switched-capacitor integrator type differential capacitive readout circuit. The pole of low-pass-filter (LPF) also determines 3dB bandwidth of the system.

The hybrid system is tested with an index table with 1° resolution in the test facilities of ASELSAN and TUBITAK-SAGE. The results of this test give the nonlinearity and the sensitivity of the sensor. Figure 5.29 shows the result of this test indicating 22.2 mV/g sensitivity and 0.1 % nonlinearity. The sensitivity value can be increased with amplifier circuitries but the resolution cannot be improved due to the fact that the amplifiers will also amplify the noise levels. Hence the performance of the hybrid system can be understood with the noise test. The noise test is done with a spectrum analyzer. Figure 5.30 shows the result of the noise test indicating a 17.75 µV/√Hz average noise level. The noise level is expresses in g/√Hz by dividing voltage noise level to sensitivity of the sensor. Hence, the average noise level of the hybrid system is found as 799 µg/√Hz. The peak noise is also measured and found as 1.8 mg/√Hz. The noise level is not satisfactory for the design goals. Hence, the construction of bias and amplifier circuitries is not realized for this sensor.

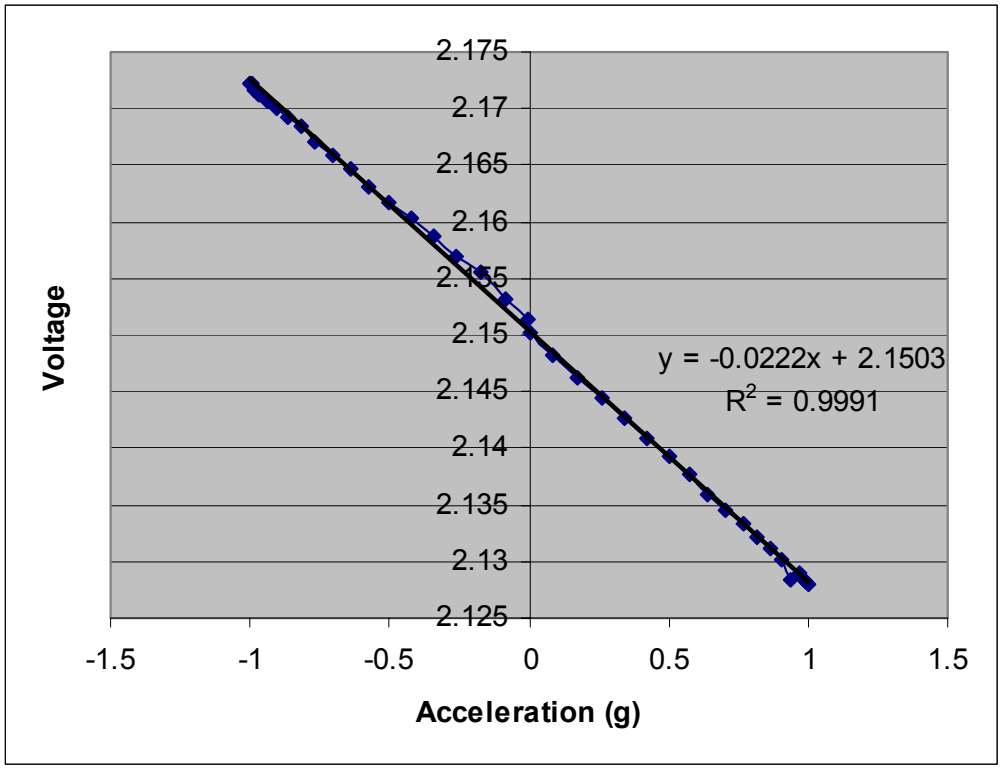

Figure 5.29: The results of index table tests showing nonlinearity and sensitivity of the first generation hybrid accelerometer system. The system shows less than 0.1 % nonlinearity and 22.2 mV/g sensitivity.

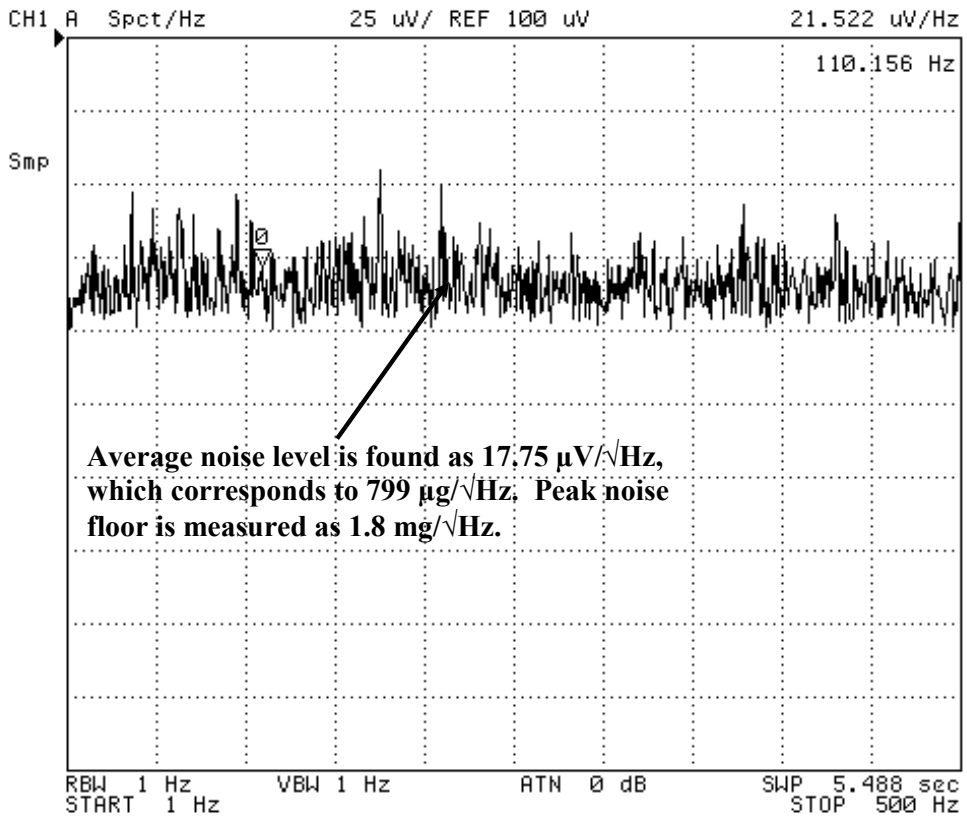

Figure 5.30: Noise test result of first generation hybrid accelerometer system. Average noise level is found as 17.75 µV/√Hz which corresponds to 799 µg/√Hz. Peak noise floor is measured as 1.8 mg/√Hz.

Table 5-4 gives the comparison of measured and calculated noise levels of the hybrid system. The total noise of the system has two components: mechanical and electrical noise. The theoretical mechanical noise can be calculated using Brownian Noise expression [26], and the electrical noise estimation can be done checking MS3110 datasheet. However, in the MS3110 datasheet, the electrical noise expression is given as "Input Capacitance Resolution," but it is not clear whether this capacitance resolution is single-ended or differential. Therefore, the calculation of electrical noise changes if the capacitance resolution provided in MS3110 datasheet is single-ended or differential. Table 5-4 gives the electrical noise estimation for both single-ended and differential case. However, the noise simulation results show that the given capacitance resolution should be single-ended.

Table 5-4: Comparison of measured and calculated noise levels of the first generation hybrid system. There are two different electrical noise, and hence total noise calculations. This is due to the electrical noise expression given in MS3110 datasheet. The electrical noise is expressed as "Input capacitance resolution" but it is not clear whether this resolution is single-ended or differential. However, the measured noise floor show that the resolution provided in the datasheet should be single-ended.

Parameter	Value
Calculated mechanical noise	71 μg/√Hz
Calculated electrical noise if the resolution data provided in MS3110 datasheet is *single-ended* capacitance resolution.	782 μg/√Hz
Calculated electrical noise if the resolution data provided in MS3110 datasheet is *differential* capacitance resolution.	391 μg/√Hz
Calculated total noise if the resolution data provided in MS3110 datasheet is *single-ended* capacitance resolution.	785 μg/√Hz
Calculated electrical noise if the resolution data provided in MS3110 datasheet is *differential* capacitance resolution.	397 μg/√Hz
Measured total average noise	799 μg/√Hz
Measured total peak noise	1.8 mg/√Hz

The second generation hybrid accelerometer system is constructed using prototype-5 and the MS3110 commercial readout circuitry. Unlike the previous hybrid system, this system has bias and amplifier circuitries additional to sensor and readout part. Figure 5.31 shows the picture of this hybrid system, and Figure 5.32 shows the block diagram of this system. The index table test is done to find the nonlinearity and the sensitivity of the system, and also the sensor is put into a rate table to extract these values under higher acceleration values. Figure 5.33 shows the index table test result of the second generation hybrid system and Figure 5.34 shows the results of rate table test. These tests show that the system shows less than 0.3 % nonlinearity even under high acceleration values and an almost 1 V/g sensitivity value. Moreover, the noise level of the system is tested with a spectrum analyzer and 228 μV/√Hz, which corresponds to 228 μg/√Hz average noise floor and 375 μg/√Hz peak noise floor, is achieved. Figure 5.35 shows the result of the noise test of the second generation

hybrid system. The scale factor asymmetry is also extracted as 2.58 % from the nonlinearity test results.

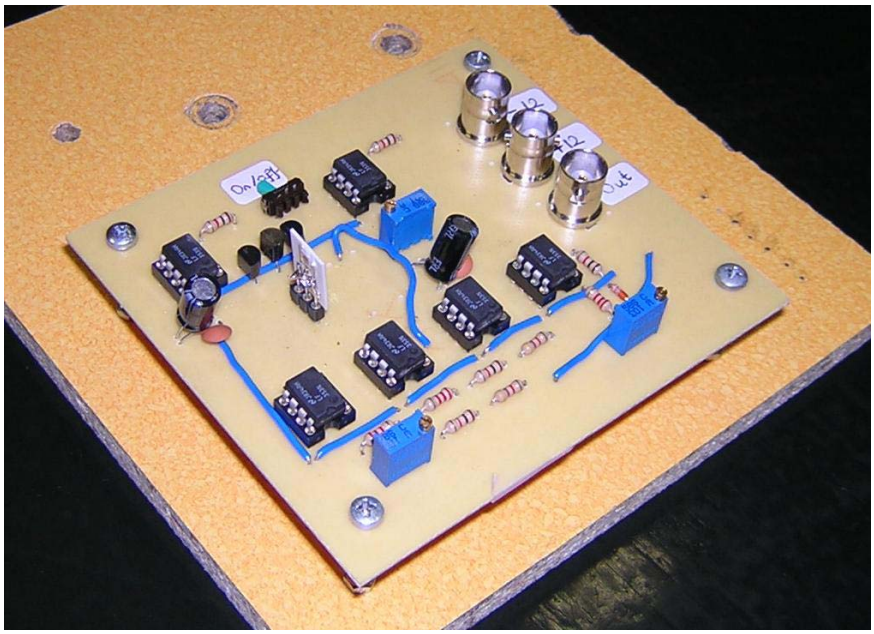

Figure 5.31: The second generation hybrid accelerometer system. This system uses a nickel accelerometer, and has bias circuitries and amplifier stages additional to first generation hybrid system.

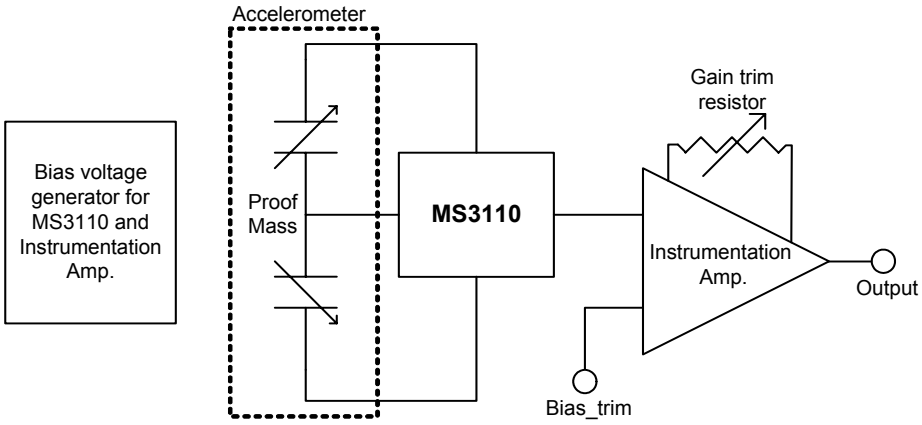

Figure 5.32: The block diagram of second generation hybrid system. The instrumentation amplifier eliminates the DC offset of MS3110 and provides the necessary voltage gain. Bias voltage generator provides the necessary bias voltages to appropriate circuit blocks.

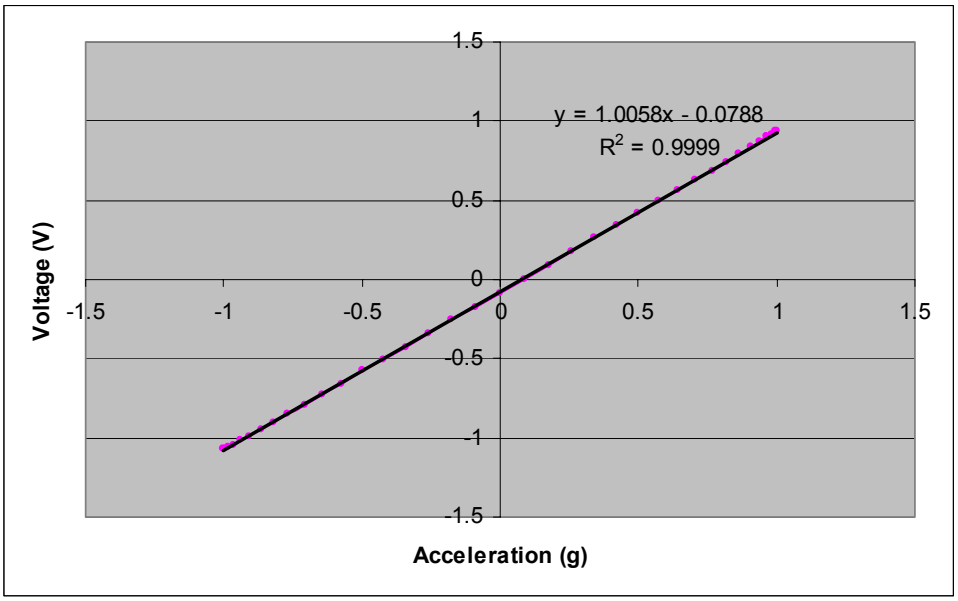

Figure 5.33:. Test results of second generation hybrid system using index table. The system shows less than 0.1 % nonlinearity and almost 1 V/g sensitivity for acceleration inputs in the range of ± 1g.

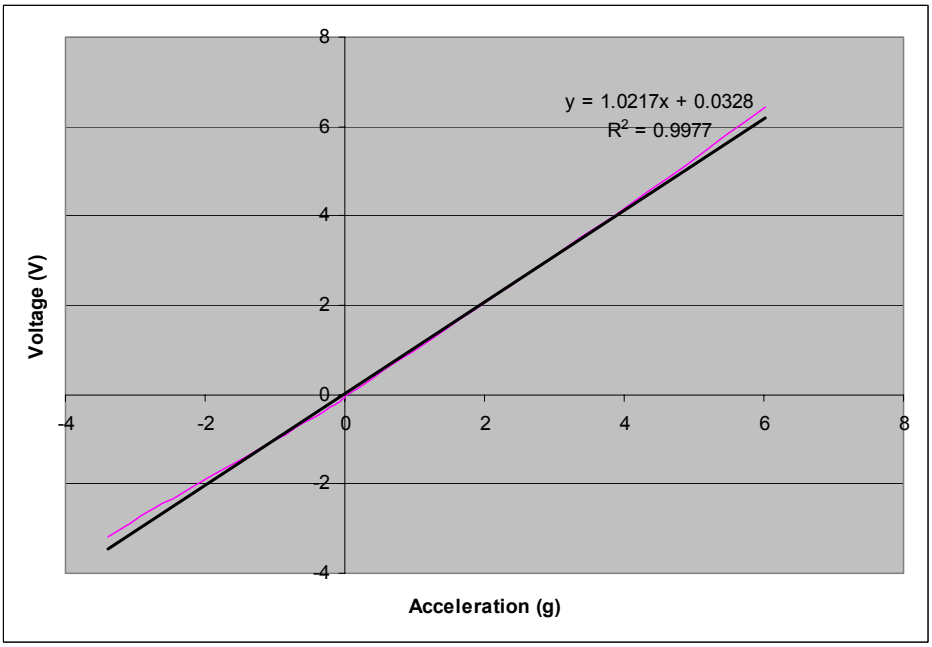

Figure 5.34: Test results of second generation hybrid system using rate table. The system shows less than 0.3 % nonlinearity and almost 1 V/g sensitivity for high acceleration inputs. The device is able to be tested in a range of (-3g, 6g) acceleration inputs.

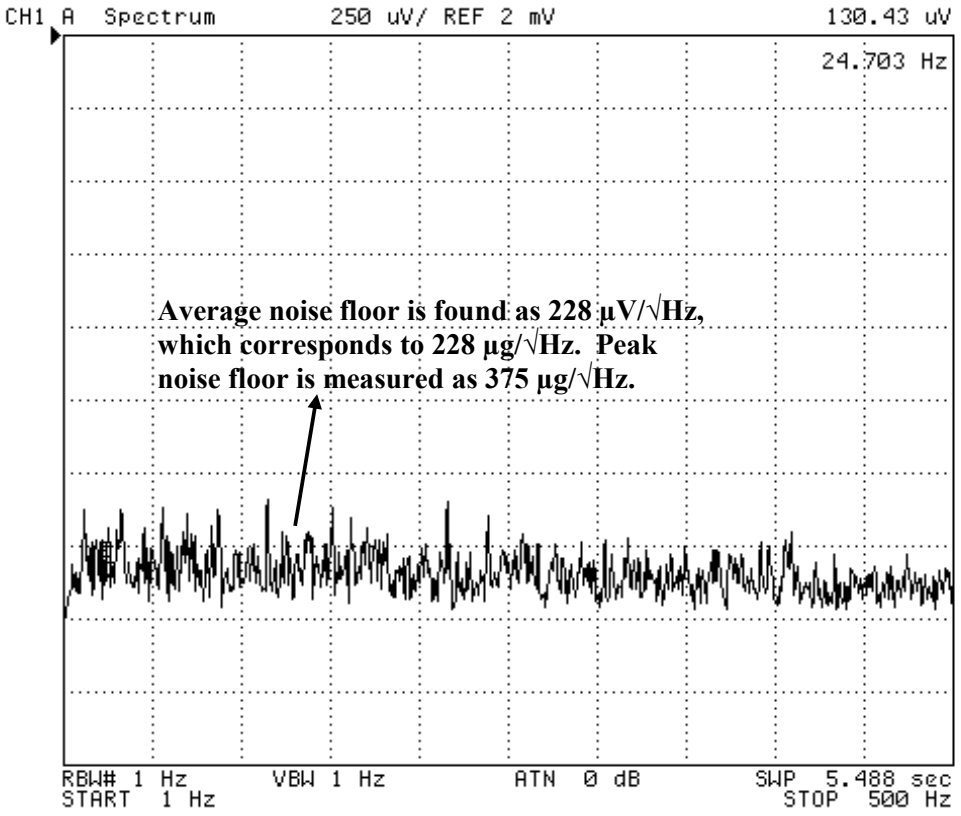

Figure 5.35: Noise test results of the second generation hybrid accelerometer system. Average noise level is 228 µV/√Hz corresponding to 228 µg/√Hz, and peak noise floor is measured as 375 µg/√Hz.

Table 5-5 gives the comparison of calculated and measured noise levels of second generation hybrid accelerometer system. Similar to the case in the first generation hybrid system, two different electrical noises are calculated considering the uncertainty in the electrical noise expression of MS3110 circuit. The single-ended resolution estimation yields a closer noise level. Moreover, considering that the noise level provided in MS3110 datasheet is a conservative value, the single-ended resolution estimation will yield much better total noise estimation.

Table 5-5: Comparison of calculated and measured noise levels of second generation hybrid system. Two different electrical noises are calculated similar to the case of first generation hybrid system. Single-ended resolution estimation yields a closer total noise estimation.

Parameter	Value
Calculated mechanical noise	12.7 μg/√Hz
Calculated electrical noise if the resolution data provided in MS3110 datasheet is *single-ended* capacitance resolution.	292 μg/√Hz
Calculated electrical noise if the resolution data provided in MS3110 datasheet is *differential* capacitance resolution.	146 μg/√Hz
Calculated total noise if the resolution data provided in MS3110 datasheet is *single-ended* capacitance resolution.	292 μg/√Hz
Calculated electrical noise if the resolution data provided in MS3110 datasheet is *differential* capacitance resolution.	147 μg/√Hz
Measured total average noise	228 μg/√Hz
Measured total peak noise	375 μg/√Hz

The bias drift of this hybrid system is also tested. For this purpose, the system is turned on for 3 hours and the output is monitored with 4 samples/sec data rate. Then this test is repeated for three times. Figure 5.36 shows the result of this bias drift test. From the test results, we can observe that the sensor has two kinds of bias drift value. First one is "Run-to-run Bias Drift" and the second one is "Long-Term Bias Drift." The run-to-run bias drift value is the maximum change of the bias value for each start-up of the system. Taking the maximum average bias difference, it can be concluded that the run-to-run bias drift of the sensor is 16.6 mV corresponding to 16.6 mg. The long-term bias drift is the maximum change of the sensor output with time. From the measured data, we can say that the sensor output makes an overshoot for 15-30 minutes, and then settles. This overshoot is probably due to the warming of bias and amplifier circuit parts. If we ignore this overshoot, we can extract the long-term bias drift as the maximum long-term bias drift of each measurement as 19 mV, corresponding to 19 mg.

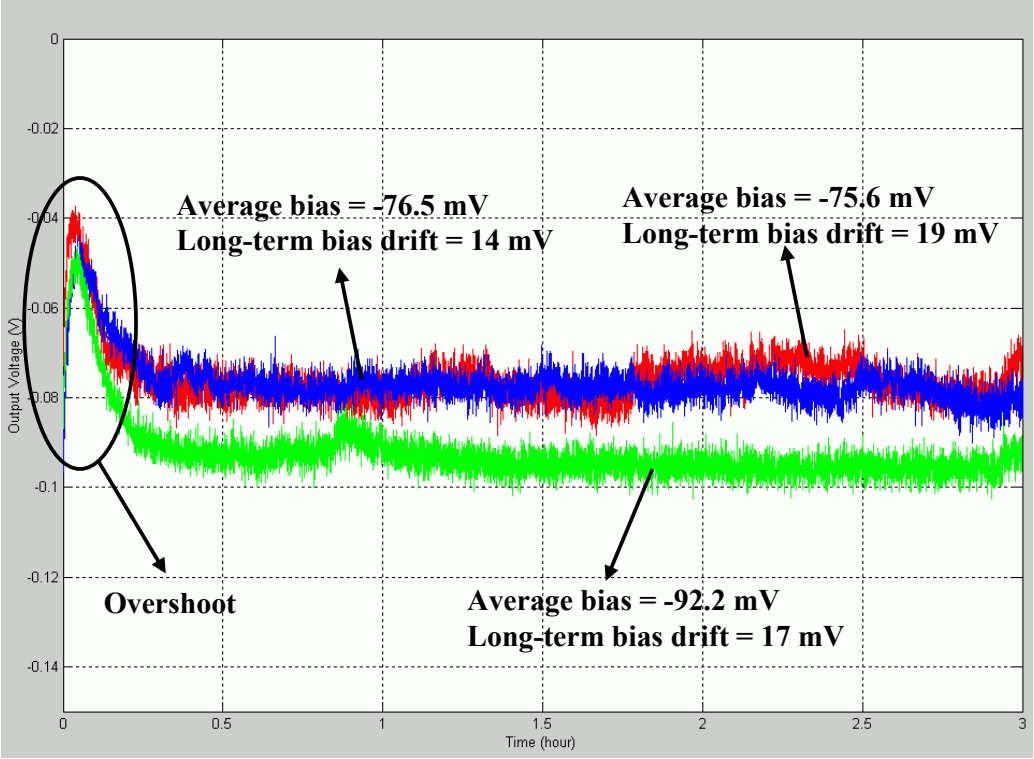

Figure 5.36: Bias drift test result of second generation hybrid accelerometer system. The maximum average bias difference gives the run-to-run bias drift, and the maximum long-term bias drift of each test result gives the long-term bias drift of the system. The measured run-to-run bias drift and long-term bias drift of the sensor are found as 16.6 mV and 19 mV corresponding to 16.6 mg and 19 mg, respectively.

The final tests performed on the second generation hybrid system are cross-axis sensitivity tests and temperature sensitivity test. Table 5-6 provides cross-sensitivity test results. For cross-axis sensitivity test, the system is given +1g, and -1g acceleration along its cross axes. The test results show that the cross-axis sensitivity of the system is negligibly small. For temperature sensitivity test, the system is put into an oven. Then the temperature is swept from -40°C to +40°C and then +40°C to -40°C. Figure 5.37 shows the results of temperature test. The results show that the system output to temperature change can be predicted and compensated with external electronics. However, it can also be observed that the output do not have exactly the same value at the same temperature value for increasing and decreasing temperature case. The reason for this result is probably the potentiometers used in the system,

and also the socket that the accelerometer is placed. The resistance value of potentiometers changes with temperature and probably does not come to its original value exactly, and changes the output. Also the legs that connects the accelerometer to its socket are affected by the temperature change and do not preserve their original position. This position change causes an axis misalignment and changes the output. A better packaged system will have lower errors.

The resolution is the primary performance criteria for accelerometers, and the resolution of the accelerometer is determined by the noise floor of the hybrid accelerometer system. The noise level of the system is determined by both mechanical and electrical noise and in nowadays sensors the main limitation for the accelerometer systems comes from the electrical noise. Table 5-7 summarizes the properties of the second generation hybrid system. It also shows the mechanical and total noise floor of the system indicating the importance o the readout circuit part. The sensor resolution performance is mainly limited by the electrical noise. With a lower noise electrical circuitry, a higher performance accelerometer system can be achieved.

Table 5-6: Cross-axis sensitivity test results of second generation accelerometer system. The sensitivity values are negligibly small.

	z-axis	**y-axis**
+1 g acceleration input	-55 mV	-50 mV
-1 g acceleration input	-60 mV	-53 mV
Cross-axis sensitivity	2.5 mV/g	1.5 mV/g

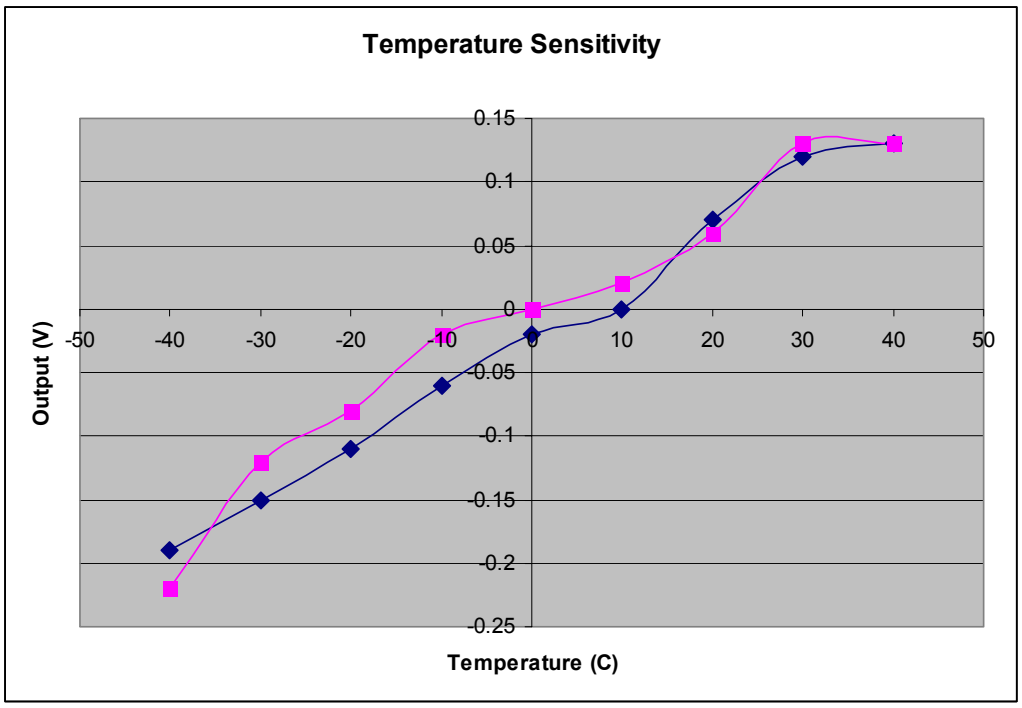

Figure 5.37: The output variation due to temperature change for the second generation accelerometer system. The output does not have exactly the same value at the same temperature value for increasing and deceasing temperature case. This error can be minimized with better packaging and with eliminating potentiometers in the system.

Table 5-7: The properties of second generation hybrid accelerometer system.

Voltage supply	± 12 V
Total dimensions	12 cm x 12 cm
Sensitivity (for (-3g, 6g) acceleration range)	1.02 V/g
Nonlinearity (for (-3g, 6g) acceleration range)	0.23 %
Mechanical noise floor	12.7 µg/√Hz
Total average noise floor	228 µg/√Hz
Total peak noise floor	375 µg/√Hz
Run-to-run bias drift	< 16.6 mg
Long-term bias drift	< 19 mg
Expected operation range	± 10 g

5.4 Summary and Discussion of the Fabrication and Test Results

The designed accelerometers and gyroscopes are fabricated using three different fabrication processes. For SOIMUMPs and nickel electroplating processes, working accelerometer and gyroscope samples are achieved but for DRIE process, due to the continuing optimization of the process, a working accelerometer or gyroscope sample cannot be realized. After the fabrication, all the necessary basic tests are done for each accelerometer and gyroscope sample, and for high performance accelerometer samples, two hybrid accelerometer-readout circuit systems are constructed and tested. This section gives the fabrication and tests results and suggests future tests.

- For SOIMUMPs process, the samples are released and then diced. Due to the shocks during the dicing operation, the gyroscope samples are severely damaged. However, the accelerometers have thicker critical dimensions than the gyroscopes; hence we do not encounter any damage in the accelerometers.

- For nickel electroplating process, the samples turned out to be just as we have expected. The formation of the mold photoresist is the critical fabrication step in this process, and with the knowledge gained from previous studies, we have almost perfectly characterized the shrinking of the photoresist in the exposure step. Hence, the fabricated sensors have almost the same resonance frequency values as we have calculated in the design period. However, the photoresist is also deformed in the hardbake step. This deformation cause capacitance mismatches, hence nonlinearity in the sensor and also may cause bias drift problems.

- For the DRIE process, we have not achieved any working sensor due to continuing optimization of the process. The wide openings are etched away very early then the small openings and this cause notching effect in the wide openings or unfinished etch regions in the small openings.

- Stiction, short circuit, sense capacitance, and resonance frequency test is performed for every working accelerometer and gyroscope sample. The resonance frequency tests results show that the fabricated sensors have very similar resonance frequencies as the designed values. This fact proves that the characterization of the process is well done in the design period.

- First generation hybrid accelerometer system is constructed using MS3110 commercial readout circuitry and a high performance SOIMUMPs accelerometer. This hybrid system consists of the sensor and the readout part only, however the bias and the amplifier circuits can be connected externally. This hybrid system is tested in the index table for sensitivity and nonlinearity, and also noise test is performed using a spectrum analyzer. The system shows 22.2 mV/g sensitivity with less than 0.1 % nonlinearity. The average noise floor and the peak noise floor of the system are measured as 799 μg/√Hz and 1.8 mg/√Hz, respectively.

- Second generation hybrid accelerometer system is constructed using high performance nickel electroplated accelerometer sample. This hybrid system consists of sensor part, MS3110 readout circuit, bias circuitry, and amplifier stages. The system is tested in the index table for nonlinearity and sensitivity values. Moreover, the system is put into a rate table to perform nonlinearity and sensitivity values for high acceleration values. Noise test is performed using a spectrum analyzer, and bias drift tests are using a computer connected multimeter. The tests show that the accelerometer has 1.02 V/g sensitivity with less than 0.3 % nonlinearity. The senor also has 228 μg/√Hz average noise floor and 375 μg/√Hz peak noise floor. Run-to-run bias drift and long-term bias drift of the sensor are found as 16.6 mg and 19 mg, respectively.

CHAPTER 6

CONCLUSION AND SUGGESTIONS FOR FUTURE RESEARCH

MEMS IMUs consisting MEMS accelerometers and gyroscopes started to appear in the market as effective and low prize solutions to inertial sensor applications. Capacitive MEMS accelerometers and gyroscopes started to dominate MEMS inertial sensor market with their high linearity, high sensitivity, low temperature dependency, low noise, and low cost. This study aims to achieve low cost, high performance accelerometer and gyroscope prototypes for some military and commercial use IMUs, using three different fabrication techniques.

The research done during this study can be summarized as:

1. Several accelerometer topologies are investigated and the best topology accelerometer is selected as the sensor topology. Moreover a new symmetric and decoupled (SYMDEC) gyroscope topology is proposed. The simulations of these topologies are done using MATLAB and COVENTORWARE.

2. 8 accelerometer prototypes and 4 gyroscope prototypes are designed for three different fabrication processes. The designs are verified with MATLAB and COVENTORWARE simulations. The mask designs for the fabrication processes are done.

3. The nickel electroplating process fabrication and majority of DRIE process fabrication steps are realized. SOIMUMPs process is realized CRONOS Inc., which is a commercial firm. Stiction, short circuit, sense capacitance, and resonance frequency tests are performed for each accelerometer and gyroscope sample, and high performance working accelerometer samples are selected.

4. Using two different accelerometer prototypes, two different hybrid systems are constructed using the accelerometer sample and MS3110 commercial capacitive readout circuit. Sensitivity, nonlinearity, and noise test is performed for both two prototypes. The second generation accelerometer is also tested for bias drift values, and nonlinearity and sensitivity under high acceleration inputs. This hybrid system satisfies the design goals with its compact structure having bias and amplifiers included. Table 6-1 gives the comparison of the design goals and the achieved accelerometer performance values. Sensitivity and nonlinearity goal is provided by ASELSAN. The bias drift goal is appropriate for some control applications in some commercial applications. Noise floor goal enables the accelerometer to be used for some control applications in some military and consumer applications.

5. A symmetric and decoupled gyroscope topology is realized. The resonance frequency test of this gyroscope is done with connecting a unity gain buffer.

Table 6-1: Comparison of design goals and achieved accelerometer performance values.

Parameter	Performance Goal	Achieved
Supply Voltage	± 12 V	± 12 V
Sensitivity	1 V/g	1.02 V/g
Noise Floor	500 μg/√Hz	375 μg/√Hz *
Nonlinearity	1 %	0.23 %
Bias-drift	20 mg	16.6 mg, 19 mg * *

* The total peak noise floor.
*We have found two kinds of bias drift as run-to-run and long-term bias drift. Each bias drift component is lower than 20 mg.

In addition to these achieved work, also some other future work can be suggested for the development of micromachined accelerometers and gyroscopes.

1. For the nickel electroplating process development, a new mask set should be prepared. This mask set should separate the bulky mold photoresist regions from the critical dimensions of the sensors. This separation will prevent the mold photoresist deformation in the hardbake step to affect the critical structural regions of the sensors. Hence, a lower drift, with lower capacitance mismatch sensors can be realized.

2. For the DRIE process development, a new mask set should be prepared. In this mask set, the openings for DRIE etch regions should have very similar widths. Hence, the etching will finish in every part of the sensor at the same time.

3. For the accelerometer prototype construction, SMD components can be used to occupy smaller area. Also a vacuum or inert gas packaging can be considered. If the SMD components can also be put into the same package, very small but well protected accelerometer system prototypes can be realized.

4. A low noise open-loop or closed-loop capacitive readout circuits for accelerometers can be designed and fabricated. As it can be seen from the test results of the hybrid accelerometer system, the system performance is mainly limited by the electronic noise. With a better electronic circuitry than MS3110, higher performance accelerometer hybrid systems can be realized.

In conclusion, the most important contribution of this work is construction of an accelerometer system that is composed of a MEMS accelerometer, a readout circuit, bias circuitries for this readout circuit, and external amplifier electronics. This system is the highest performance accelerometer system developed in Turkey. In addition, asymmetric and decoupled gyroscope topology is proposed and its operation is verified. The fabrication processes that are currently used in METU facilities are also improved with the gained knowledge and experience. It is hoped that this work will be an important step in developing tactical and inertial grade IMUs in METU.

REFERENCES

[1] M. D. Pottenger, "Design of Micromachined Inertial Sensors," *PhD. Dissertation*, Univ. of California, 2001.

[2] J. E. D. Williams, "From Sails to Satellites: The Origin and Development of Navigational Science," New York, Oxford University Press, 1994.

[3] S. E. Alper, "Silicon Surface Micromachined Gyroscopes Using MEMS Technology," *M.S. Thesis*, Middle East Technical Univ., 2000.

[4] K. Kumar, N. Barbour, and J. M. Elwell, "Emerging Low(er) Cost Inertial Sensors," *Proc. AIAA GN&C Conf.*, pp. 11-24, August 1992.

[5] M. Kraft, "Micromachined Inertial Sensors: The State of the Art and a Look into Future," *IMC Measurement and Control*, Vol. 33 No. 6, pp. 164-168, 2000.

[6] N. Yazdi, F. Ayazi, and K. Najafi, "Micromachined Inertial Sensors," *Proc. of the IEEE*, Vol. 86, No 8, pp. 1640-1659, August 1998.

[7] H. Kulah, "Closed-Loop Electromechanical Sigma-Delta Microgravity Accelerometers," *PhD. Dissertation*, Univ. of Michigan, 2003.

[8] J. Dosher and C. Kitchin, "Monitoring Machine Vibration with Micromachined Accelerometers," *Sensors 14(5)*, pp. 33-34, May 1997.

[9] P. F. Man, and C. H. Mastrangelo, "Surface micromachined shock sensor for impact detection," *Tech. Digest of IEEE Solid-State Sensors and Actuator Workshop (Hilton Head'94)*, pp.156-159, 1994.

[10] R. S. Seeley, "Micromachines Rev Up for Fast Growth," *Electronic Business Today*, pp- 33-38, April 1996.

[11] R. F. Yazıcıoğlu, "Surface Micromachined Capacitive Accelerometers Using MEMS Technology," *M.S. Thesis*, Middle East Technical Univ. ,2003.

[12] N. Barbour, G. Schmidt, "Inertial Sensor Technology Trends," *Workshop on Autonomous Underwater Vehicles*, pp.55-62, 1998.

[13] R. L. Craik and C. A. Oatis (Eds.), "Gait Analysis: Theory and Applications," Mosby, 1995.

[14] K. Miller, D. Hendelman, C. Baggett, E. Debold, and P. Freedson, "Validation of Accelerometry to Assess Moderate Intensity Physical Activity in the Field," *Medicine & Science in Sports & Exercise, 31(5)*, pp.43, May 1999.

[15] W. Kuehnel and S. Sherman, "A surface micromachined silicon accelerometer with on-chip detection circuitry," *Sensors and Actuators* Vol. A-45, pp. 7-16, 1994.

[16] S. J. Sherman, W. K. Tsang, T. A. Core, R. S. Payne, D. E. Quinn, K. H. L. Chau, J. A. Farash, and S. K. Baum, "A Low Cost Monolithic Accelerometer: Product/Technology Update," *Techncal Digest International Electron Devices Meeting*, pp.501-504, 1992.

[17] K. Jost, "Yaw Sensing," *Automotive Engineering*, pp. 61-63, September 1995.

[18] G. He and K. Najafi, "A Single-Crystal Silicon Vibrating Ring Gyroscope," *Proc. IEEE Micro Electro Mechanical Systems Workshop (MEMS'02)*, pp. 718-721, January 2002.

[19] W. Qu, C. Wenzel, and G Gerlach, "Fabrication of a 3D Differential-Capacitive Accelerometer by UV-LIGA," *Sensors and Actuators*, Vol. 77, pp. 14-20, 1999.

[20] J. W. Wiegold, K. Najafi, ans S. W. Pang, "Design and Fabrication of Submicrometer, Single Crystal Si Accelerometer," *Journal of Microelectromechanical Systems*, Vol.10, pp. 558-524, Dec.2001.

[21] K. H. –L. Chau, S. R. Lewis, Y. Zhao, R.T. Howe, S. F. Bart, and R. G. Marcheselli, "An Integrated Force-Balanced Capacitive Accelerometer for low-g Applications," *Sensors and Actuators*, Vol. 54, pp. 472-476, 1996.

[22] B. Guldimann, P. Thiebauld, N. F. de Rooji, and R. A. Turpin, "Micromachined, Fiber-Optic Based Accelerometer with Shutter Modulation," *Proc. IEEE Micro Electro Mechanical System Workshop (MEMS'00)*, 2000.

[23] A. Partidge, J. K. Reynolds, B. W. Chui, E. M. Chow, A. M. Fitzgerald, L. Zhang, and N.I. Maluf, "A High-Performance Planar Piozoresistive Accelerometer," *J. Microelectromechanical Sys.*, Vol. 9, No. 1, pp. 58-66, March 2000.

[24] H. Takao, Y. Matsumoto, and M. Ishida, "Stress-sensitive Differential Amplifiers Using Piozoresistive Effects of MOSFETs and Their Application to Three-Axis Accelerometers," *Sensors and Actuators*, Vol. 65, pp. 61-68, 1998.

[25] J. A. Plaza, M. A. Benitz, and Lora-Tamayo, "New FET Accelerometer Based on Surface Micromachining," *Sensors and Actuators*, Vol. 61, pp. 342-345, 1997.

[26] S. D. Senturia, "Microsystem Design," Kluwer Academic Publishers, 2001.

[27] F. Paelotti, "A Silicon Micromachined Vibrating Gyroscope with Piezoresistive Detection and Electromagnetic Excitation," *MEMS'96*, pp.162-167, 1996.

[28] R. Voss, "Silicon Angular Rate Sensor for Automotive Applications with Piezoelectric Drive and Piezoresistive Read-out," *Transducers'97*, Vol.2 pp.879-882, 1997.

[29] Y. Nemirovsky, A. Nemirovsky, P. Muralt, and N. Setter, "Design of Novel Thin-Film Piezoelectric Accelerometer," *Sensors and Actuators*, Vol. 56, pp. 239-249, 1996.

[30] D. L. DeVoe, and A. P. Pisano, "Surface Micromachined Piezoelectric Accelerometers (PiXLs)," *J. Microelectromechanical Sys*., Vol. 10, No. 2, pp. 180-186, June 2001.

[31] http://www.murata.com/ninfo/nr0283e.html

[32] V. Milanovi, E. Bowen, N. Tea, J. Suehle, B. Payne, M. Zaghloul, and M. Gaitan, "Convection-Based Accelerometer and Tilt Sensor Implemented in Standard CMOS," *Proc. Int. Mech. Eng. Conf. and Exp., MEMS Symposium*, Anaheim, Nov. 1998.

[33] A. A. Seshia, M. Palaniapan, T. A. Roessing, R. T. Howe, R. W. Gooch, T. R. Schimert, and S. Montague, "A Vacuum Packaged Surface Micromachined Resonant Accelerometer," *J. Microelectromechanical Sys*., Vol. 11, No. 6, pp. 784-793, Dec 2002.

[34] C.–H. Lui and T. H. Kenny, "A High-Precision, Wide-Bandwidth Micromachined Tunneling Accelerometer," *J. Microelectromechanical Sys*., Vol. 10, No. 3, pp. 425-433, Sept. 2001.

[35] F. Gretillat, M.-A. Gretillat, and N. F. de Rooij, "Improved Design of a silicon Micromachined Gyroscope with Piezoresistive Detection and Electromagnetic Actuation," *J. Microelectromechanical Sys*., Vol. 8, No. 3, pp. 243-250, September 1999.

[36] A. J. Harris, J. S. Burdess, D. Wood, R. Langford, G. Williams, M. C. L. Lard, and M. E. McNie, "Issues Associated with the Design, Fabrication and Testing of a Crystalline Silicon Ring Gyroscope with Electromagnetic Actuation and Sensing," *J. Micromech. Microeng*., pp. 284-292, August 1998.

[37] F. P. Beer and E. R. Johnston, "Mechanics of Materials," McGraw-Hill, 1985.

[38] R. J. Roark and W. C. Young, "Formulas for Stress and Strain," McGraw-Hill, 1983.

[39] M. W. Putty, "A Micromachined Vibrating Ring Gyroscope," *PhD. Dissertation*, Univ. of Michigan, 1995.

[40] A. Burstein, "Highly Sensitive Single and Dual-Axis High Aspect Ratio Accelerometers with a CMOS Precision Interface Circuit," *PhD Dissertation*, Univ. of California, 1999.

[41] W. T. Thomson and M. D. Dahleh, "Theory of Vibration with Applications," Prentice Hall, 1998.

[42] T. Veijola, H. Kuisma, and J. Lahdenpera, "The Influence of Gas-Surface Interaction on Gas-Film Damping in a Silicon Accelerometer," *Sensors and Actuators*, Vol. 66, pp. 83-92, 1998.

[43] T. Veijola, H. Kuisma, J. Lahdenpera, and T. Rayhanen, "Equivalent-Circuit Model of the Squeezed Gas Film in a Silicon Accelerometer," *Sensors and Actuators*, Vol. A-48, pp. 239-248, 1995.

[44] M. A. Lemkin, "Micro Accelerometer Design with Digital Feedback Control," *PhD. Dissertation*, Univ. of California, Berkeley, 1997.

[45] Y. J. Yang and C. J. Yu, "Macromodel Extraction of Gas Damping Effects for Perforated Surfaces with Arbitrary Shaped Geometries," *Modeling and Simulation of Microsystems*, pp. 178-181, 2002.

[46] P. C. Yen and Y. J. Yang, "Time-Domain Reduced-Order Models for Lateral Viscous Damping Effects for 3-D Geometries," *Modeling and Simulation of Microsystems*, pp. 190-193, 2002.

[47] A. Duwel, M. Weinstein, J. Gorman, J. Borenstein, and P. Ward, "Quality Factors of MEMS Gyros and the Role of Thermoelastic Damping," *Proc. IEEE Micro Electro Mechanical Systems Workshop (MEMS'02)*, pp. 214-219, January 2002.

[48] J. Chae, H. Kulah, and K. Najafi, "An All-Silicon In-Plane High-Sensitivity Low-Noise Micro-G Micromachined Accelerometer," *Proc. IEEE Micro Electro Mechanical Systems Workshop (MEMS'03)*, pp. 466-469, January 2003.

[49] W. Geiger, W. U. Butt, A. Gaiβer, J. Frech, M. Braxmaier, T. Link, A. Kohne, P. Nommensen, H. Sandmaier, and W. Lang, "Decoupled Microgyros and The Design Principle DAVED," *Tech. Dig. IEEE Micro Electro Mechanical Systems Conf. (MEMS 2001)*, pp. 170-173, January 2001.

[50] W. A. Clark and R. T. Howe, "Surface Micromachined Z-Axis Vibratory Rate Gyroscope," *Tech. Dig. Solid-State Sensor and Actuator Workshop*, , pp. 283-287, June 1996.

[51] X. Jiang, J. I. Seeger, M. Kraft, and B. E. Boser, "A Monolithic Surface Micromachined Z-Axis Gyroscope with Digital Output," *Symp. on VLSI Circuits Dig. of Tech. Papers*, , pp. 16-19, June 2000.

[52] B. E. Boser, "Capacitive Sensor Interfaces," Univ. of Berkeley, pp. 1-41, 1996.

[53] J. R. Vig and Y. Kim, "Noise in Microelectromechanical System Resonators," *IEEE Trans. On Ultrasonics, Ferroelectrics, and Frequency Control*, Vol. 46, No.6, pp. 1558-1565, Nov. 1999.

[54] IEEE Standard Specification Format Guide and Test Procedure for Linear, Single-Axis, Pendulous, Analog Torque Balance Accelerometers, 1972.

[55] G. K. Fedder, "Simulation of Microelectromechanical Systems," *Ph.D. Dissertation*, Univ. of California, Berkeley, 1994.

[56] F. Ayazi, H. H. Chen, F. Kocer, G. He, and K. Najafi, "A High Aspect Ratio Polysilicon Vibrating Ring Gyroscope," *Digest, Solid-State Sensors and Actuators Workshop*, pp 289-292, June 2000.

[57] S. An, Y. S. Oh, B. L. Lee, K. Y. Park, S. J. Kang, S. O. Choi, Y. I. Go, and C. M. Song, "Dual-Axis Microgyroscope with Closed-Loop Detection," *Proc. IEEE Micro Electro Mechanical Systems Workshop (MEMS'98)*, pp. 328-333, 1998.

[58] www.memscap.com/memsrus/docs/SOIMUMPs.DR.4.0.pdf

[59] J. Chae, H. Kulah, H. Najafi, "A Hybrid Silicon-On-Glass (SOG) Lateral Micro-Accelerometer With CMOS Readout Circuitry," *Proc. IEEE Micro Electro Mechanical Systems Workshop (MEMS'02)*, pp. 623-626, Jan 2002.

[60] P. J. French and P. M. Sarro, "Surface versus Bulk Micromachining: The Contest for Suitable Applications," *J. Micromech. Microeng.*, pp. 45-53, August 1998.

[61] M. J. Madou, "Fundementals of Microfabrication: The science of Miniaturization," CRC, 2002.

[62] G. T. Kovacs, N. I. Maluf, and K. E. Petersen, “Bulk Micromachining of Silicon,” *Proc. IEEE*, Vol. 86, No. 8, pp. 1536-1551, August 1998.

[63] J.-L. Yeh, “Integrated Polysilicon Surface and DRIE Bulk Silicon Micromachined Devices,” *Ph.D. dissertation*, Cornell University, 2000.

[64] B. Loechel, "Thick-layer Resists for Surface Micromachining," *J. Micromech. Microeng.* Vol. 10, No. 2, pp. 108-115, June 2000.

[65] H. Kuisman, T. Ryhanen, J. Lahpendera, E. Punkka, S. Routsalainen, T. Sillanpaa, and H. Sepa, “A Bulk Micromachined Silicon Angular Rate Sensor,” *Tech. Dig. 9th Int. Conf. Solid-State Sensors and Actuators (Transducers’97)*, pp. 875-878, June 1997.

[66] T. K. Tang, R. C. Gutierrez, J. Z. Wilcox, C. Stell, V. Vorperian, R. Calvet, W. J. Li, I. Charkaborty, R. Bartman, and W. J. Kaiser, “Silicon Bulk Micromachined Vibratory Gyroscope,” *Tech. Dig. Solid-State Sensors and Actuators Workshop*, pp. 288-293, June 1996.

[67] G. I. Andersson, N. Hedenstierna, P. Svensson and Hakan Pettersson, “A Novel Silicon Bulk Gyroscope,” *Tech. Dig. 10th Int. Conf. Solid-State Sensors and Actuators (Transducers’99)*, pp. 902-905, June 1999.

[68] R.P. van Kampen and R. F. Wolffenbuttel, “Modeling the Mechanical Behaviour of Bulk-Micromachined Silicon Accelerometers,” *Sensors and Actuators*, Vol. 64, pp. 137-150, 1998.

[69] Y. Oh, B. Lee, S. Baek, H. Kim, J. Kim, S. Kang, and C. Song, “A Surface-Micromachined Tunable Vibratory Gyroscope,” *Proc. IEEE Micro Electro Mechanical Sytems Workshop (MEMS’97)*, pp. 272-277, 1997.

[70] W. A. Clark and R. T. Howe, “Surface Micromachined Z-axis Vibratory Rate Gyroscope,” *Tech. Dig. Solid-State Sensor and Actuator Workshop*, pp. 283-287, June 1996.

[71] K. Funk, H. Emmerich, A. Schilp, M. Offenberg, R. Neul, and F. Larmer, “A Surface Micromachined Silicon Gyroscope Using a Thick Polysilicon Layer,” *Proc. IEEE Micro Electro Mechanical Systems Workshop (MEMS’99)*, pp. 57-60, January 1999.

[72] C. Hierold, A. Hildebrandt, U. Naher, T. Scheiter, B. Mensching, M. Steger, and R. Tielert, “A Pure CMOS Surface-Micromachined Integrated Acelerometer,” *Sensors and Actuators*, Vol. 57, pp. 111-116, 1996.

[73] B. E. Boser and R. T. Howe, "Surface Micromachined Accelerometers," *IEEE J. Solid-State Cct*, Vol. 31, No.3, pp. 366-375, March 1996.

[74] N. Yazdi and K. Najafi, "An All-Silicon Single-Wafer Micro-g Accelerometer with a Combined Surface and Bulk Micromachining Process," *J. Microelectromechanical Sys*., Vol. 9, No. 4, pp. 544-550, December 2000.

[75] S. Lee, S. Park, J. Kim, S. Lee, and Dong-il (Dan) Cho, "Surface/Bulk Micromachined Single-Crystalline-Silicon Micro-Gyroscope," *J. Microelectromechanical Sys.*, Vol. 9, No. 4, pp. 557-567, December 2000.

[76] C. Lu, M. Lemkin, and B. E. Boser, "A Monolithic Surface Micromachined Accelerometer with Digital Output," *IEEE Journal of Solid-State Circuits*, Vol. 30, No. 12, pp. 1367-1373, Dec. 1995.

[77] J. Gobet, F. Cardot, J. Bergqvist, and F. Rudolf, "Electrodeposition of 3D Microstructures on Silicon," *J. Micrimech. Microeng*. Vol. 3, No. 3, pp. 123-130, September 1993.

[78] W. Ruythooren, K. Attenborough, S. Beerteen, P. Merken, J. Fransaer, E. Beyne, C. Van Hoof, J. De Boeck, and J. P. Celic, "Electrodeposition for the Synthesis of Microsystems," *J. Micromech. Microeng*. Vol. 10, No. 2, pp. 101-107, June 2000.

[79] Shipley Microposit SJR 5000 Photoreisit Datasheet.

[80] X. Li, S. Kiyawat, H. J. Santos, and C. J. Kim, "High-Aspect-Ratio Electroplated Structures with 2 μm Beamwidth," *Proc. MEMS (MEMS-Vol.1), ASME Int. Mechanical Eng. Congress and Exposition*, pp. 25-30, Nov. 1999.

[81] F. Laermer, A. Schilp, K. Funk, and M. Offenberg, "Bosch Deep Silicon Etching: Improving Uniformity and Etch Rate for Advanced MEMS Applications," *Proc. IEEE Micro Electro Mechanical Systems Workshop (MEMS'99)*, pp. 211-216, January 1999.

[82] M. Chabloz, J. Jiao, Y. Yoshida, T. Matsuura, and K. Tsutsumi, "A Method to Evade Microloading Effect in Deep Reactive Ion Etching for Anodically Bonded Glass-Silicon Structures," *Proc. IEEE Micro Electro Mechanical Systems Workshop (MEMS 2000)*, pp. 283-287, January 2000.

[83] M. A. Schimidt, "Wafer-to-wafer bonding for microstructure formation," *Proc. IEEE*, Vol. 86, pp. 1574-1585, Aug 1998.

[84] G. Willis, "Direct-current polarization during field-assisted glass-metal sealing," *J. Amer. Ceramic. Soc*. Vol. 53, pp. 563-567, 1970.

[85] T. M. H. Lee, I.-M. Hsing, and C. Y. N. Liaw, "An Improved Anodic Bonding Process Using Pulsed Voltage Technique," *J. Microelectromechanical Sys*., Vol. 9, No. 4, pp. 469-473, December 2000.